[illegible]
[illegible]
[illegible]

NAVAL POSTGRADUATE SCHOOL

Monterey, California

THESIS

ELECTROMAGNETIC NEAR-FIELD COMPUTATIONS FOR A BROADCAST MONOPOLE USING NUMERICAL ELECTROMAGNETICS CODE (NEC)

by

David Duerr Thomson

September 1983

Thesis Advisor: S. Jauregui

Approved for public release, distribution unlimited

T215705

REPORT DOCUMENTATION PAGE		READ INSTRUCTIONS BEFORE COMPLETING FORM
1. REPORT NUMBER	2. GOVT ACCESSION NO.	3. RECIPIENT'S CATALOG NUMBER
4. TITLE (and Subtitle) Electromagnetic Near-Field Computations for a Broadcast Monopole using Numerical Electromagnetics Code (NEC)		5. TYPE OF REPORT & PERIOD COVERED Master's Thesis; September 1983
		6. PERFORMING ORG. REPORT NUMBER
7. AUTHOR(s) David Duerr Thomson		8. CONTRACT OR GRANT NUMBER(s)
9. PERFORMING ORGANIZATION NAME AND ADDRESS Naval Postgraduate School Monterey, California 93943		10. PROGRAM ELEMENT, PROJECT, TASK AREA & WORK UNIT NUMBERS
11. CONTROLLING OFFICE NAME AND ADDRESS Naval Postgraduate School Monterey, California 93943		12. REPORT DATE September 1983
		13. NUMBER OF PAGES 149
14. MONITORING AGENCY NAME & ADDRESS(if different from Controlling Office)		15. SECURITY CLASS. (of this report) UNCLASSIFIED
		15a. DECLASSIFICATION/DOWNGRADING SCHEDULE

16. DISTRIBUTION STATEMENT (of this Report)

Approved for public release, distribution unlimited

17. DISTRIBUTION STATEMENT (of the abstract entered in Block 20, if different from Report)

18. SUPPLEMENTARY NOTES

19. KEY WORDS (Continue on reverse side if necessary and identify by block number)

Electromagnetics; Near-Field Computations; Numerical Electromagnetics Code (NEC)

20. ABSTRACT (Continue on reverse side if necessary and identify by block number)

An often ignored aspect of electromagnetic radiation from antennas is the characterization of their near-fields. A computer program, Numerical Electromagnetics Code (NEC), is validated for accurate near-field computations and applied to a model of a broadcast monopole. E- and H-fields are plotted as a function of position along the antenna for various distances from the surface. The fields are also plotted as a function of radial distance outward for various heights.

DD FORM 1 JAN 73 1473 EDITION OF 1 NOV 65 IS OBSOLETE
S/N 0102-LF-014-6601

Approved for public release, distribution unlimited

Electromagnetic Near-Field Computations for a Broadcast Monopole using Numerical Electromagnetics Code (NEC)

by

David Duerr Thomson
Lieutenant Commander, United States Navy
B.S.E.E., University of Washington, 1971

Submitted in partial fulfillment of the
requirements for the degree of

MASTER OF SCIENCE IN ELECTRICAL ENGINEERING

from the

NAVAL POSTGRADUATE SCHOOL
September 1983

ABSTRACT

An often ignored aspect of electromagnetic radiation from antennas is the characterization of their near-fields. A computer program, Numerical Electromagnetics Code (NEC), is validated for accurate near-field computations and applied to a model of a broadcast monopole. E- and H-fields are plotted as a function of position along the antenna for various distances from the surface. The fields are also plotted as a function of radial distance outward for various heights.

TABLE OF CONTENTS

I. INTRODUCTION---------------------------------- 6

A. PROBLEM ENVIRONMENT---------------------------- 6

B. THESIS STATEMENT, SCOPE AND LIMITATIONS------ 8

II. DESCRIPTION OF SELECTED ANALYSES---------------- 12

A. CLASSICAL ANALYSIS---------------------------- 12

B. CONTEMPORARY ANALYSIS------------------------- 22

1. The Integral Equation Method------------ 22

2. The Sweep-Off Method-------------------- 24

3. Mode Theory of Antennas----------------- 26

4. Discussion------------------------------ 26

C. NUMERICAL ANALYSIS---------------------------- 27

1. Hallen's Approach----------------------- 27

2. Parabolic Interpolative Fit Approach----- 28

3. Bessel Function Fit Approach------------ 30

4. Discussion------------------------------ 31

III. DESCRIPTION OF NEC------------------------------ 33

A. FEATURES OF THE CODE-------------------------- 33

B. ZONING CONSIDERATIONS------------------------- 34

1. Wires----------------------------------- 35

2. Surfaces-------------------------------- 36

3. Ground Plane---------------------------- 37

C. INTEGRAL EQUATIONS---------------------------- 38

1. Electric Field Integral Equation (EFIE)-- 38

2. Magnetic Field Integral Equation (MFIE)-- 40

3. Hybrid EFIE/MFIE------------------------ 42

D. METHOD OF MOMENTS AND THE MATCH POINT-------- 43

1. Mathematical Concept--------------------- 43

2. NEC's Application------------------------ 45

IV. MODEL DESCRIPTION AND COMPUTATIONAL RESULTS------ 53

A. MODEL DESCRIPTION---------------------------- 53

1. Assumed Current Distribution------------- 53

2. Modal Modeling--------------------------- 54

3. Sub-domain Modeling---------------------- 54

B. MODEL CONFIGURATIONS------------------------- 55

C. EXPECTATIONS/OBSERVATIONS/ANOMALIES---------- 56

1. E(Z) Plots------------------------------- 60

2. E(R) Plots------------------------------- 67

3. H(Z) Plots------------------------------- 72

4. H(R) Plots------------------------------- 75

V. A VALIDATION OF NEC NEAR-FIELD CALCULATIONS------ 77

A. COMPARISON OF NEC WITH CLASSICAL ANALYSIS RESULTS-- 77

B. COMPARISON OF NEC WITH EMPIRICAL ANALYSIS RESULTS-- 79

C. COMPARISON OF NEC WITH MAXWELL'S EQUATIONS--- 80

VI. CONCLUSIONS AND RECOMMENDATIONS----------------- 87

APPENDIX A-- 88

APPENDIX B --------------------------------------- 132

LIST OF REFERENCES-------------------------------- 148

INITIAL DISTRIBUTION LIST------------------------- 149

I. INTRODUCTION

A. PROBLEM ENVIRONMENT

Maxwell's equations describe, for all space, the Electric (E) and Magnetic (H) Fields that are the medium for transmitting information (virtually) instantaneously over extended distances. This practical application of electromagnetic (EM) radiation has generated considerable interest in its far-field* characteristics. The E and H vectors can be analytically determined when the current (I) on the radiator (from which the field vectors are generated) has been described. For the far-field region of monopoles and dipoles, acceptable results are obtained by assuming a sinusoidally varying current. However, when the field vectors are calculated for field points at distances less than $\lambda/2\pi$ (the near-field region), significant errors occur between calculated values and empirically measured values. This discrepancy is not the result of inaccuracies in Maxwell's Equations, but can be wholly attributed to an inaccurate description of the current.

---

*The far-field, for a monopole or dipole, is defined as distances from the radiator greater than $\lambda/2\pi$, where λ is the wavelength. For free space, $\lambda=c/f$ where f=the frequency at which the radiator is excited, and c=the speed of light in free space.

In the past, the inaccuracies of the near field calculations were not a problem--there was no practical application to which the energy could be applied. However, in recent years there has been an escalating interest in the close-in problem. This interest has been generated by an increasing proliferation of devices which use Radio Frequency (RF) energy in such a manner that the user is exposed to near-field radiation (e.g. microwave ovens, hand-held walky-talkies, wireless telephones, RF sealers, etc.).

The U.S. Navy was one of the first organizations to express an interest in these fields. The interest was the result of a concern for the hazards these fields might pose to fuels, ordnance, other EM operational and test equipment, and to personnel. The hazards posed by fuels, ordnance, and other EM equipment result in overt effects; the hazards posed to personnel are not so obvious.

With virtually unanimous consensus, the literature identifies the heating of body tissue as the primary hazard to personnel. However, some distinctly non-thermal effects have been observed. Some of these effects [Ref. 1] include:

a) minor changes in blood properties

b) a "buzz" heard by certain people when exposed to microwave radiation*

---

*The "buzz" is assumed to be a function of the pulse repetition rate (PRR) rather than the carrier frequency.

c) abnormalities of the chromosome structure

d) movement, orientation, and polarization of protein molecules

e) changes in the transport rate at the blood-brain barrier

f) comfort imbalances, such as epigastric distress, emotional upset, and nausea.

The significance of these effects is not yet understood.

The general public has not been exposed to near-field radiation hazards of sufficient intensity or duration to be cause for alarm; however, there are certain vocations in which the incumbents have an elevated probability of exposure to this type of field.*

B. THESIS STATEMENT, SCOPE AND LIMITATIONS

In order to provide more accurate data for people researching biological effects of near-field radiation, this study will validate a computer program which computes the near electric, magnetic, and composite (peak) fields of an arbitrary radiator. The program will also be used to compute these near fields for a model to be described below. The program, Numerical Electromagnetics Code (NEC), was developed at Lawrence Livermore Laboratory under the

---

*Sailors at sea or steeplejacks who effect antenna repairs, for instance.

sponsorship of the Naval Ocean Systems Center (NOSC) and the Air Force Weapons Laboratory. It can be easily learned and applied directly by a researcher who has some knowledge of electromagnetic theory.

The model to be used for the investigation will be a 75 meter high broadcast monopole radiating above a perfectly conducting ground plane. The ground plane is located in the X-Y plane; the monopole is co-axial with the Z-axis. The antenna will be excited at its base with a voltage sufficient to produce a radiated power of 1000 watts. The excitation is at a frequency of 1 Megahertz, which has a wavelength of 300 meters; hence, the monopole is a quarter-wavelength radiator operating at resonance. A diagram of the model is shown in Figure 1.

In simulating this model, NEC requires that the antenna be broken into virtual short straight segments. In consonance with this requirement, three different configurations will be used for computations; a model composed of 5, 15, and 25 segments of 15, 5, and 3 meters, respectively.

Using cylindrical coordinates, the radial and parallel electric fields, and the tangential magnetic field will be computed. Field values will be computed in .1 meter increments for points parallel to the z-axis at distances of 1*, 2, 5, 10, 100, and 1000 radii (1 radius = .3 meters).

---

*1 radius = surface of the monopole.

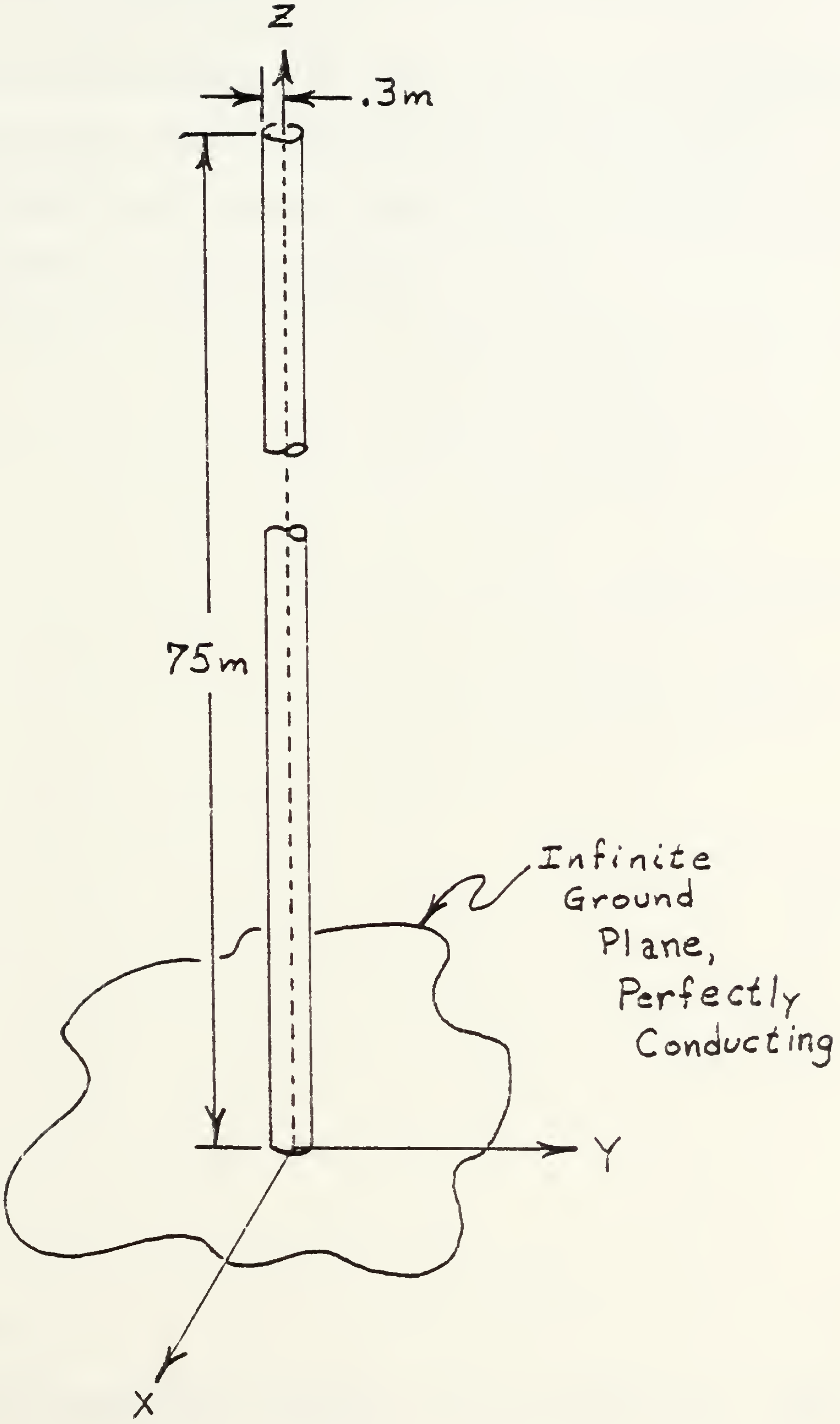

Figure 1

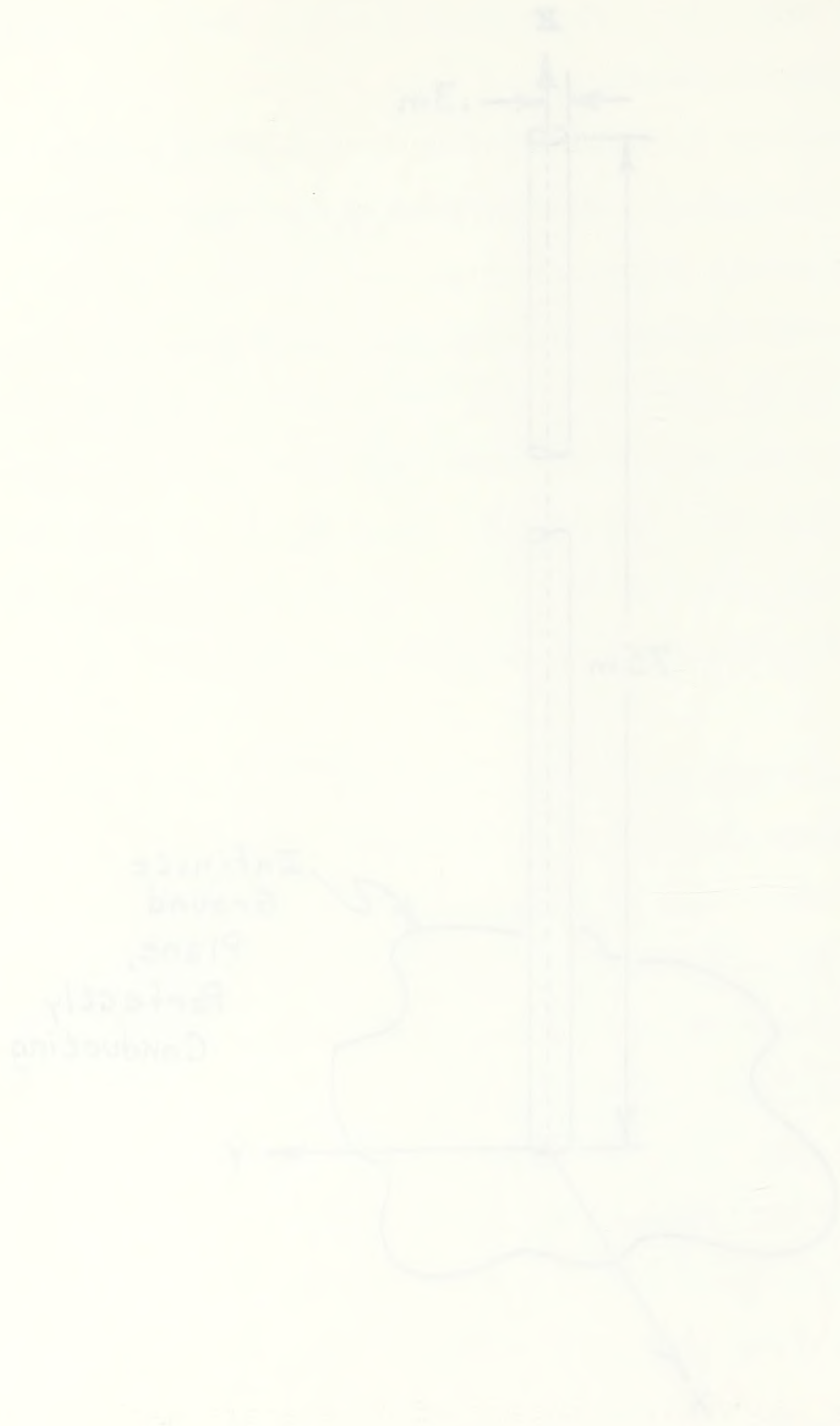

Figure 1

Field values will also be calculated along the radial axis (Y-axis) in increments of .5 meters for heights (h) of 2h, 1h, 1/2h, 1/4h, and 2/100ths h.*

The near-field examined in this study is the cylindrical volume bounded by a cylinder of one wavelength radius centered on the Z-axis, rising from the ground plane to a height twice that of the monopole.

---

* This is the approximate height of an average mans upper torso.

II. DESCRIPTION OF SELECTED ANALYSES

A. CLASSICAL ANALYSIS

The antenna utilized in this study is a member of the class identified as 'thin-wire' antennas. The criteria which adumbrate the thin-wire approximation are [Ref. 2]:

a) Transverse currents are negligible relative to axial currents

b) Circumferential variations of the axial current are negligible

c) The current can be represented by a filament current on the wire axis

d) Boundary conditions on the electric field need be enforced only in the axial direction.

By far, the largest subset of thin-wire antennas is a class known as short antennas. Short antennas are defined as having one dimension (h) much greater than the other dimensions, but h is also much less than a wavelength, typically $h < \lambda/8$. Because of the predominance of this sub-set, it is reasonable that it should be used as a model for classical analysis.

Based on Maxwells Equations and geometric considerations as shown in Figure 2, the following non-zero complex scalar field components can be derived:

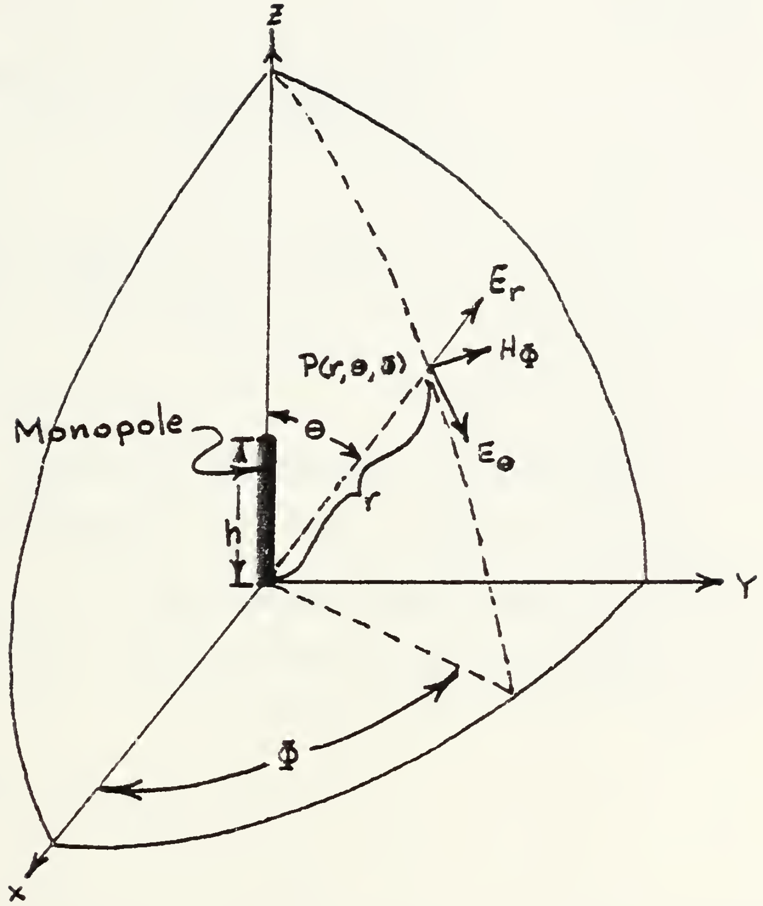

Figure 2

$$E_\theta = \frac{\eta I h}{4\pi} \sin\theta \left(\frac{j\beta}{r} + \frac{1}{r^2} - \frac{j}{\beta r^3}\right) e^{-j\beta r} \qquad (1)$$

$$E_r = \frac{\eta I h}{2\pi} \cos\theta \left(0 + \frac{1}{r^2} - \frac{j}{\beta r^3}\right) e^{-j\beta r} \qquad (2)$$

$$H_\phi = \frac{I h}{4\pi} \sin\theta \left(\frac{j\beta}{r} + \frac{1}{r^2} + 0\right) e^{-j\beta r} \qquad (3)$$

where: η = the intrinsic impedance of the medium, I = antenna current, λ = wavelength, $\beta = 2\pi/\lambda$ = phase constant, h = monopole height, r = distance of field observation point from monopole base. Since there is no variation in Φ:

$$E_\phi = H_\theta = H_r = 0 \qquad (4)$$

The interpretation of these equations under classical analysis require two additional assumptions:

a) The distance to the field observation point is large relative to the monopole height, and

b) An harmonically time varying current is uniform over the height of the monopole.

The first of these assumptions is made to focus attention to that volume of space where the lines of force have detached themselves from the antenna and are approaching the form of

a plane wave front. The second assumption is to form a first approximation of the current distribution on the wire which is solvable in closed form. Extensive analysis over many years has shown this to be a valid assumption when the antenna is excited at a single point.

In this study, we will be interested in fields where the observation points are not at distances considered large relative to the monopole height. When this is the case, the diagram of Figure 2 must be modified as shown in Figure 3*. From the geometry of this figure, the following non-zero complex scalar field components can be derived:

$$E_\theta = -\frac{j\eta I_o}{4\pi}\left(\frac{e^{-j\beta r_1}}{r_1} + \frac{e^{-j\beta r_2}}{r_2} - 2(\cos\beta h)\,\frac{e^{-j\beta r_0}}{r_0}\right) \qquad (5)$$

$$E_\rho = \frac{j\eta I_0}{4\pi}\left(\frac{z-h}{\rho}\,\frac{e^{-j\beta r_1}}{r_1} + \frac{z+h}{\rho}\,\frac{e^{-j\beta r_2}}{r_2} - \frac{2z\cos\beta h}{\rho}\,\frac{e^{-j\beta r_0}}{r_0}\right) \qquad (6)$$

$$H_\phi = \frac{jI_0}{4\pi\rho}\left(e^{-j\beta r_1} + e^{-j\beta r_2} - 2(\cos\beta h)e^{-j\beta r_0}\right) \qquad (7)$$

---

*Equations (1) through (3) are expressed in spherical coordinates while Equations (5) through (7) have been transformed to cylindrical coordinates.

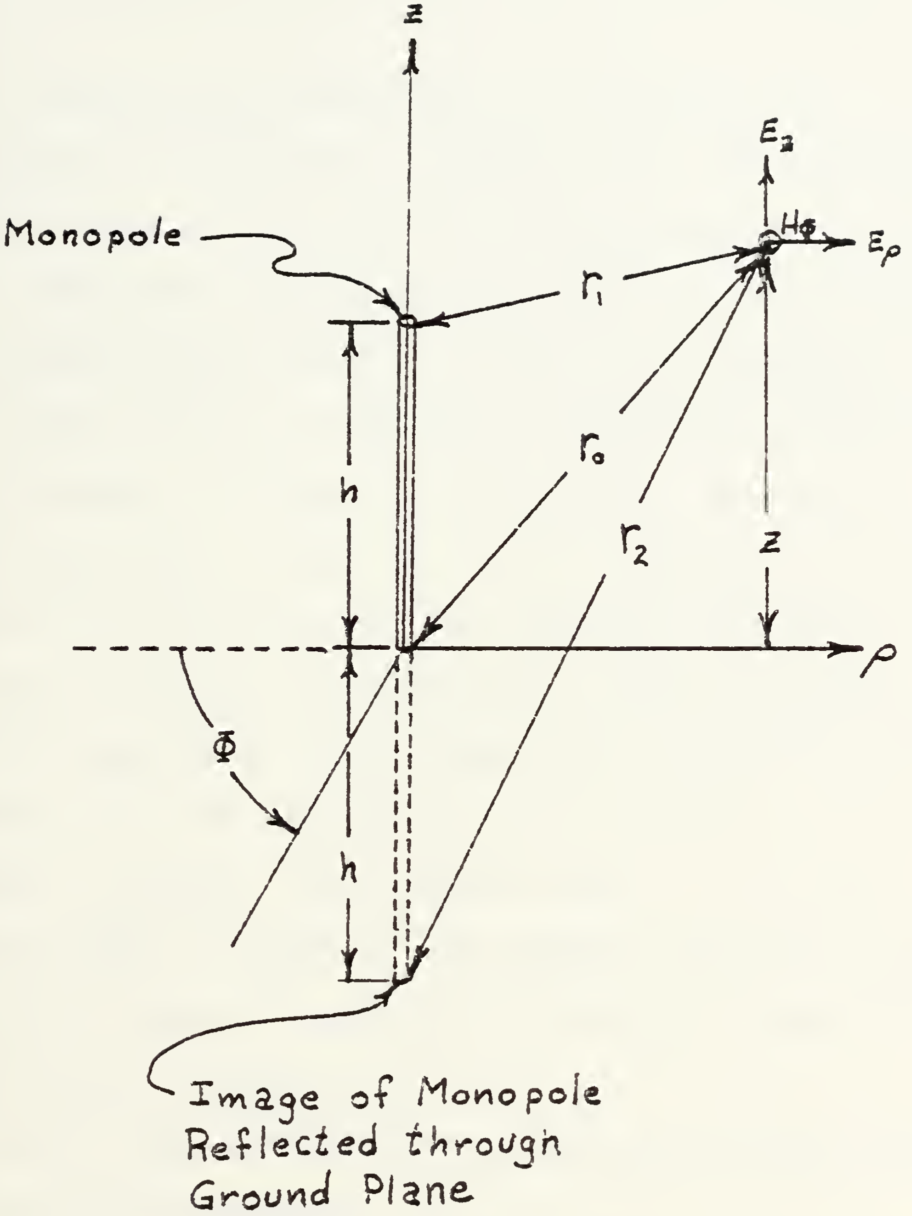
z
E_z
Monopole
H_φ
E_ρ
r_1
r_0
r_2
h
z
ρ
Φ
h
Image of Monopole Reflected through Ground Plane

Figure 3

A current of the form:

$$I(z) = I_0 \sin\beta h \text{ for } 0 \leq z \leq h \qquad (8)$$

has been inserted into Equations (5) through (7).

Equations (5) through (7) indicate that each field component is the phasor sum of contributions from three point sources. The first source is located at the top of the monopole, a second image source is located in a symmetric position when the first source is reflected through the ground plane. The third source is located at the base of the monopole; its relative amplitude is modified by the ($-2\cos\beta h$) factor.

Since we have a solution for computing the field points, it is now reasonable to determine the range over which it is valid. By inspection we note that for $r = \lambda/2\pi$ in Equations (1) through (3), the magnitude of each non-zero term in the parenthesis is equal. This implies that $r = \lambda/2\pi$ may be a transition point. Further investigation indicates that for:

a) $r > \lambda/2\pi$: the $1/r^3$ terms in E_θ and H_ϕ, and the $1/r^2$ term in E_r are dominant

b) $r < \lambda/2\pi$: the $1/r^3$ terms in E_θ and E_r, and the $1/r^2$ term in H_ϕ are dominant.

Since we know that power drops off as the inverse square of distance, and that the power flow at a field point can be defined in terms of its E-field as:

$$P = E^2/\eta \tag{9}$$

we can extrapolate from a) above ($E^2\theta/\eta \propto k/r^2$; where k = a constant) that the far-field begins at $r = \lambda/2\pi$ and continues out to infinity, while the near-field begins at the monopole and continues out to $r = \lambda/2\pi$.*

It is interesting to note the complementary relationship that is maintained by the power in this transition region. Instantaneous power flow at a point in space is given by the complex Poynting vector:

$$\overline{S}^* = 1/2(\overline{E} \times \overline{H}) \tag{10}$$

For the short monopole, the complex Poynting vector is oriented in the radial direction and given by:

$$\overline{S}^*_r = \frac{\eta}{2}\left(\frac{Ih}{4\pi}\right)(\sin\theta)e^{-j\beta r})^2\left(\frac{\beta^2}{r^2} - \frac{j}{\beta r^5}\right)\hat{r} \tag{11}$$

The real part of this equation gives the average rate of flow of Real power ($\propto 1/r^2$) while the Imaginary part is proportional to the difference between average magnetic energy density

---

*This argument is offered not as a proof, but as a reasonable rationale which can be empirically verified.

and average electric energy density ($\propto 1/r^5$). Interpretation of this equation indicates that for:

a) $r > \lambda/2\pi$: Reactive power flow decreases rapidly ($\propto \frac{1}{r^5}$), Real power flow decreases not so rapidly ($\propto \frac{1}{r^2}$)

b) $r = \lambda/2\pi$: Average Real power flow and average Reactive power flow are equal

c) $r < \lambda/2\pi$: Reactive power flow becomes much greater ($\propto r^5$) than Real power flow ($\propto r^2$).

The transverse component of the complex Poynting vector:

$$\overline{S}^*_t = \eta\left(\frac{Ih}{4\pi} e^{-j\beta r}\right)^2 \cos\theta \sin\theta \left(-j\left(\frac{\beta}{r^3} + \frac{1}{\beta r^5}\right)\right) \hat{\theta} \qquad (12)$$

is completely Imaginary, indicating no Real power flow, and it falls off rapidly with increasing distance due to $1/r^3$ and $1/r^5$ contributions.*

The deviant behavior of the fields encountered at distances $r < \lambda/2\pi$ is the result of moving from a region where the lines of force are closed on themselves and approaching a plane wave front, to a region where the lines of force still maintain a strongly spherical wave front and some of the lines are still attached to the antenna. Even in the simplest of

---

*Also noted is the fact that the Electric field changes from Elliptical polarization to Linear polarization in passing from $r > \lambda/2\pi$ to value of $r < \lambda/2\pi$ when $\theta \neq 0°, 90°$, or $180°$. For these angles the polarization of the electric field is linear on both sides of $r = \lambda/2\pi$.

cases, the current distribution in conductors is complex. This complexity is the result of non-uniform currents and charge densities, capacitance and inductance generated by these non-uniformities, and discontinuities from impressed forcing functions.

It is well established that as the field observation point moves within the $\lambda/2\pi$ distance from the antenna, that the measured values deviate from those predicted by Equations (5) through (7). It is also well established that Maxwells equations are valid for all space. Consequently, the conclusion is that the sinusoidal current distribution is not sufficiently accurate for determining field points within the near-field region. The problem then is to find a better description of the current distribution. This is the domain of contemporary analysis.

Before proceeding, it is necessary to reflect that the analysis performed thus far has been for a short antenna. The model for this study is a resonant monopole; when the antenna is lengthened to resonance some interesting characteristics appear. Primary among these is the fact that the reactive component of the impedance vanishes, which says the input reactance goes to zero. The current on the antenna and the voltage required to place it there are determined solely by the resistance, the real part of the impedance. When a sinusoidal current is assumed on the antenna, the tangential field component is given by:

$$E_z = -j \frac{\eta I_o}{4\pi} \left(\frac{e^{-j\beta r_1}}{r_1} + \frac{e^{-j\beta r_2}}{r_2}\right) \tag{13}$$

The $(-2\cos\beta h)$ term representing radiation from the base of the monopole has disappeared. The monopole appears as a point source radiating from its height, and an image source found at the reflection through the ground plane.

Also, the resonant condition occurs at a length less than that expected from the $\lambda/4$ relationship. This is the result of an "effective" lengthening of the antenna by capacitance and "fringing" at the end-cap of the wire. Capacitance is caused by a build-up of charge at the end of a wire of finite width. The change in direction of the geometry at the end of the wire also changes the direction of the lines of force emanating perpendicular from it; this is the fringing effect. These factors cause resonance to occur for an antenna length of $h = \lambda/4 - \delta$ where δ is a function of the capacitance caused by the two effects discussed above.

The short monopole development discussed above is very restrictive and cannot be applied directly to resonant monopoles. However, when the resonant peculiar characteristics mentioned are taken into consideration, the resulting development will follow the same procedure as used for the short monopole. For the resonant monopole development and results, see Ref. 4.

B. CONTEMPORARY ANALYSIS

Schelkunoff [Ref. 3: pp. 370-374] identifies three methods for obtaining a closer approximation to the actual current distribution on an antenna. They are:

a) The Integral Equation method

b) The Sweep-Off method

c) The Mode Theory of Antennas method.

Each are discussed below, in succession.

1. The Integral Equation Method

The assumption is made that the current is distributed on the surface of a hollow cylinder which is divided into filaments of angular density $(I(z')/2\pi)$ and angular width $(d\Phi')$. The Kernel Function is modified to allow for variations in Φ and is expressed as an integral around the circumference of the wire as:

$$\Gamma(z,z') = \frac{1}{2\pi} \int_0^{2\pi} \psi\,(z,z',\Phi,\Phi')\,d\Phi' \qquad (14)$$

where: $\psi = \frac{e^{-j\beta r}}{4\pi r}$ = wave function.

The field intensity for a straight current filament:

$$E_z = \frac{1}{j\omega\varepsilon} \int_{z_1}^{z_2} \left(\frac{\partial^2\psi}{\partial z^2} + \beta^2\psi\right) I(z')\,dz' \qquad (15)$$

is modified by inclusion of Equation (14), with the boundary condition: $(E_z + E_z^i = 0)$ enforced to give:

$$-E_z^i(z) = \frac{1}{j\omega\varepsilon} \int_{z_1}^{z_2} \left(\frac{\partial^2\Gamma}{\partial z^2} + \beta^2\Gamma\right) I(z')\, dz' \tag{16}$$

This Integral Equation (from which the name of the method derives) is the limit (as N→∞) of a series of equations of the form:

$$-E_z^i(z) = \sum_{n=1}^{N} \frac{1}{j\omega\varepsilon} \left[\frac{\partial^2\Gamma(z_n,z)}{\partial z^2} + \beta^2\ (z_n,z)\right] \Delta z_n\, I(z_n) \tag{17}$$

which is also of the form:

$$-E_z^i(z) = Z_{mn}\, I(z) \tag{18}$$

Equation (16) is a 'circuit equation' for an antenna and can be solved, in a manner analogous to the use of Kirchhoffs Equations for lumped networks, to an arbitrary degree of accuracy through the use of Equation (17).

It is instructive at this point to pause and consider how accurately our initial approximation of the current approached reality. Integrating Equation (16) by parts and setting $-E_z^i(z)=0$, as it is on the surface of the antenna, we obtain:

$$\left(I(z')\Gamma(z,z') + I(z')\frac{\partial\Gamma}{\partial z}\right) - \int_{z_1}^{z_2} \left(\frac{d^2I}{dz'^2} + \beta^2 I\right)\Gamma(z,z')\, dz'=0 \tag{19}$$

This equation shows that as the antenna radius approaches zero, the first term of Equation (19) approaches a constant limit for all z, except $z = z_1$ or $z = z_2$. Sufficiently far from the ends this constant is small. The $\Gamma(z,z')$ factor in the second term is infinite at $z = z'$ and large in its vicinity; hence, the $\left(\frac{d^2I}{dz'^2} + \beta^2 I\right)$ factor must be small. Therefore, as the radius of the antenna approaches zero, $\left(\frac{d^2I}{dz'^2}+\beta^2 I\right)$ approaches zero, which implies $I(z)$ approaches a sinusoidal form.

2. The Sweep-Off Method

This method starts with Equation (15), the tangential field equation for a filament current, being integrated twice by parts. Then an approximation to the current distribution on a transmitting antenna of finite radius, assumed to be given by:

$$I(z') = A\cos\beta z' + B\sin\beta z' \tag{20}$$

is substituted into the integrated form of Equation (15) to yield:

$$E_z = \frac{j}{4\pi\omega\varepsilon}\left[I'(z_2)\frac{e^{-j\beta r_2}}{r_2} - I'(z_1)\frac{e^{-j\beta r_1}}{r_1} + I(z_2)\frac{\partial}{\partial z}\left(\frac{e^{-j\beta r_2}}{r_2}\right) - I(z_1)\frac{\partial}{\partial z}\left(\frac{e^{-j\beta r_1}}{r_1}\right)\right] \tag{21}$$

This equation is an exact expression for the electric field intensity parallel to a sinusoidal current filament. The antenna is then subjected to a compensating impressed field, $-E_z^i$, and the correction terms from the first approximation are computed. The name for this method results from the concept of 'sweeping-off' the surface of the antenna the residual tangential electric intensity by applying an equal and opposite intensity.

It should be noted here that although Equation (21) is an exact expression for E_z, that E_z does not vanish along the filament. This apparent dichotomy results from the erroneous assumption of uniform convergence for E_z. In actuality, the convergence of E_z is non-uniform at $\rho = 0$, where ρ is the distance from the filament. For an antenna radius $r = a$,

there exists a remainder term $I_1(z)$ in addition to $I(z)$; $I_1(z)$ is sufficient to cause $E_z(a) = 0$. As $a \to 0$, $I_1(z) \to 0$; consequently, its contribution to E_z for any fixed value of ρ, greater than a, will approach zero with a. In the limit, E_z is given by Equation (21) for $\rho > 0$, but at $\rho = 0$ Equation (21) does not hold.

3. Mode Theory of Antennas

This method is based on the solution of Maxwells Equations subject to boundary conditions at the antenna surface, and the surface of the source of power. The method consists of calculating modes of propagation consistent with the boundary conditions at the lateral surfaces of the antenna, then the modes consistent with free-space propagation. These modes are combined to satisfy all boundary conditions and the current is obtained as the sum of two components: the TEM or Principal wave, and the Complementary wave consisting of all higher order modes. The principal mode is governed by ordinary transmission line equations (in terms of distributed capacitance and inductance).

4. Discussion

Of the methods discussed above, 'Sweeping-Off' is the most elementary and consequently, the least precise. The Mode Theory of Antennas excites a current in the conductor for the TEM mode, and a current for the complementary wave, which is a sum of currents, one for each of the higher order modes excited. The excited modes are strongly dependent on

the geometrical configuration of the system; hence, a generalized solution requires a number of terms which rapidly approaches infinity. This overwhelming problem of accounting for all terms limits the attractiveness of this method.

The Integral Equation method appears most promising for generating a better approximation to the current. Many different approaches to solving the equation have been proposed and virtually all of them lend themselves to solution by digital computer. Three of these approaches will be discussed in the next section.

C. NUMERICAL ANALYSIS

1. Hallen's Approach

One of the earliest solutions to the Integral Equation was the approach proposed by Hallen,* the basis of which is successive approximations to the current. Hallen uses a traditional Green's Function along with a tacit assumption of a homogeneously distributed current** over the conductor surface. The 'E' field inside the conductor (expressed in terms of current and skin effect resistance) is equated to the

---

*Hallen's approach is relatively long; the details will not be presented here. For an outline of the method and a discussion of the important steps and results, see [Ref. 5].

**Hallen's tacit assumption is that the impressed voltage is distributed over a finite length [Ref. 3] (which, for a homogeneous conductor, implies a homogeneously distributed current). If the stated assumption of a driving potential discontinuity is strictly enforced, Hallen's method breaks down [Ibid.].

'E' field outside the conductor (expressed in terms of vector potential, 'A'). The wave equation is solved as a sum of a complimentary function and a particular integral. A constant, C_2, in the solution is evaluated in terms of input conditions at the terminals, and the vector potential, A, is expressed in terms of the antenna current. C_2 and A are inserted in the solution for the wave equation obtaining an Integral Equation in current, which is Hallen's Equation. A partial solution for the current is obtained by evaluating one of the integrals so the current is expressed as the sum of several terms, some of which also include the current, I. Neglecting certain terms in I, an approximate (zero order) solution is obtained for I. This value is substituted back in the current equation obtaining a first-order approximation. This process is continued to yield successively higher orders of solution. The process is stopped when a sufficient degree of accuracy is obtained, the constant C_1 (the coefficient for the quadrature term of current) is evaluated and an asymptotic expansion for the current is obtained.

2. Parabolic Interpolative Fit Approach

A more recent approach (1975) is one proposed by Chang et al, [Ref. 6]. Chang begins by assuming a surface current on the antenna (as opposed to a line current approximation) and defines a new Kernel (Green's) Function to account for axial variations in current. He also derives a different expression for E_z from the relationship:

$$E = -j\frac{1}{\omega\mu\varepsilon}(\nabla(\nabla\cdot\bar{A}) + \beta^2\bar{A}) \qquad (22)$$

which he claims is more accurate, since continuity of higher order derivatives of 'I' do not have to be specifically considered at segment boundaries when solving the Integral Equation. He then assumes a Parabolic Interpolative Fit for the current distribution over each segment (the distribution over the whole antenna is not necessarily parabolic) where precise values of current are exactly defined at sample points. He also defines three moment functions that describe the Kernel Function and its variation with respect to Φ and Z over a segment. The non-zero field points are then expressed as double summations of the moment functions over each interval. To avoid the double summations, he splits the Kernel Function into two factors (a technique used by Hallen, as well) which facilitates the computation of the dominant term (the result of which is a complete elliptic integral of the first kind), then redefines the Kernel as an elliptic integral plus an approximate remainder. With this Kernel he then computes the moment functions defined above while redefining a remainder term for three different special situations. These moment functions can now be evaluated numerically through adaptive integration techniques, such as Gauss-Legendre Quadrature, by splitting the integrand functions into Real and Imaginary parts.

3. Bessel Function Fit Approach

Another recent approach (1981) is that proposed by Balzano et al, [Ref. 7]. Balzano also begins by redefining the Kernel Function to account for azimuthal variations, but casts it into the form of an integral of a Hankel Function of the second kind, which also can be represented as an infinite summation of Bessel Functions. The magnetic vector potential is then expressed as a double integration of the current density on the conductor times the integral of the infinite summation of Bessel Functions described above. In this form, all that is needed is an accurate description of the axial current distribution, I(z') over the cylindrical antenna.

From the relationship of the vector potential with the E and H fields, an expression can be written for E_z as a function of the integral of I(z):

$$E_z(a,z) = -\frac{\eta}{8\pi k}\int_{-\infty}^{\infty} J_0(a\sqrt{k^2-\zeta^2})H_0^{(2)}(a\sqrt{k^2-\zeta^2}) \cdot (k^2-\zeta^2)\left(\int_0^h I(z')e^{j\zeta z}\,dz'\right)e^{-j\zeta z}\,d\zeta \qquad (23)$$

I(z') is expressed by a suitable linear combination of orthonormal functions which satisfy the boundary conditions for the current. Then the current expressed as an infinite sum of these orthonormal functions is equated to the Fourier Transform of the current expressed as a function of the vector potential:

$$\int_{o}^{h} I(z')e^{j\zeta z'}\, dz' = \sum_{n=1}^{N} A_n/\sqrt{h}\; \varepsilon_n(\zeta) \qquad (24)$$

where: $\varepsilon_n(\zeta)$ is the Fourier Transform of the current harmonics, A_n is an infinite series of constants. Equation (24) is substituted into Equation (23) and solved by applying Galerkins Method.* This yields an infinite system of equations which can be truncated and solved for the unknown A_n. A similar treatment can be applied to the other non-zero field equations to cast them into solvable form. However, the equations so defined converge slowly; therefore, additional manipulation is required. The additional manipulation becomes rather involved and will not be discussed here. Details can be found in Ref. 7.

4. Discussion

All three of the above methods are theoretically sound, all three give reasonable results over large portions of the near-field region, and all three lend themselves to numerical solution by computer. Of concern here is the amount of valuable computer resources (time, core, and cost) consumed in making these calculations. Balzano indicates the

---

*Galerkin's Method solves an Integral Equation via the Method of Moments to be discussed below. Specifically, Galerkin's Method sets the Weighting Functions equal to the Basis Functions.

expressions he derives for field components are slow in converging, and even after modifications to his basic derivation to hasten the convergence, he states that more than 1500 harmonics (a 1500th order linear system of equations) are needed to satisfactorily match boundary conditions.

Chang does not indicate directly the amount of computer resources consumed by his method, but he does imply his method is adopted because a simpler method (The Method of Moments) is inaccurate:

> "...in the numerical computation, the integral from -h to h is usually subdivided into a finite number of segments; in each segment the current is interpolated by a polynomial with coefficients expressible in terms of values of current at a few sample points within that segment. The higher derivatives of I(z) are therefore discontinuous at boundary points between any two segments." [Ref. 6]

One of the intentions of this study is to show that the Numerical Electromagnetics Code (NEC), which uses the Method of Moments, has been modified to account for the discontinuities of the first derivative at segment boundaries, and that this modification is sufficient to yield results that are accurate for engineering analysis.

III. DESCRIPTION OF NEC

NEC, Numerical Electromagnetics Code, is a computer program for the analysis of the electromagnetic response of antennas and other metal structures. It computes a numerical solution to integral equations that describe the currents induced on a structure by voltage or current generators and/or incident fields. It is the latest in a series of programs. The first, called BRACT, was developed by MBAssociates under funding from the Air Force Space and Missile Systems Command. This was followed by AMP, again developed by MBAssociates, this time under an Office of Naval Research contract. NEC evolved from AMP and was developed by Lawrence Livermore Laboratories with funding from the Naval Electronics Systems Command. It is a user friendly code which incorporates the following:

A. FEATURES OF THE CODE

An Integral Equation (I.E.) for modeling the current on smooth surfaces is combined with an I.E. for current modeling on thin wires to describe the electromagnetic response of an arbitrary structure. The structure, or parts of it, may be active or passive, located over a perfect or imperfect ground plane, and may have lumped-element or distributed loading. Excitation may be from voltage or current sources on the

structure, an incident plane wave with either linear or elliptic polarization, or the field may be due to a Hertzian dipole. Output may include current and charge density, power gain or directive gain, near- or far-zone electric or magnetic fields, impedance or admittance, total radiated power or input power. It is suitable for either antenna analysis or cross-section scattering and electromagnetic pulse (EMP) studies. The code will handle junctions of wires of uneven radius, free ends of wires that have finite radius, wires of variable radius, and coupling between wires.

NEC utilizes the Gauss-Doolittle Method for solving the matrix equations generated by the Method of Moments when solving the integral equations. It also allows for use of rotational or plane symmetry to reduce computation time. When the impedance matrix is too large to be contained in core, NEC has the option of storing portions out of core. It allows the 'self-interaction matrix' for a structure to be computed, factored for solution, and stored on tape or file. A solution for a new antenna that enters this environment requires only the evaluation of the 'self-interaction matrix' for the antenna, the mutual antenna to environment interactions, and matrix manipulations for a partitional matrix solution.

B. ZONING CONSIDERATIONS

NEC is a discrete sampling code where a complex structure must be dissected into a number of simple elements (wires or

plates) to which the Electric Field Integral Equation (EFIE) or Magnetic Field Integral Equation (MFIE) are applied. As with any description of the real world, there are approximations, but because of the versatility in modeling the geometry of a structure, its approximations more closely resemble nature. The resemblance is strongly influenced by the choice of zoning (i.e. dissecting) the structure in the program. The smaller the geometric elements, the closer the model comes to reality. However, the smaller the elements, the larger the number of elements, which means the larger the matrix of equations and hence, the more costly the solution. There is a point beyond which smaller zones do not yield a substantially more accurate solution; it may be necessary to rerun the problem with increasingly smaller elements to find the point of diminishing returns. The choice of proper zoning then is gained with experience and becomes as much of an art as it is a science. The guidelines for the science aspect are as follows.

1. Wires

Segments should follow the paths of conductors using a piece-wise linear fit on curves. Generally, segment lengths (Δ) should be less than $.1\lambda$; shorter segments ($.05\lambda$) or less may be needed at critical regions (junctions or curves). Segments smaller than $10^{-3}\lambda$ should be avoided since the similarity of constant and cosine components lead to numerical inaccuracy. The radius of the wire (a) relative to

λ depends on the Kernel used in the Integral Equation. Two options exist. The thin-wire Kernel models a filament current, while the extended Kernel models a uniform current distribution around the segment surface. The field of the distributed current is approximated by the first two terms in a series expansion of the exact field, in powers of a^2. The first (a^0) term is identical to the thin-wire Kernel; the second term extends the accuracy for larger values of a. Both Kernels incorporate the thin-wire approximations (see Section II.A) and both require $2\pi a/\lambda<<1$. The thin-wire Kernel requires a $\Delta/a>8$; the extended Kernel relaxes this to $\Delta/a>2$. These values ensure errors are less than 1%. The extended Kernel is used at free wire ends and between parallel, connected segments. The thin-wire Kernel is always used at bends.

2. Surfaces

A conducting surface is modeled by small flat surface patches which conform as closely as possible to curved surfaces. The parameter defining a patch is a normal unit vector, originating from the center of the patch, defined in Cartesian coordinates. Each patch must be connected by a wire at the patch center for the program to integrate the surface current. The code divides each patch into four equal patches about the wire end, along the unit vector lines describing the surface of the patch. An interpolation function is applied to the four patches to represent placement of the current onto the

patches, and the function is numerically integrated. Patches with wires connected to them (active patches) should be chosen to be approximately square with sides parallel to the unit vectors defining the surface. Only one wire may connect to a patch, that wire may not be connected to another patch, and it may not lie in the plane of the patch. A minimum of about 25 patches should be used per wavelength of surface area; the maximum size for an individual patch is about .04 square wavelengths. The number of patches used increases, and the size of each patch decreases, as the radius of curvature decreases. Smaller patches should be used at edges since the current amplitude may vary rapidly in this region. Long narrow patches should be avoided. Patches are restricted to modeling voluminous bodies with closed surfaces; parallel surfaces on opposite sides cannot be too close together.

3. Ground Plane

For a perfectly conducting ground, the code generates a reflected image. Structures may be close to, or contact, the ground; however, for a horizontal wire: $\sqrt{h^2 + a^2} > 10^{-6}\lambda$ where a = wire radius, h = height of wire axis above the ground plane, and $h/a \gtrsim 3$.

A finitely conducting ground may be modeled by an image modified by the Fresnel Plane-wave Reflection coefficients. This method is fast, but of limited accuracy and should not be used for structures close to the ground, or

having a large horizontal extent over the ground. The Sommerfeld/Norton model uses the exact solution and is accurate close to the ground; the horizontal restriction is the same as for a perfect ground. This model is only used for wire-wire interactions, for surfaces the code reverts to Fresnel Reflection coefficients. At the present time, a ground stake cannot be used, but wires may end on a perfectly conducting ground plane if the derivative of the current at the end of the wire is zero. For wires, there are options for a radial-wire ground screen approximation and a two-medium ground approximation based on modified reflection coefficients. These options allow considerable savings in computational time when limited accuracy can be tolerated.

C. INTEGRAL EQUATIONS

1. Electric Field Integral Equation (EFIE)

The EFIE is used for thin-wire structures with small conductor volume. It is derived from the electric field representation for a current distribution confined to the surface of a perfectly conducting body:

$$\overline{E}(\overline{r}) = -j \frac{\eta}{4\pi\beta} \oint_S \overline{J}_S(\overline{r}') \, \overline{\overline{G}}(\overline{r},\overline{r}') \, dA' \qquad (25)$$

where: $\overline{r}'$ is the source point, $\overline{r}$ is the observation point, $\overline{J}_S$ is a surface current density, $\overline{\overline{G}}(\overline{r},\overline{r}') = (\beta^2\overline{\overline{I}} + \nabla\nabla)g(\overline{r},\overline{r}')$, $g(\overline{r},\overline{r}') = e^{-j\beta|r-r'|}/|r-r'|$, β = phase velocity, η = intrinsic

impedance of medium. The principal value integral $⨍_S$ is indicated so $\bar{r} \to \bar{r}'$ in the limit.

An integral equation for the current induced on S by an incident field E^i can be obtained from Equation (25) and the boundary condition:

$$\hat{n}(\bar{r}) \times [\bar{E}^i(\bar{r}) + \bar{E}^s(\bar{r})] = 0 \tag{26}$$

where $r \varepsilon S$, $\hat{n}(\bar{r})$ is the unit normal vector at $\bar{r}$, $\bar{E}^s$ is the field due to the induced current $\bar{J}_s$. This integral equation is given by:

$$-\hat{n}(\bar{r}) \times \bar{E}^i(r) = -j \frac{\eta}{4\pi\beta} \hat{n}(\bar{r}) \times ⨍_S \bar{J}_s(\bar{r}') \cdot (\beta^2 \bar{\bar{I}} + \nabla\nabla) g(\bar{r},\bar{r}')\, dA' \tag{27}$$

This vector integral equation is reduced to a scalar integral equation for the thin-wire model. With the surface current density replaced by a filament current and the boundary condition enforced in the axial direction, this gives:

$$-\hat{s} \cdot \bar{E}^i(\bar{r}) = -j \frac{\eta}{4\pi\beta} \int_L I(s')(\beta^2 \hat{s} \cdot \hat{s}' - \frac{\partial^2}{\partial s \partial s'}) g(\bar{r},\bar{r}')\, ds' \tag{28}$$

where: $\hat{s}$ = distance along the wire axis at r, and $\hat{s}'$ = unit vector along the wire axis. This is the EFIE solved by NEC.

2. Magnetic Field Integral Equation (MFIE)

The MFIE is derived from the integral representation for the Magnetic field of a surface current distribution $\bar{J}_s$:

$$\bar{H}^s(\bar{r}) = \frac{1}{4\pi} \int_s \bar{J}_s(\bar{r}) \times \frac{\partial}{\partial r'} \; g(\bar{r},\bar{r}')\, dA' \tag{29}$$

If $\bar{J}_s$ is induced by an external incident field $\bar{H}^i$, then the total magnetic field inside the perfectly conducting surface must be:

$$\bar{H}^i(\bar{r}) + \bar{H}^s(\bar{r}) = 0 \tag{30}$$

where: $\bar{H}^i$ is the incident field, and $\bar{H}^s$ is the scattered field. Let $r \rightarrow r_o$ along $\hat{n}(\bar{r}_o)$ from inside the surface, then Equation (30) with Equation (29) substituted becomes:

$$-\hat{n}(\bar{r}_o) \times \bar{H}^i(\bar{r}_o) = \hat{n}(\bar{r}_o) \times \frac{1}{4\pi} \lim_{r \rightarrow r_o} \int_s \bar{J}_s(\bar{r}') \times \frac{\partial}{\partial r'} g(r,r')\, dA' \tag{31}$$

The limit is evaluated using a result of potential theory to yield:

$$-\hat{n}(\bar{r}_o) \times \bar{H}^i(\bar{r}_o) = -1/2\bar{J}_s(\bar{r}_o) + \frac{1}{4\pi} \fint_s \hat{n}(\bar{r}_o)$$

$$\times[\bar{J}_s(\bar{r}') \times \frac{\partial}{\partial r'} g(\bar{r}_o,\bar{r}')]\, dA' \qquad (32)$$

This vector is resolved into two scalar equations along the orthogonal surface vectors $\hat{t}_1$ and $\hat{t}_2$, where:

$$\hat{t}_1(\bar{r}_o) \times \hat{t}_2(\bar{r}_o) = \hat{n}(\bar{r}_o) \qquad (33)$$

which are given by:

$$\hat{t}_2(\bar{r}_o)\cdot\bar{H}^i(\bar{r}_o) = -1/2\ \hat{t}_1(\bar{r}_o)\cdot\bar{J}_s(\bar{r}_o)$$

$$- \frac{1}{4\pi} \fint_s \hat{t}_2(\bar{r}_o)\cdot[\bar{J}_s(\bar{r}') \times \frac{\partial}{\partial r'} g(\bar{r}_o,\bar{r}')]dA'$$

$$(34)$$

and

$$-\hat{t}_1(\bar{r}_o)\cdot\bar{H}^i(\bar{r}_o) = -1/2\ \hat{t}_2(\bar{r}_o)\cdot\bar{J}_s(\bar{r}_o) +$$

$$+ \frac{1}{4\pi} \fint_s \hat{t}_1(\bar{r}_o)\cdot[\bar{J}_s(\bar{r}') \times \frac{\partial}{\partial r'} g(\bar{r}_o,\bar{r}')]dA'$$

$$(35)$$

3. Hybrid EFIE/MFIE

NEC models thin wires using EFIE and for surfaces uses MFIE. For a structure with both wires and surfaces, $\bar{r}$ in Equation (28) is restricted to the wires, with the integral for $\bar{E}^S(\bar{r})$ extending over the complete structure. Hence, Equation (28) is used for wires, while the more general form, Equation (27) is used for surfaces. Likewise, $\bar{r}_o$ is restricted to surfaces in Equation's (34) and (35), with the integrals for $\bar{H}^S(\bar{r})$ extending over the complete structure. The resulting coupled integral equations are:

For $\bar{r}$ on wire surfaces:

$$-\hat{s}\cdot\bar{E}^i(\bar{r}) = -j\,\frac{\eta}{4\pi\beta}\int_L I(s')\cdot[\beta^2\hat{s}\cdot\hat{s}' - \frac{\partial^2}{\partial s\partial s'}]g(\bar{r},\bar{r}')\,ds'$$

$$-j\,\frac{\eta}{4\pi\beta}\int_{S_1} J_s(\bar{r})\cdot[\beta^2\hat{s}-\frac{\partial}{\partial r'}\cdot\frac{\partial}{\partial s}]g(\bar{r},\bar{r}')\,dA' \tag{36}$$

For $\bar{r}$ on surfaces excluding wires:

$$\hat{t}_2(\bar{r})\,\bar{H}^i(\bar{r}) = -\frac{1}{4\pi}\,\hat{t}_2(\bar{r})\cdot\int_L I(s')[\hat{s}'\ X\ \frac{\partial}{\partial r'}\ g(r,r')]\,ds'$$

$$-\ 1/2\ \hat{t}_1(\bar{r})\cdot\bar{J}_s(\bar{r}) - \frac{1}{4\pi}\ -\!\!\!\!\!\!\int_{S_1}\hat{t}_2(\bar{r})$$

$$\cdot\ [\bar{J}_s(\bar{r}')\ X\ \frac{\partial}{\partial r'}\ g(\bar{r},\bar{r}')]\,dA' \tag{37}$$

and

$$-\hat{t}_1(\bar{r}) \cdot \bar{H}^i(r) = \frac{1}{4\pi} \hat{t}_1(\bar{r}) \cdot \int_L I(s')[s' \text{ X } \frac{\partial}{\partial r'} g(\bar{r},\bar{r}')] \, ds'$$

$$-1/2\hat{t}_2(\bar{r}) \cdot \bar{J}_s(\bar{r}) + \frac{1}{4\pi} \fint_{S_1} \hat{t}_1(\bar{r})$$

$$\cdot \, [\bar{J}_s(\bar{r}') \text{ X } \frac{\partial}{\partial r'} g(\bar{r},\bar{r}')] \, dA' \qquad (38)$$

D. METHOD OF MOMENTS AND THE MATCH POINT

The Method of Moments is a technique whereby an integral equation is reduced to a system of linear algebraic equations which are easily handled by high speed digital computers.

1. Mathematical Concept

The method applies to an inhomogeneous linear operator of the form:

$$L \bar{f} = \bar{e} \qquad (39)$$

where L is a linear operator with domain D_L containing the function $\bar{f}$, which is an unknown response to an excitation $\bar{e}$, which is given, and found in the range of L.

If a solution to Equation (39) exists and is unique for all $\bar{e}$, then the inverse operator, L^{-1}, exists such that:

$$\bar{f} = L^{-1}\bar{e} \qquad (40)$$

which represents a solution to Equation (39).

The unknown function, $\overline{f}$, may be expanded in a series of N linearly independent Basis Functions spanning D_L as:

$$\overline{f} = \sum_{j=1}^{N} a_j \overline{f}_j \qquad (41)$$

Substituting Equation (41) into Equation (39), and taking the inner product with a set of linearly independent weighting functions $\{w_i\}$, defined in the range L and spanning sub-space S_w, results in a set of equations for the coefficients, a_j, of Equation (41). This set of equations:

$$\sum_{j=1}^{N} a_j <w_i, Lf_j> = <w_i, e> \qquad i = 1, 2, \ldots N \qquad (42)$$

can be written in matrix notation as:

$$[G]\,[A] = [E] \qquad (43)$$

where: $G_{ij} = <w_i, Lf_j>$, $A_j = a_j$, and $E_i = <w_i, e>$. This procedure projects the space of $\overline{e}$ onto the sub-space S_w, and enforces the equality between projections.

Hence, if a solution to Equation (43) exists and is unique for all $\overline{e}$, then the inverse operator, L^{-1}, also exists such that:

$$[A] = [G]^{-1} [E] \tag{44}$$

which is a solution to Equation (43).

The efficiency of computations and accuracy of solution is largely dependent on the choice of Basis Function. Factors which should guide this choice are:

a) accuracy of solution desired

b) ease of evaluation of matrix elements

c) size of the matrix that can be inverted

d) the realization of a 'well-conditioned' matrix.

There are two general classes of Basis Functions from which to choose, entire domain and sub-domain. The sub-domain class has fewer elements; hence, its execution time is less, it simplifies the evaluation of the inner product integral and still ensures the matrix [G] will be 'well-conditioned'.

2. NEC's Application

NEC's interpolation of current on wires enforces continuity of current and linear charge density at segment ends. This imposes additional restrictions on the current and its derivative with respect to distance along the conductor. NEC forces the current on the conductor to match the integral equation at specific points; these 'match points' are located at the center of each segment.

NEC's application of the Method of Moments starts with the Integral Equations: Equation's (28) and (34) to

(35), or Equation's (36) to (38); the equation selected depending on the structure being modeled. These integral equations are the basis from which the system of linear equations will be generated.

A source model with a known excitation voltage can be related to the E-field impressed on the antenna; hence, E^i (= $\overline{e}$ from Equation (39)) is known. We know we are locking for a more accurate description of the current distribution on the antenna; hence, the current I (= $\overline{f}$ from Equation (39)) is the unknown response. The operator L (an integral operator in this case) is the composite of all other terms/factors (other than E and I) found in the integral equations. Hence, these terms can be cast into the form of Equation (39) as:

$$E^i = L\ I \tag{45}$$

To generate the system linear equations, we have divided the structure to be modeled into a number of segments according to the zoning guidelines discussed above. The current distribution on the antenna is now approximated as the summation of currents found on each segment. That is:

$$I = \sum_{j=1}^{N} I_j\ g_j \tag{46}$$

which has the same form as Equation (41). Here g_j are the Basis Functions and I_j is the system of coefficients. For wires:

$$I_j g_j = A_j + B_j \sin(\beta(s-s_j) + C_j \cos(\beta(s-s_j))^* \tag{47}$$

where: s_j = center of the jth sub-section, and β = free space wave number. As a result of current continuity considerations at segment ends, each sub-section will have only one unknown.

For patches, the surface current density is:

$$\bar{J}_s(\bar{r}) = \hat{u}\, K_{uj} + \hat{v}\, K_{vj} \tag{48}$$

where: K_{uj} and K_{vj} are vector components of the surface current density, $\bar{J}_s(\bar{r})$, on each patch. Each K_j is constant over the patch, which is usually rectangular, but can be any reasonable shape. Again, current continuity considerations for the patch yield only two unknowns, one for each direction.

Because of the nature of the Kernel functions in the integral equations, the choice of basis functions is more critical on wires than on surfaces.

---

*This form has been found to provide rapid solution convergence and fields of sinusoidal currents are easily evaluated in closed form.

For simplicity, the rest of this section will be restricted to the case for only wires, as this is in consonance with the system for this study. Assuming the wire is aligned with the z-axis (as it is in this study), Equation (45) can be re-written as:

$$E^i(z) = L\, I\, (z') \tag{49}$$

where the z' indicates the current is on the surface of the wire. Equation (46) can be rewritten as:

$$I(z') = \sum_{j=1}^{N} I_j\, g_j(z') \tag{50}$$

Equation (50) defines the set of sub-domain basis functions to be used in computations. For finite N, the sum of $I_j\, g_j(z')$ cannot exactly equal the general current distribution*, so the $I_j\, g_j(z')$ need to be chosen as close to the actual distribution as possible. This is accomplished by restricting the support for $I_j\, g_j(z')$ to a localized region of the surface near the center of the segment. Each basis function has a peak on the segment on which it is defined and extends only

---

*The approximation can be brought arbitrarily close to the exact solution by choosing N sufficiently large. Fortunately, reasonable accuracy can be obtained, in most cases, with a relatively small number of segments ($N \cong 10/\lambda$).

onto segments to which it is directly connected, going to zero with zero derivative at the outer ends of connected segments.

Equation (50) is then substituted into Equation (49) to give:

$$E^{i}(z) = L\left[\sum_{j=1}^{N} I_j \, g_j(z')\right] = \sum_{j=1}^{N} I_j \, L[g_j(z')] \qquad (51)$$

where: I_j and the summation have been moved outside the domain of L as a result of its linearity.

The next task is to identify a set of weighting functions, $\{w_i\}$. When the weighting functions are set equal to the basis functions (i.e. $w_i = g_i$), this is known as Galerkins Method.* In NEC, w_i is chosen as a set of Dirac Delta Functions:

$$w_i(z) = \delta\left(z - \frac{\Delta i}{2}\right) \qquad (52)$$

where: $\frac{\Delta i}{2}$ is the set of match points found at the center of each segment Δi. Use of this weighting function results in a point sampling of the integral equations known as the "collocation method" of solution.

---

*Employed in Hallen's approach (See Section II.C.1)

Using this weighting function (Equation (52)) and taking the inner product of each side of Equation (51) gives:

$$<w_i, E^i(z)> = \sum_{j=1}^{N} I_j <w_i, L[g(z')]> \qquad (53)$$

which has the form:

$$[V] = [I] [Z] \qquad (54)$$

where: [V] is a matrix of weighting functions applied to the known impressed field, [I] is a matrix of unknown coefficients, and [Z] is a mapping matrix of weighting functions applied to the assumed basis functions.

From previous arguments, we know that if a solution to Equation (54) exists and is unique for all E^i, then Equation (54) can be transposed to:

$$[I] = [Z]^{-1} [V] \qquad (55)$$

In this form, the system of equations can be solved by imposing the boundary condition:

$$E_z^i + E_z^s = 0 \qquad (56)$$

on E^i, which then states that the tangential scattered field, E_z^s (which generates the current), is equal to the negative of the known impressed field, E_z^i. Stated in equation form:

$$E_z^i = -E_z^s \tag{57}$$

Hence, the system of equations can be solved for the exact current at the match points, and by enforcing current and charge continuity at segment ends, a very close approximation to the actual current distribution can be obtained.

Equation (54) is solved by the Gauss-Doolittle method. In this method the matrix [Z] is defined as two sub-matrices:

$$[Z] = [{}^{A}_{B}] \tag{59}$$

where sub-matrix [A] with elements A_{ij} represents the electric field at the center of segment i due to the jth basis function, centered on segment j. Sub-matrix [B], with elements B_{ij}, represents magnetic fields generated by segment basis functions. In the execution of this method, the matrix [Z] is factored into the product of an upper triangular matrix [U] and a lower triangular matrix [L]. That is:

$$[Z] = [L]\,[U] \tag{59}$$

Equation (54) then becomes:

$$[V] = [I]\,[L]\,[U] \qquad (60)$$

and [I] is computed in two stages:

$$[V] = [L]\,[F] \qquad (61)$$

and:

$$[F] = [U]\,[I] \qquad (62)$$

where Equation (61) is solved first for [F] (an intermediate matrix) by forward substitution, and then for [I] by backward substitution.

Now that the current has been determined, the other non-zero scalar field components (E_r and H_ϕ) can easily be computed.

IV. MODEL DESCRIPTION AND COMPUTATIONAL RESULTS

A. MODEL DESCRIPTION

The basic model used for this study is a simple monopole colinear with the Z-axis and mounted perpendicular to a perfectly reflecting ground plane, that is itself located in the X-Y plane. As can be seen from Figure 1, the antenna is 75 meters in height and .6 meters in diameter. It is radiating at a frequency of 1 Megahertz (the middle of the AM broadcast band) with a wavelength ($\lambda = c/f$) of 300 meters; it is a quarter-wavelength monopole operating at its resonant frequency. Transmit power is fed to the model through its base by a voltage that is normalized to obtain 1000 watts of radiated power.

Virtually all modeling schemes start from the basic premise that E- and H-field component values can be determined from a knowledge of the current distribution on the antenna. Three generalized methods for describing the current distribution will be discussed here: 1) assuming a current distribution, 2) modal modeling, and 3) sub-domain modeling.

1. Assumed Current Distribution

This is the classical method as described in [Ref. 4]. Typically, the assumed distribution is sinusoidal, which results in a tangential E-field component substantially different from zero. This may not cause a significant error in

the far-field, but in the near-field where stored energy strongly depends on the current shape, large errors generally occur.

2. Modal Modeling

To improve on the assumed distribution, the modal modeling method was devised. By this method the current distribution can be described as the sum of an infinite system of equations which precisely describe the current distribution in the limit. This is the approach used by Balzano [Ref. 7]. Using an infinite series of Bessel-Fourier Integrals, which can be truncated to allow for desired accuracy, a system of closed form equations can be generated which lend themselves to computer solution. This method enforces boundary conditions (i.e. $E_z = 0$) over the surface of the antenna with precision (in the limit), but there is a practical limitation that must be imposed on the size of the system of equations that precludes an exact solution. If the current is expressed by a sum of harmonics, the total number of harmonics which must be used in the computations to match boundary conditions is related to the ratio of dipole height to gap size.

3. Sub-domain Modeling

To avoid much of the mathematical complexity of modal modeling, sub-domain modeling divides a given structure into a concatenated series of sub-structures, or elements. The actual current distribution on the given structure is

approximated by geometric distributions (sin, cos, and linear constants) on the elements. This is the method used by NEC [Ref. 2]. The NEC code uses the scalar form of the integral equations to determine the current in each of the elements, then combines the results from each substructure to deduce the performance of the total structure.

B. MODEL CONFIGURATIONS

In this study three configurations of the model were assumed and values for the tangential, radial, and peak (time and spatial) fields were calculated for each. The three configurations were for a structure modeled with 5, 15, and 25 sub-domains. In each of the configurations, a null value for the tangential E-field was imposed at the center point of each sub-domain (this point is called the match point). Since a closed form solvable function has not been identified which describes the current on the antenna, while maintaining a tangential E-field equal to zero, it has become necessary to approximate the current distribution. This is done in NEC through the Method of Moments as discussed in Section III.D. Using this method the current can be approximated to an arbitrary degree of accuracy by increasing N. Fortunately, reasonable accuracy is obtained in most situations with a relatively small number of segments, typically $N = 10/\lambda$.

C. EXPECTATIONS/OBSERVATIONS/ANOMALIES

This study utilized three configurations to determine two relevant facts: a) whether the calculated value of the near-field was dependent on the number of segments used, and b) whether the size of the segment conformed to the guidelines used in the far-field.

A non-analytic overview of the plots generated by this study indicated that the calculated value of the near-field was independent of the number of segments into which the structure was divided. This was determined by overlaying plots of five and fifteen segments on a twenty-five segment plot. An example of one of these plots is shown in Figure 4. The spurious field emitted from the base of the antenna has significantly different values. These variations were the result of using different values of input voltage, when the configuration was changed, to maintain a normalized radiated power output of 1000 watts.* The values along the antenna and at its top are essentially the same, for respective positions on the antenna, for all three configurations.

The NEC manual [Ref. 2] recommends segment lengths (Δ) less than $\lambda/10$ for normal modeling, and for critical regions a $\Delta < \lambda/20$ is recommended. For a wavelength of 300 meters as used in this study, segment lengths of $\Delta < 300/10 = 30$

---

*Radiated power depended on the magnitude of the E-Field in each segment, which in turn depended on the segment length.

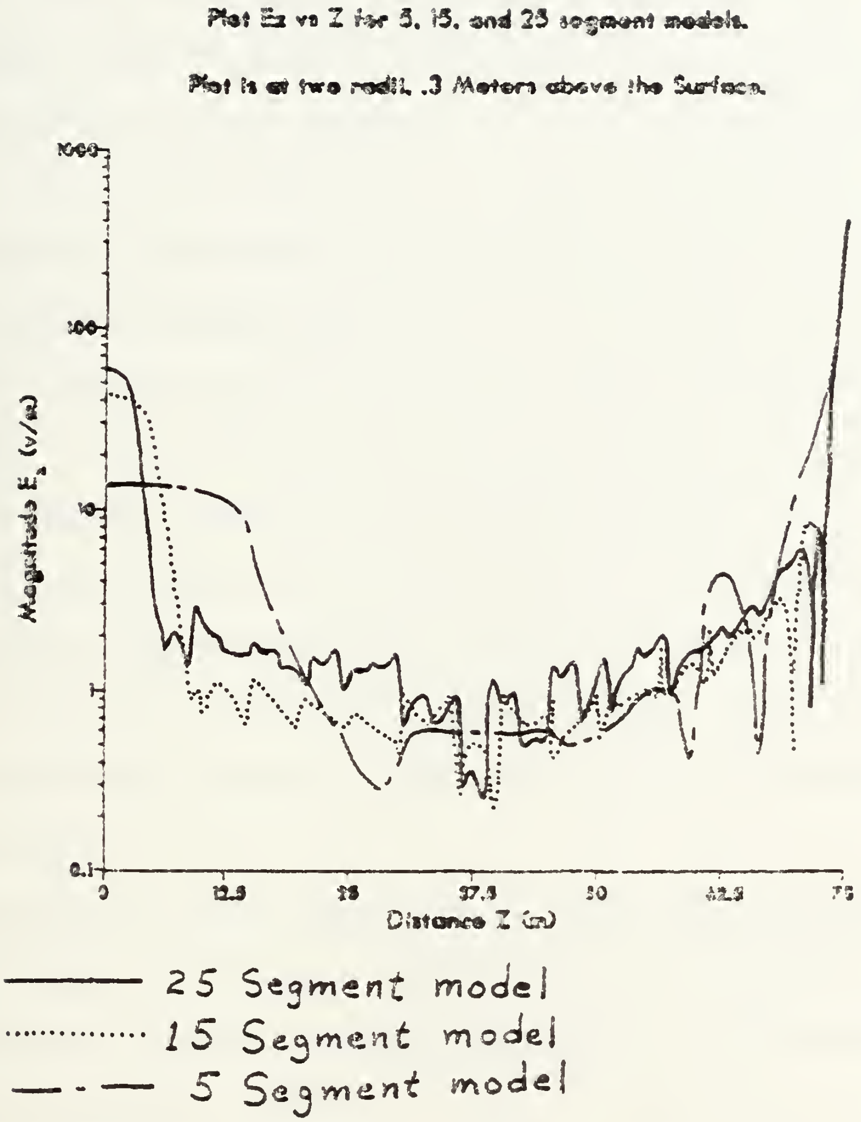
Plot Ez vs Z for 5, 15, and 25 segment models.
Plot is at two radii, .3 Meters above the Surface.
1000
100
10
1
0.1
Magnitude E_z (v/m)
0
12.5
25
37.5
50
62.5
75
Distance Z (m)
25 Segment model
15 Segment model
5 Segment model

Figure 4

meters, or $\Delta < 300/20 = 15$ meters are suggested. Lengths used in each configuration were: $\Delta_1 = 75/5 = 15$ meters, $\Delta_2 = 75/15 = 5$ meters, and $\Delta_3 = 75/25 = 3$ meters. Again, from a non-analytic overview of plots similar to Figure 4, it was determined that reasonable additional resolution was obtained in going from a five segment to a fifteen segment configuration (i.e. $\Delta = 15$ meters to $\Delta = 5$ meters), but the increased resolution in going from the fifteen segment to the twenty-five segment configuration (i.e. $\Delta = 5$ meters to $\Delta = 3$ meters) was not justified by the increased computer resources it consumed. From this observation it could be concluded that smaller segment lengths are required for near-field calculations, and that the lengths are on the order of 1/5 the value specified for the far-fields (i.e. $\Delta<\lambda/50$ for normal situations and $\Delta<\lambda/100$ for critical areas). Additional tests and models should be run to modify, or confirm this observation.

Intensity of the near-field is independent of the segment size, but smaller segment size is required to get a resolution of how that intensity varied as a function of position along the antenna. Based on these observations, a determination was made to restrict all further discussion to the fifteen segment configuration to avoid duplication of effort.

In the course of the investigation, plots of the E- and H-fields as a function of distance along the Z-axis were run

from the base of the monopole to its height, and also from the base to twice the height of the monopole. The plots to just the height of the monopole were run to obtain increased resolution as a function of position along the monopole. Examination of the single and double height plots, side by side, revealed no increased resolution or additional information was obtained from a single height plot that was not available on the double height plot, so only plots to twice the antenna height are discussed in this section.

Additionally, closely spaced plots within a segment were run to determine if there was any variation as a function of intra-segment position. This type of plot was run at the center of the antenna for: a) the end of a segment, b) the center of a segment, and c) a position half-way between the positions described in a) and b). This type of plot was also run for: a) the top of the antenna, b) a quarter of a segment above and below the top, and c) a half a segment above and below the top. In both cases, there was no observable difference in the a), b), or c) plots. Consequently, they have not been included in the discussion of plots that follows.

As a result of the above culling, the following are the plots included in Appendix A:

1. E-field plots (E_z, E_r, E_{peak}) as a function of Z to twice the height of the monopole, at distances of 1, 2, 5, 10, 100, and 1000 radii from the axis.

2. E-Field plots (E_z, E_r, E_{peak}) as a function of R to a distance of one (1) wavelength from the monopole, for heights of 2/100ths, 1/4, 1/2, 1, and 2 times the height of the monopole.

3. H-field plots (H) as a function of Z to twice the height of the monopole, at distances of 1, 2, 5, 10, 100, and 1000 radii from the axis.

4. H-field plots (H) as a function of R to a distance of one (1) wavelength for heights of 2/100ths, 1/4, 1/2, 1, and 2 times the height of the monopole.

Each of these categories are discussed in further detail below.

1. E(Z) Plots

As shown in Figure 5, $E_z(Z)$ along the antenna surface was much lower in magnitude (about 60 dB lower) than its value at the top. These lower values varied by an order of magnitude as a result of NEC forcing $E_z = 0$ at match points and approximating values (from the current distribution) elsewhere. These radical variations were quickly attenuated as the observation point (O.P.) moved away from the surface. At a distance of five radii (Figure 6), the integrating effect of a wider field of view had essentially smoothed out the curve, and also decreased the difference in magnitude between values at the top of the antenna and those along its length. When the O.P. moves to a distance of 100 radii, the integrating effect will have created an almost uniform magnitude along

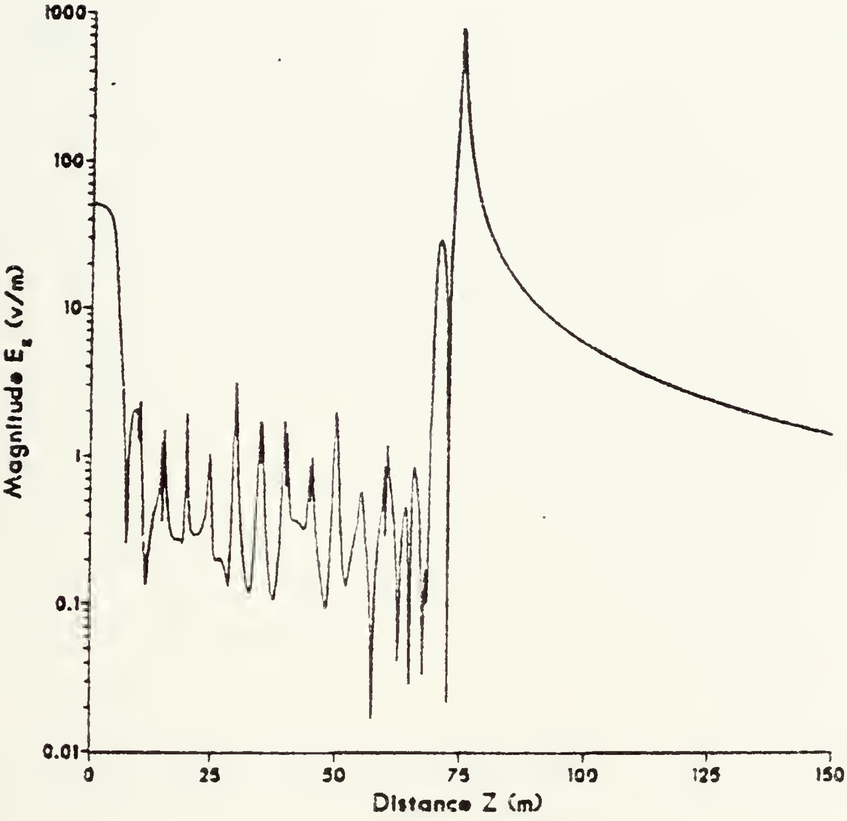
Plot Ez vs Z for a model of 15 segments.

Plot is at one radius, the Surface of the Monopole.

Figure 5

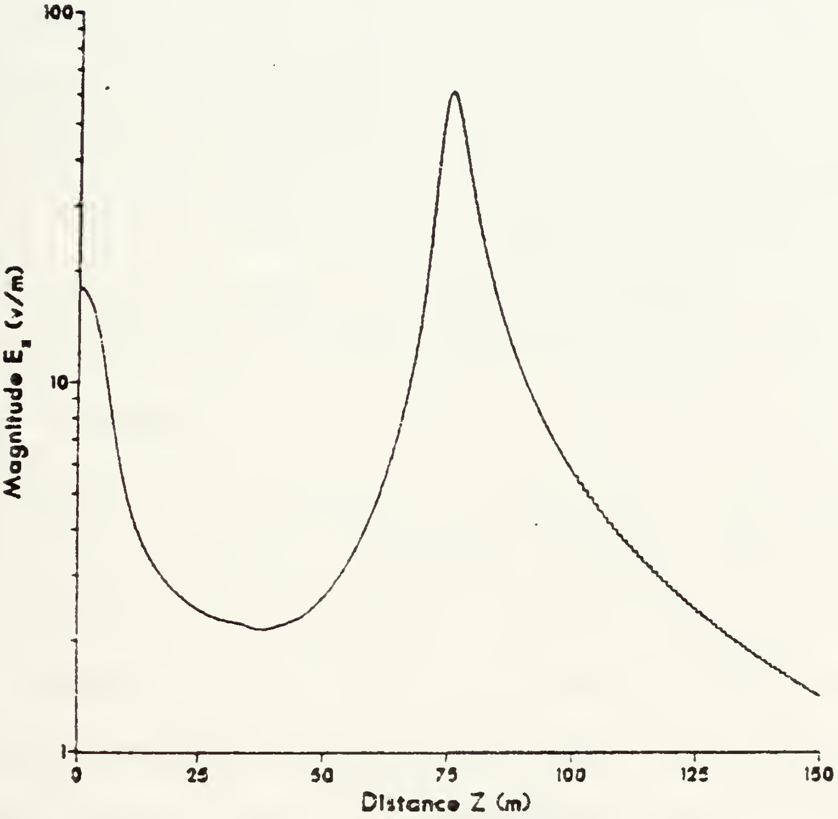

Plot Ez vs Z for a model of 15 segments.

Plot is at ten radii. 2.7 Meters above the Surface.

Figure 6

the antenna, and this uniform magnitude will continue to decrease in absolute value as the distance of the O.P. moves radially from the antenna.

The magnitude of E_z and E_r are approximately equal at the top of the monopole, but E_r maintains a value within an order of magnitude of its peak value all along the antenna surface (Figure 7). As a result of boundary conditions on E_r for the ground plane (similar to those for E_z on the antenna surface), the magnitude of E_r quickly approaches zero at the base. The shape of this curve remains pretty much the same as observations are made at greater distances. The magnitude of the curve decreases slowly and approaches a uniform value along the antenna.

E_{peak} is a composite of E_r and E_z. Near the antenna, plots of E_{peak} (Figure 8) strongly resemble plots of E_r. This implies that E_r is the dominant component in the near-field region. However, as the O.P.'s are moved further outward, the E_{peak}/E_r resemblence fades and there is a point around $\lambda/2\pi$ (see Figure 9) where the dominance begins to shift to E_z. When E_z becomes completely dominant, the value of E_{peak} is approaching a uniform value along the antenna. This results from the electromagnetic waves, generated by the point source at the top of the antenna, approaching a plane wave front at large distances. Also noted in Figure 9 is the sharp decline of E_z above the height of the antenna. This indicates very little radiation in the axial direction, the

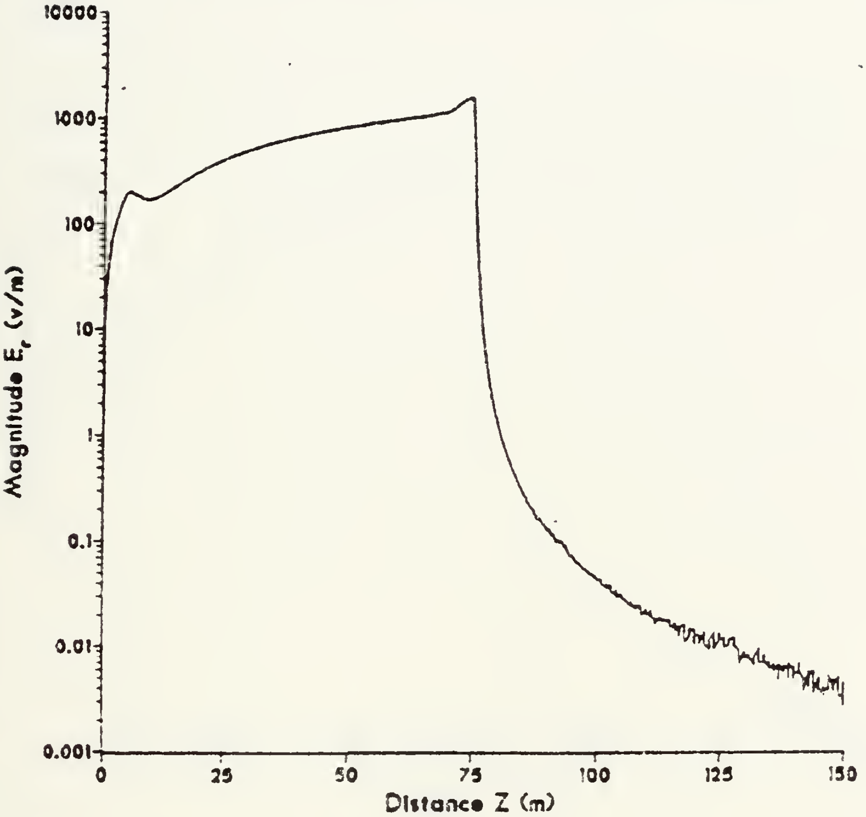

Plot Er vs Z for a model of 15 segments.

Plot is at one radius, the Surface of the Monopole.

Figure 7

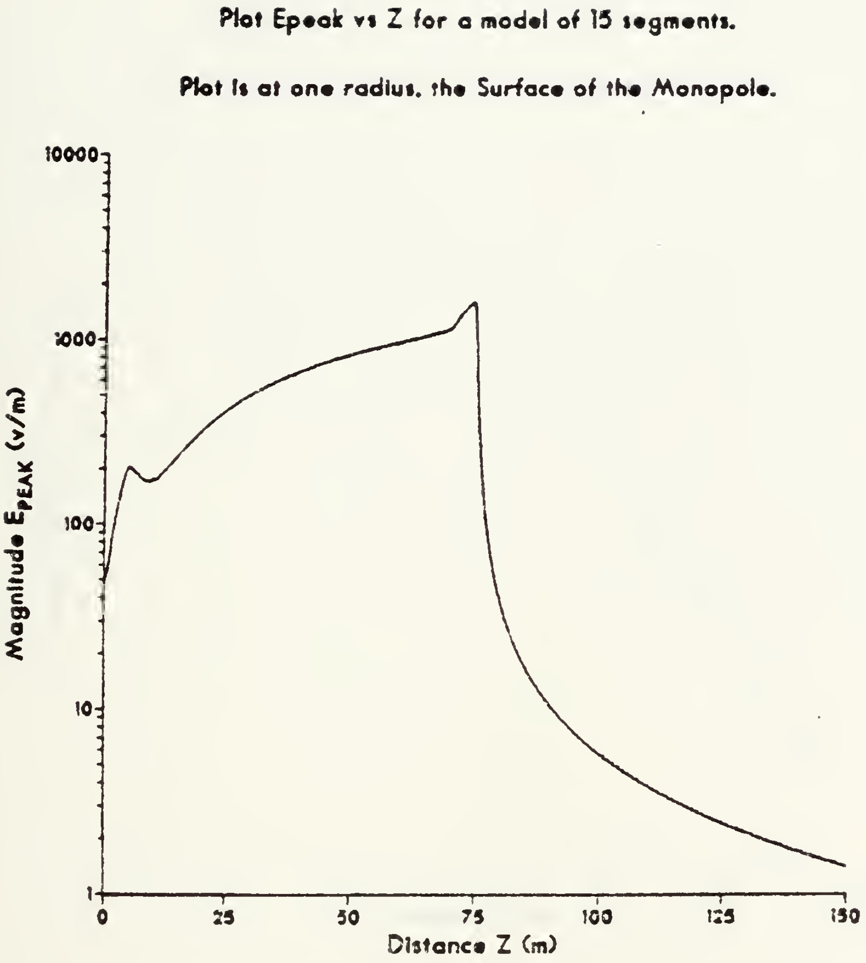

Plot Epeak vs Z for a model of 15 segments.

Plot is at one radius, the Surface of the Monopole.

Figure 8

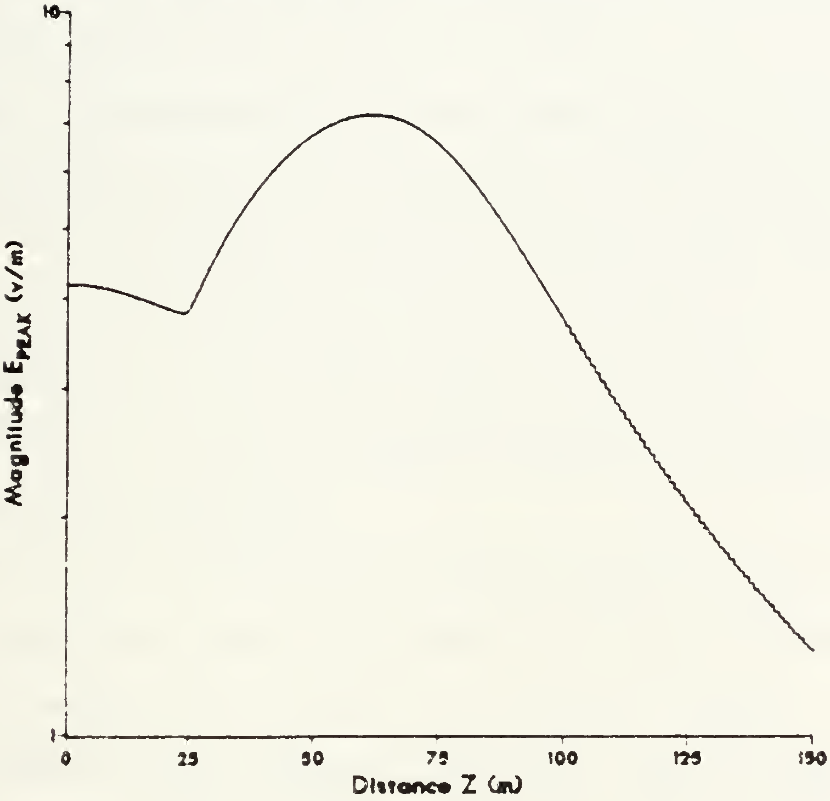

Plot Epeak vs Z for a model of 15 segments.

Plot is at 100 radii, 29.7 Meters above the Surface.

Figure 9

greatest percentage is directed radially outward. A more complete set of E(Z) Plots are found in Figure A-1 through A-18 in Appendix A.

2. E(R) Plots

Figure 10 shows the very large value of E_z found at the top of the antenna decreases rapidly in magnitude as the O.P. moves radially away from the monopole. At a radial distance of approximately $\lambda/2\pi$ the rapid decline in E_z subsides and approximates the attenuation with distance observed at other points along the antenna (see Figure 11). Since $E_z=0$ at the surface, as shown in Figure 11, the magnitude of the field rises rapidly with radial distance to a peak at about 20 meters from the antenna, from which the magnitude slowly declines.

The rate of decline of $E_r(R)$ appears to be uniform for all positions along the antenna, the only difference being the magnitude from which the decline begins. (Figure 12)

Close to the antenna, the E_{peak} curve follows the E_r curve. At some unknown point, $E_z(R)$ has diminished in magnitude less than $E_r(R)$; hence, the E_{peak} curve switches to follow $E_z(R)$ (Figure 13). The point at which this switch occurs falls at a greater radial distance for O.P.'s at greater heights. This is the result of a larger starting magnitude (at greater heights) from which E_r begins its uniform rate of decline. For larger starting magntudes, a

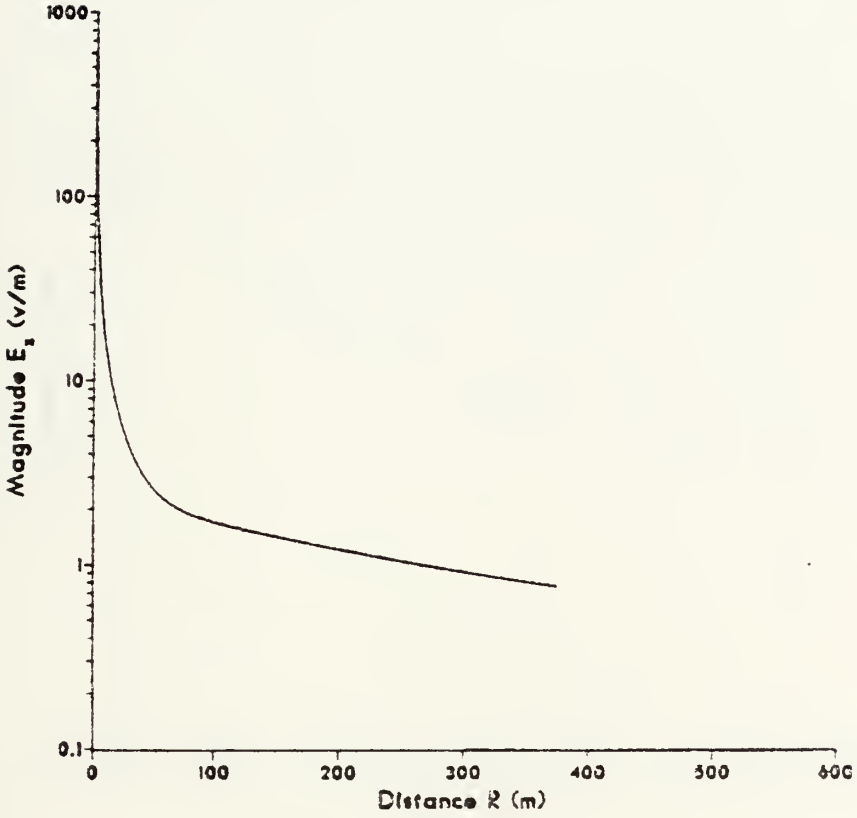

Plot Ez vs r for a model of 15 segments.

Plot is at the height of the monopole along the r axis.

Figure 10

Plot Ez vs r for a model of 15 segments.

Plot is at 1/2 the monopole height along the r axis.

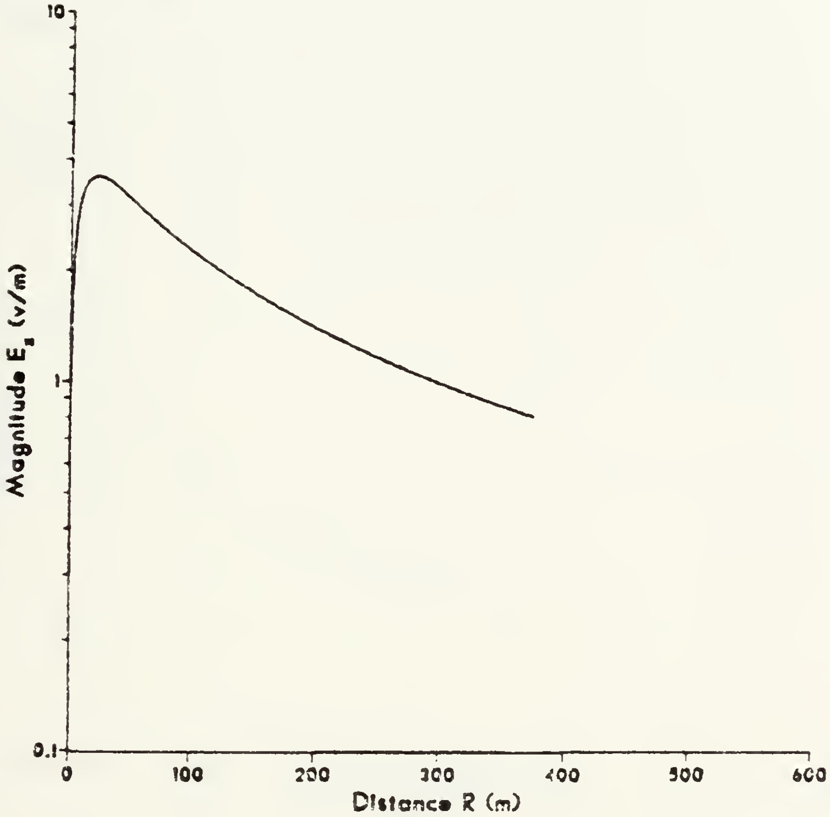

Figure 11

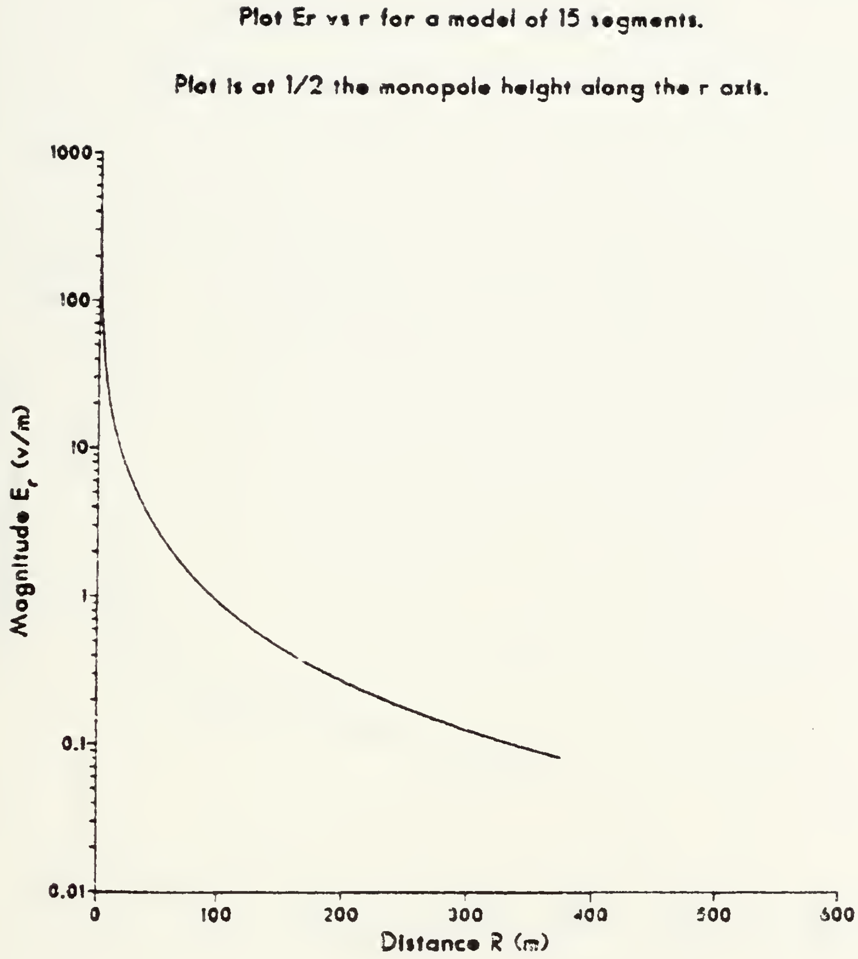

Plot Er vs r for a model of 15 segments.

Plot is at 1/2 the monopole height along the r axis.

Figure 12

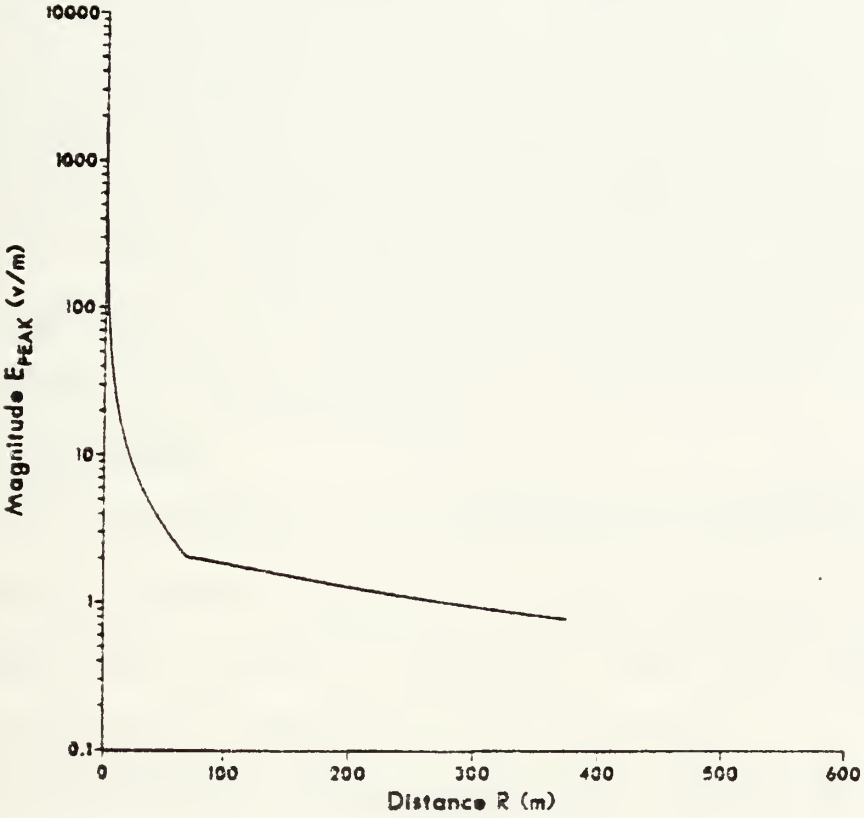

Plot Epeak vs r for a model of 15 segments.

Plot is at the height of the monopole along the r axis.

Figure 13

larger radial distance is allowed for it to decline before the magnitude of E_z exceeds E_r. The point at which this occurs is so sharply defined, that the curve of E_{peak} has an "apparent discontinuity" in it.

At twice the monopole height, the curve of E_{peak} (Figure 14) has an inverted cusp. This results from the same shift in E_z/E_r dominance discussed above. Directly above the antenna, $E_r = 0$; hence, E_z is larger than E_r. But as the O.P. moves radially, E_z declines while E_r rises to a peak. This forms the inverted cusp; then, E_r also begins a decline, but not as rapid as E_z. More plots of E(R) are found in Figures A-19 through A-33 in Appendix A.

3. H(Z) Plots

At the surface of the monopole, the magnitude of H_Φ is virtually constant; there is a slight decrease near the top (Figure 15). Above the monopole, there is a sharp drop (about 80 dB's) in intensity of H_Φ; the field is virtually non-existent there. Similar plots of H_Φ for greater distances from the antenna follow the same type of curve, except, the magnitude of the field parallel to the antenna decreases with increasing distances from the antenna, and the sharp decline in intensity above the height of the antenna becomes less abrupt. At a distance of one wavelength, the difference between the magnitude of H_Φ parallel to the antenna and above its height is about 20 dB. More plots of H(Z) are found in Figure A-34 through A-39 in Appendix A.

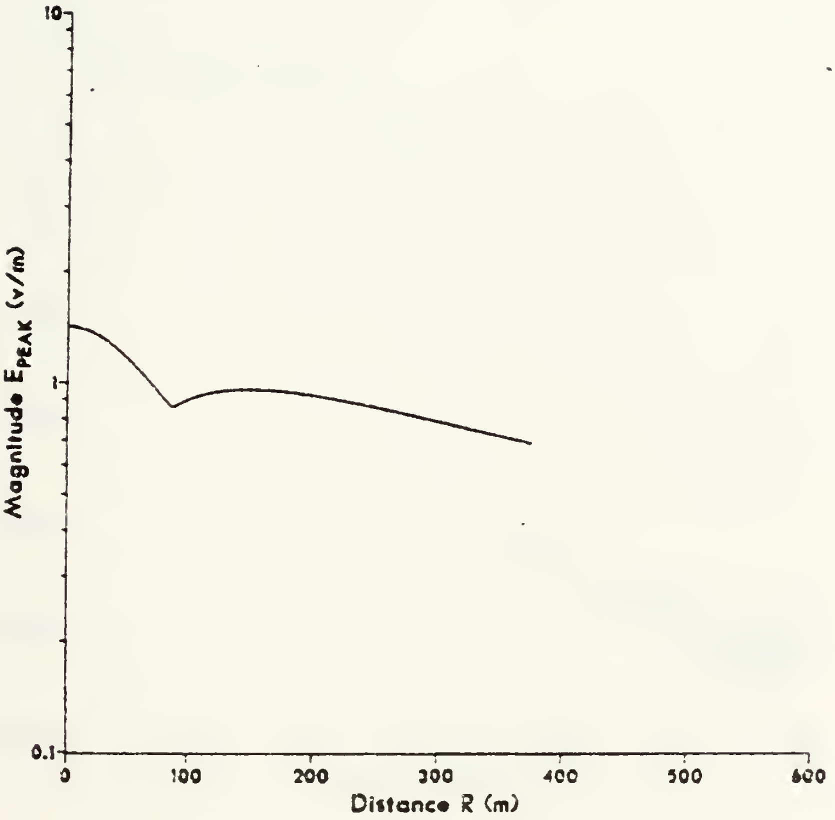

Plot Epeak vs r for a model of 15 segments.

Plot is at twice the monopole height along the r axis.

Figure 14

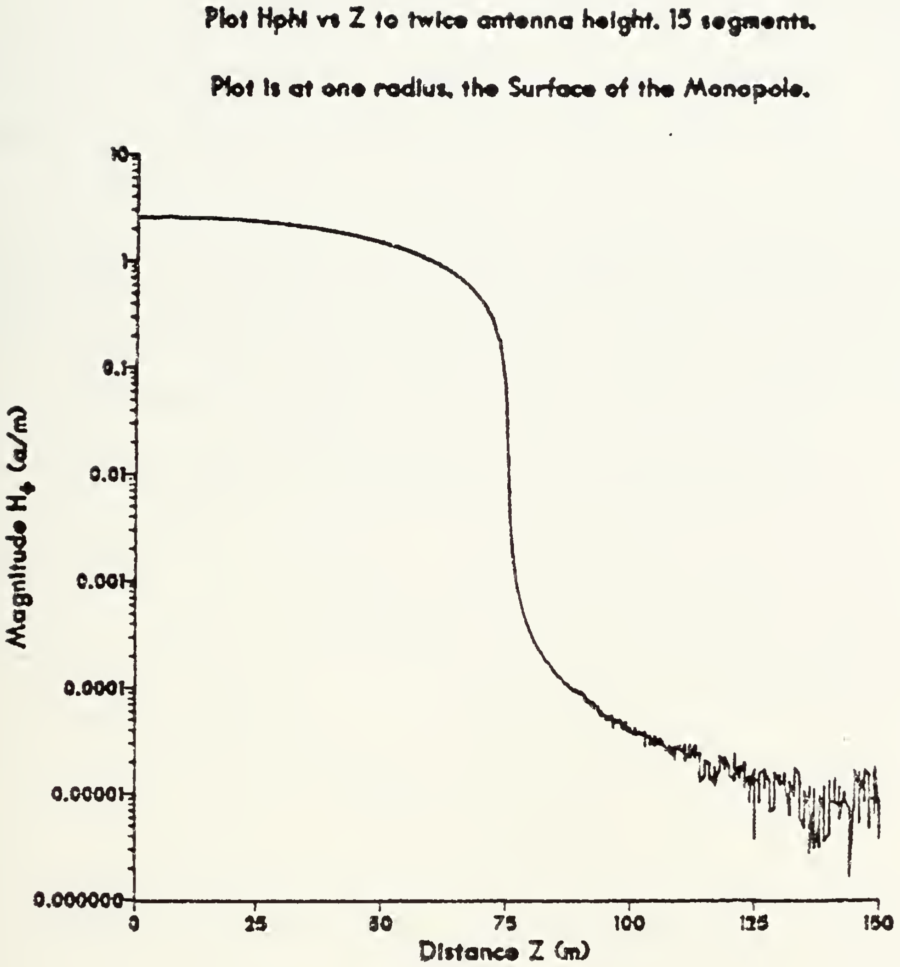

Plot Hphi vs Z to twice antenna height. 15 segments.

Plot is at one radius, the Surface of the Monopole.

Figure 15

4. H(R) Plots

Again, at the surface of the monopole the magnitude of H_ϕ is virtually constant. The magnitude of H_ϕ decreases rapidly with increasing radial distance, and uniformly for various antenna heights. Figure 16 is an example curve which delineates the behavior of H_ϕ all along the axis. As indicated above, for O.P.'s directly above the antenna, H_ϕ is virtually non-existent. As the O.P. moves radially outward, at twice the height of the antenna, H_ϕ rises quickly to a peak, then slowly declines in magnitude. More plots of H(R) are found in Figure A-40 through A-44 in Appendix A.

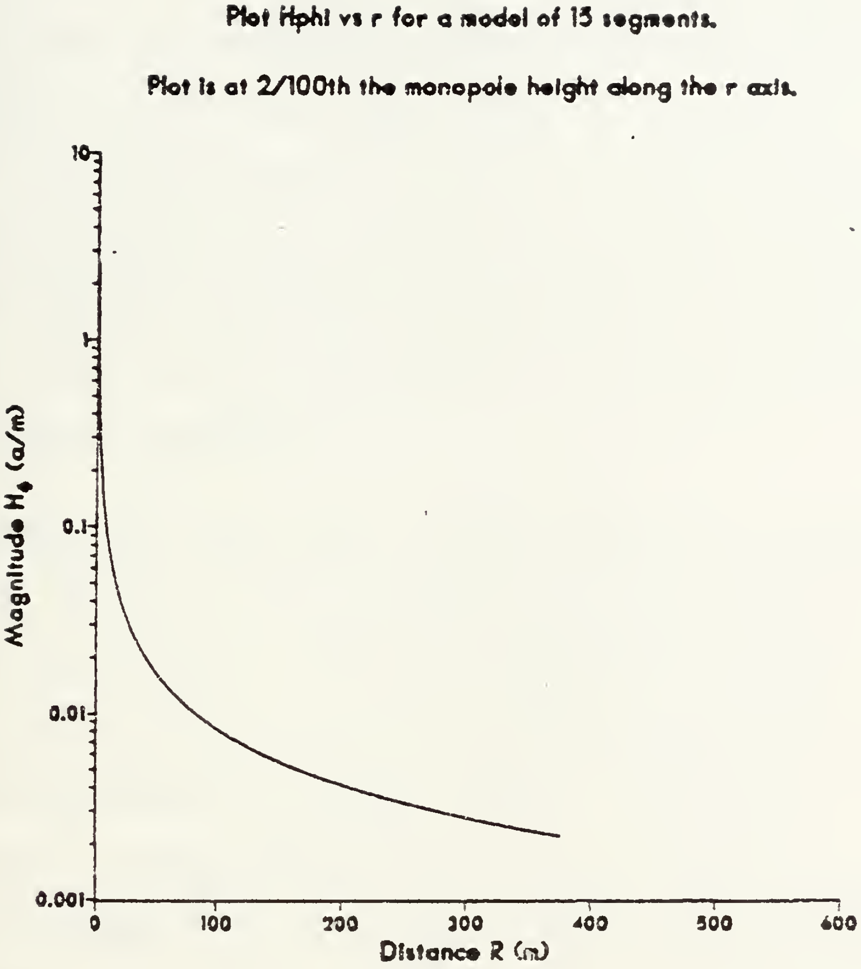

Plot Hphi vs r for a model of 15 segments.

Plot is at 2/100th the monopole height along the r axis.

Figure 16

V. A VALIDATION OF NEC NEAR-FIELD CALCULATIONS

NEC is still evolving. On-going efforts toward refining and improving its calculations are constantly occurring. In its present form, it has been extensively used, and documented to provide accurate results in the far-field; its validity in close to the antenna is not so well documented. To show that NEC provides reasonable results in near-field regions, three tests have been run. They are described in the following paragraphs.

A. COMPARISON OF NEC WITH CLASSICAL ANALYSIS RESULTS

Mills [Ref. 8], using equations similar to those found in Ref. 4 (pp. 333 to 338), calculated theoretical values for E_z as a function of radial distance from the antenna, for short antennas of various lengths. Two of his plots are of interest to this study; they are for dipoles of half-length (h) equal to $.1\lambda$ and $.2\lambda$. The results of his calculations are plotted as broken lines in Figure 17, the plot of NEC's calculations for the same antennas are shown as solid lines. Remembering, the assumption of sinusoidal current is accurate only for the quarter-wavelength monopole*,

---

*As the antenna becomes shorter, the sinusoidal peak occurs further back on the feed line and the distribution on the antenna becomes more linear.

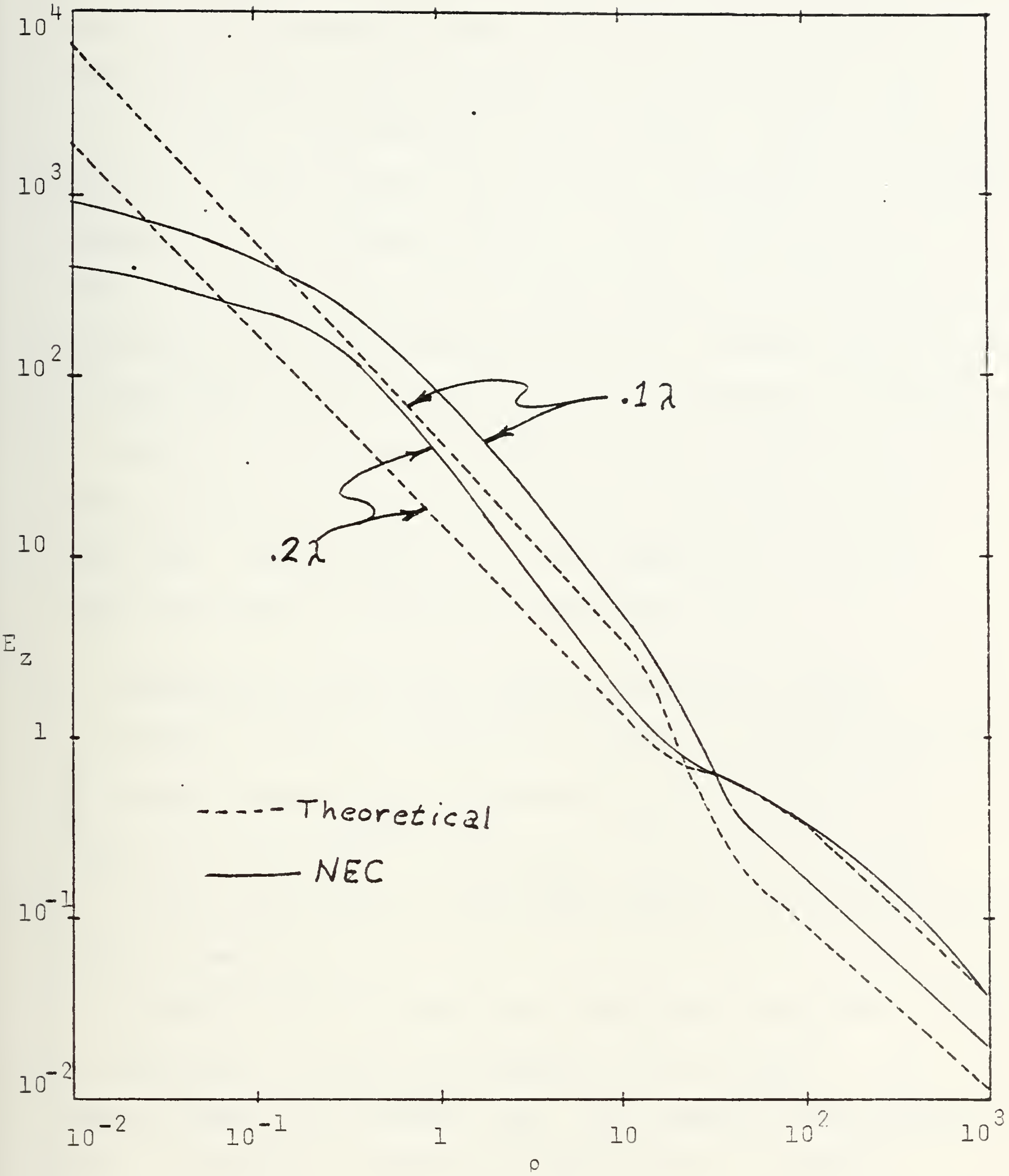
10^4
10^3
10^2
10
E_z
1
10^{-1}
10^{-2}
10^{-2}
10^{-1}
1
10
10^2
10^3
ρ
.1λ
.2λ
----- Theoretical
—— NEC

Figure 17

it is interesting to note NEC's calculations are more closely matched as the antenna length approaches the resonant condition, especially for radial distances greater than $\lambda/2\pi$ (= 300/2 = 48 meters for this study). Balzano [Ref. 7] points out, that inside this distance, the classical approach breaks down, "...because nowhere in the near field ($\rho<\lambda/2\pi$) does the dipole look like an elementary source (infinitesimal dimension) from the observation point". Balzano also points out that the classical approach has a constantly increasing E_z field up to the dipole surface which is incongruent with energy density boundary conditions at the antenna edge. Therefore, the leveling off of the magnitude of E_z, as predicted by NEC, is the more reasonable plot.

B. COMPARISON OF NEC WITH EMPIRICAL ANALYSIS RESULTS

Balzano in Ref. 7 (Part II) performed some measurements on a dipole constructed from bronze rods of .0015 meters diameter (= $3.75 \times 10^{-3}\lambda$) that was .188 meters in length (= $.4712\lambda$), including a .0018 meter gap at the center from which it was fed.

A model of this antenna was constructed using NEC. The configuration chosen was a monopole of 19 segments, each segment being .0049 meters long. The monopole was mounted above a perfectly conducting ground plane in a manner similar to that used for this study. Plots of E_z and E_r were run as a function of Z for radial distances of .003, .006,

.01, .02, .03, .04, .05, and .06 meters from the dipole axis. The results of these plots are shown in Appendix B. With the exception of a scaling factor, the information contained in these plots is the same as that discussed in Section IV.C. for the study. To further compare the results of NEC with the measured values, the measured peaks of the square of the electric field intensity, for both axial and radial polarizations, at the radial distances indicated above, were extracted from plots in Ref. 7. These values were plotted in Figures 18 and 19 along with the square of the peak of the fields extracted from the plots of the model run by NEC. As can be seen, very close correlation between the model and the measurements were obtained. The largest discrepancy was at .003 meters distance where the calculated value was inordinately higher than the measured value, relative to other calculated/measured pairs. Balzano's calculated value was also quite a bit higher, which would indicate the measured value was a bit low. Credence for this argument is supported by Balzano's statement, "...at closer distances, capacitive effects became predominant".

C. COMPARISON OF NEC WITH MAXWELL'S EQUATIONS

Chang [Ref. 6] points out that "...on the surface of the monopole the field component H_Φ should be proportional to the current distribution I(Z)...". The NEC calculated value of H_Φ was compared to the current flowing on the model. The

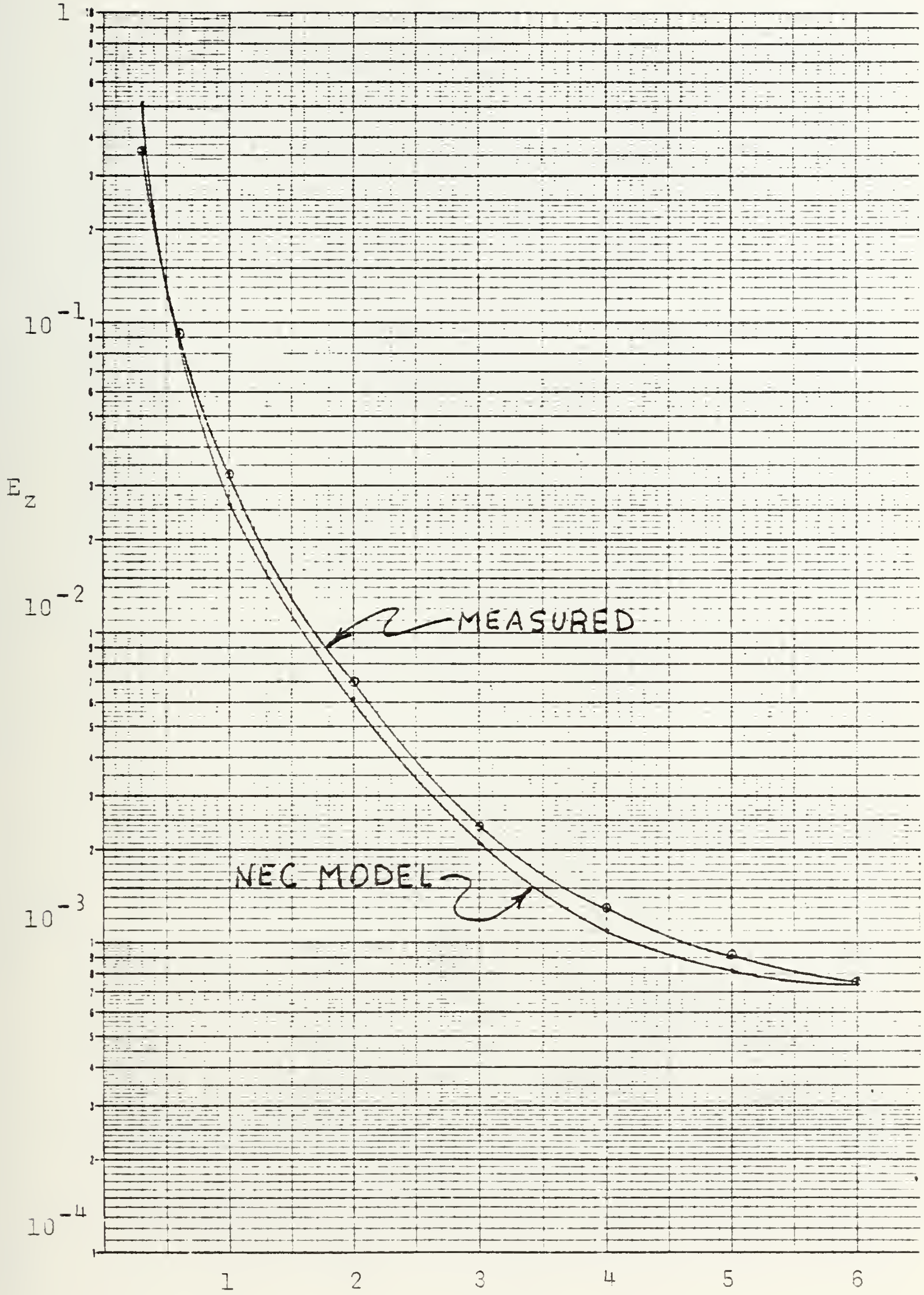

Figure 18

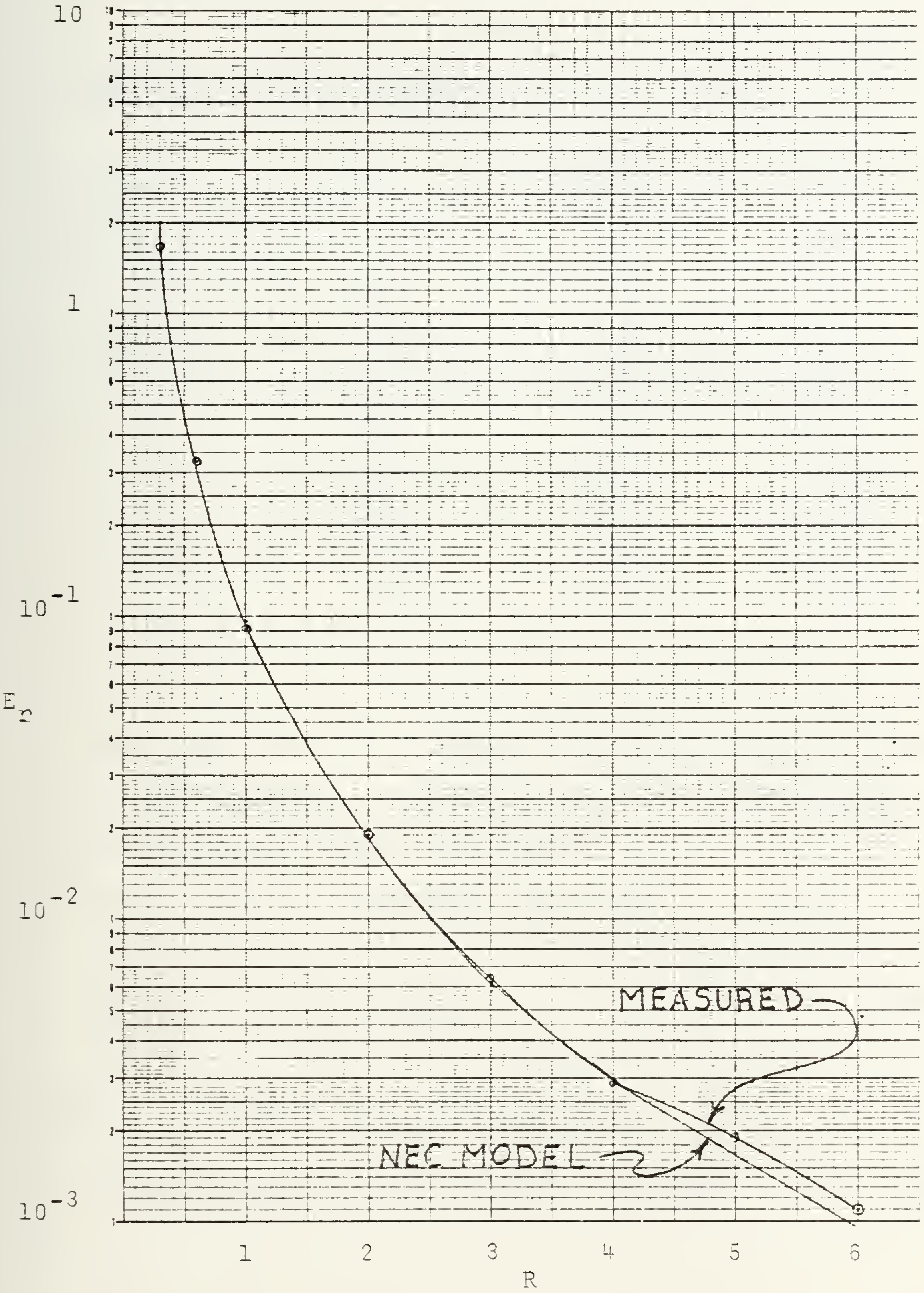

Figure 19

results are shown in Table I.

TABLE I

COMPARISON OF NEC COMPUTED H-FIELD AND CURRENT AT THE MONOPOLE SURFACE

Z	H_Φ	$2\pi r H_\phi$	I(Z)
2.49	2.573	4.850	4.849
7.50	2.577	4.858	4.858
12.51	2.552	4.810	4.811
17.52	2.497	4.707	4.707
22.50	2.413	4.548	4.548
27.51	2.300	4.335	4.337
32.52	2.161	4.073	4.076
37.53	1.997	3.764	3.767
42.54	1.810	3.412	3.414
47.52	1.601	3.018	3.019
52.53	1.369	2.581	2.584
57.54	1.118	2.107	2.112
62.55	.8478	1.598	1.604
67.56	.5562	1.048	1.056
72.54	.2247	.4235	.4304

Quite good agreement is maintained all along the antenna. The largest variation occurs at the end of the antenna and that variation is still less than 1%.

Chang uses the difference between:

$$E\rho(\rho,z) = j\,\frac{\zeta_o}{\beta}\,\frac{\partial}{\partial z}\,H_\phi(\rho,z) \tag{63}$$

and

$$\frac{1}{\rho}\,\frac{\partial}{\partial \rho}\,(\rho E\rho(\rho,z)) = -\,\frac{\partial}{\partial z}\,E_z(\rho,z) \quad \text{for } \rho \neq a \tag{64}$$

to approximate E_ρ. This relationship is:

$$E_\rho(\rho, z_2) = j\,\frac{\zeta_o}{\beta h}\left(\frac{h}{z_3 - z_1}\right)\left(H_\Phi(z_3) - H_\Phi(z_1)\right) \qquad (65)$$

Its application to the data from the study at sample points yields Table II.

TABLE II

COMPARISON OF E_ρ ESTIMATED AND E_ρ CALCULATED BY NEC

z_2	$H_\Phi(Z_3)-H_\Phi(Z_1)$	E_ρ Est.	E_ρ Calc.
2.5	0.	0	105
7.5	0.	0	177
12.5	.001	90	195
17.5	.003	270	274
22.5	.004	360	366
27.5	.005	450	458
32.5	.006	540	548
37.5	.007	630	634
42.5	.007	630	716
47.5	.009	810	794
52.5	.010	900	866
57.5	.010	900	935
62.5	.0112	1008	1006
67.5	.0121	1089	1090
72.5	.0156	1404	1402

The correlation between the estimated value and the calculated value is quite good above approximately 15 meters in height on the monopole. The wide variation below that point can be attributed to insufficient significant figures in the values of H_Φ used to estimate the difference. Also, NEC was computing the field emitted from the base of the monopole,

which is not considered in the estimate of Maxwell's equations. Considering these two factors, the correlation is surprisingly good.

E_z is expected, by Maxwell's equations, to be zero on the surface of the monopole. In NEC, this condition is only enforced at the match points. The best estimate of how well NEC approximates $E_z=0$ can be seen from the plot of $E_z(Z)$ at the surface of the monopole, Figure 20. The magnitude of E_z that is radiated can be found at the top of the monopole, as expected. This value, from Figure 20, is nominally 1000 v/m; at other points along the antenna, the nominal value can be approximated as 1 v/m. This drop of three orders of magnitude, or 60 dB, is a reasonable approximation of zero by virtually any engineering standard.

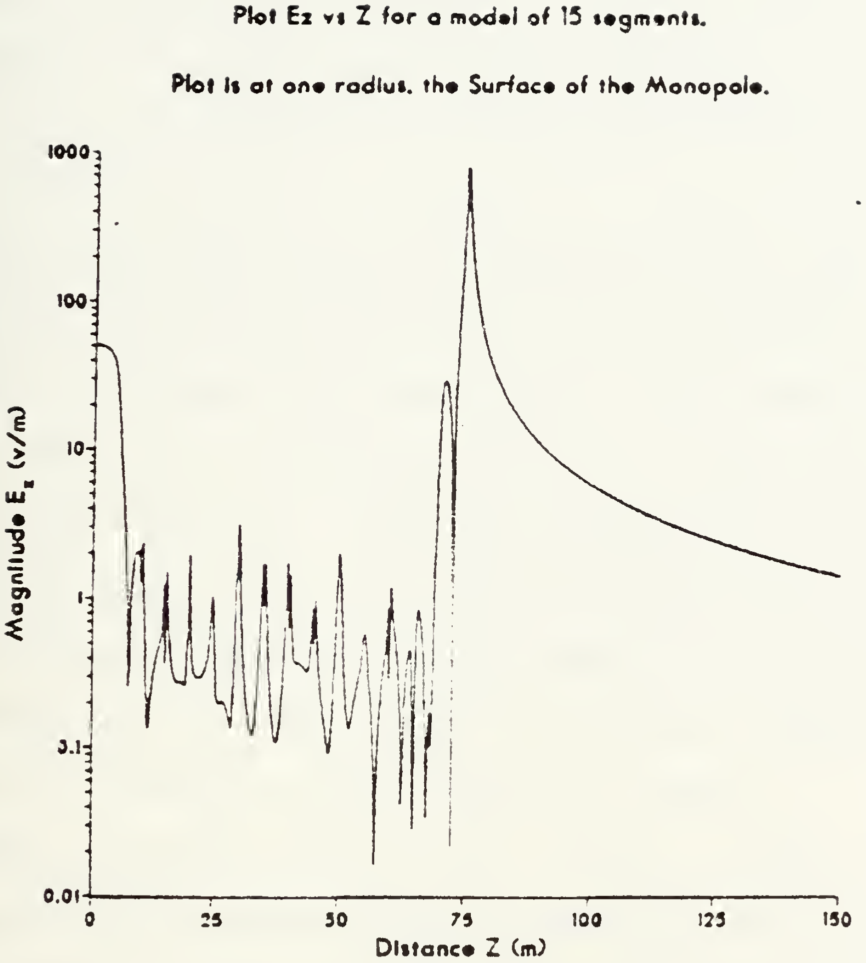

Plot Ez vs Z for a model of 15 segments.

Plot is at one radius, the Surface of the Monopole.

Figure 20

VI. CONCLUSIONS AND RECOMMENDATIONS

From the results of Section V, it can be seen that NEC is an effective analysis tool for near-field calculations and can be used and trusted to give meaningful results. The tool cannot be applied thoughtlessly; care must be exercised to ensure the model accurately represents the actual physical structure. Zoning considerations must be factored into the procedure to ensure that sufficiently small segments are used to get the desired resolution, but not so many as to be wasteful of resources. Electrical parameters must be considered to ensure they represent the operational environment into which the structure will be immersed. When these items are adequately considered, NEC will provide the desired results in a timely and cost effective manner.

Areas of further study could include expanded investigations into the maximum segment length for near-field calculations, investigation of the characteristics of the field emitted from the base insulator region, and effects on the near-field of using multiple parallel wires with cross connections in the manner in which broadcast towers are actually constructed.

APPENDIX A

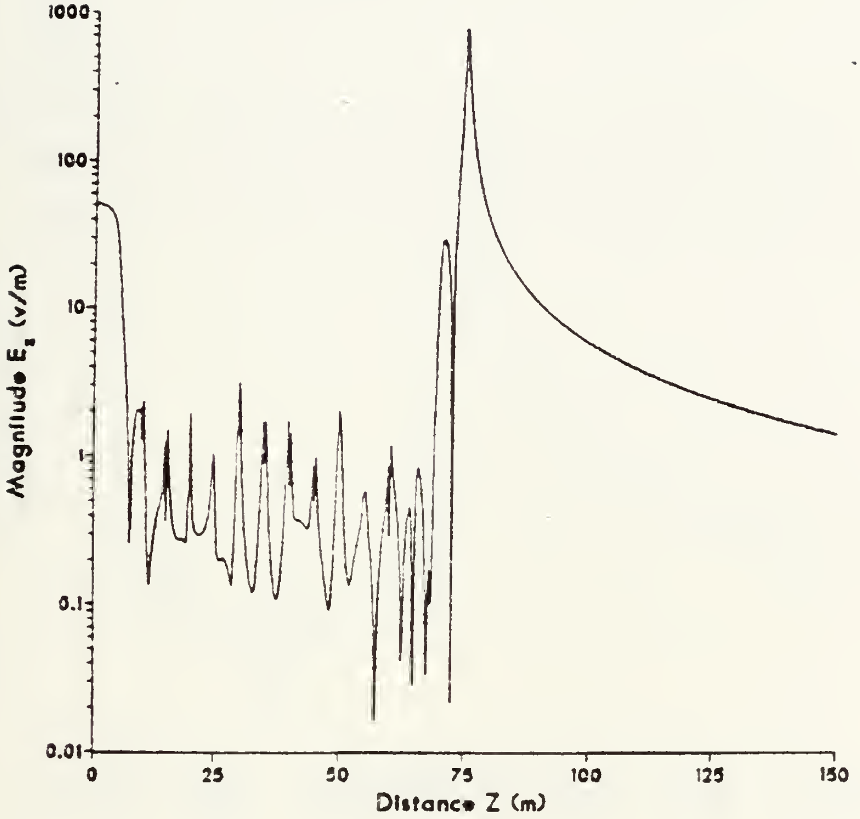

Plot Ez vs Z for a model of 15 segments.

Plot is at one radius. the Surface of the Monopole.

Figure A-1

Figures A-1 through A-6 are plots of E_z as a function of z for various distances from the Z(axis).

Plot Ez vs Z for a model of 15 segments.

Plot is at two radii. .3 Meters above the Surface.

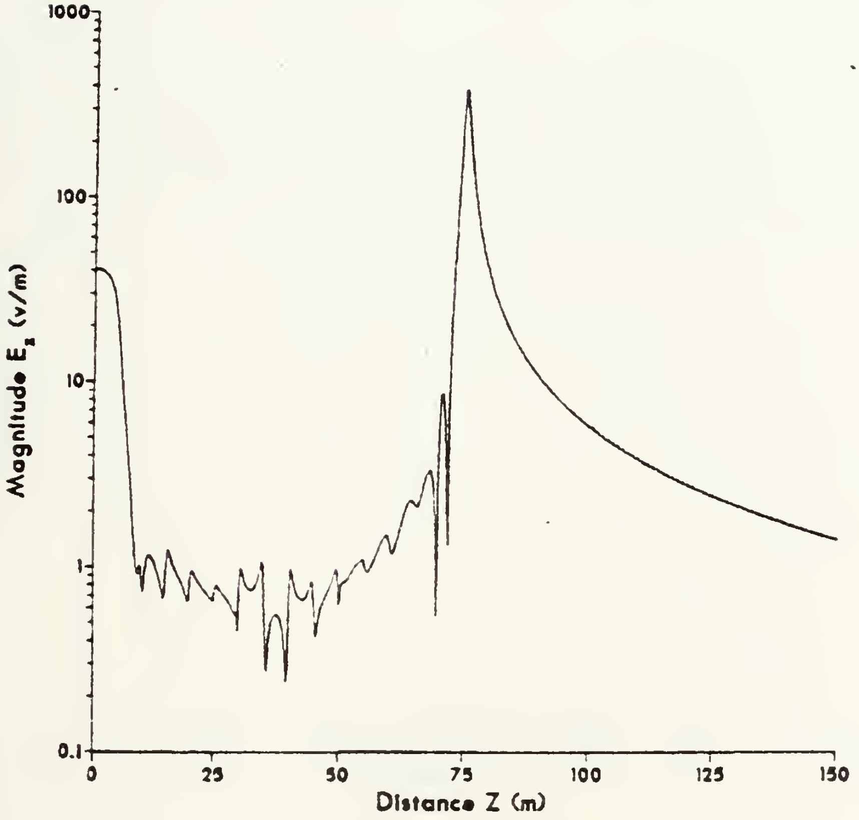

Figure A-2

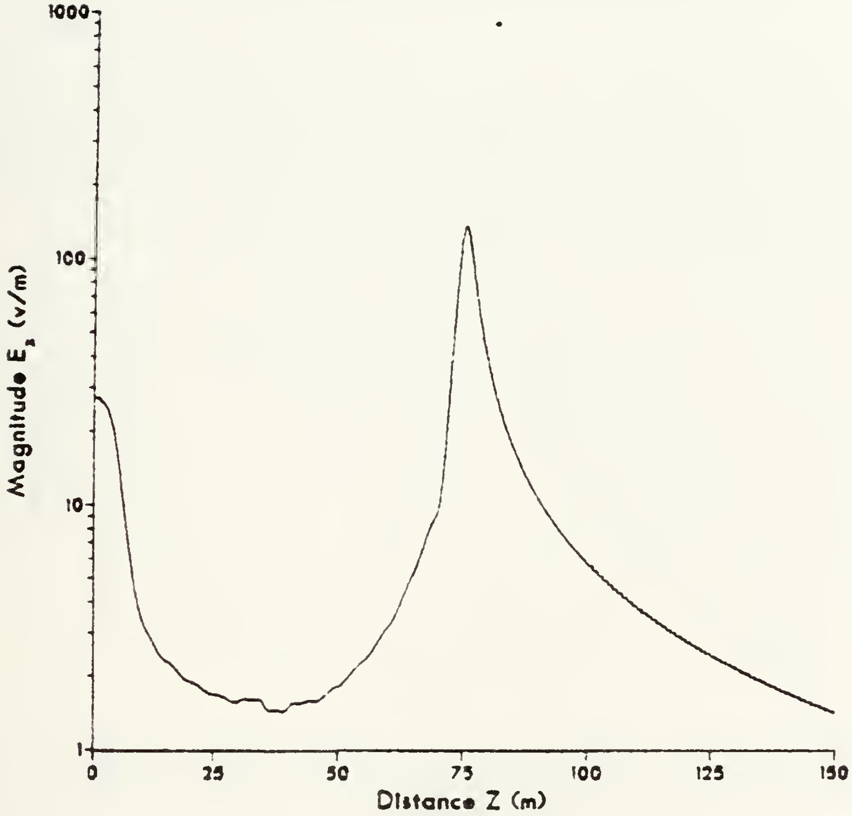

Plot Ez vs Z for a model of 15 segments.

Plot is at five radii, 1.2 Meters above the Surface.

Figure A-3

Plot Ez vs Z for a model of 15 segments.

Plot is at ten radii, 2.7 Meters above the Surface.

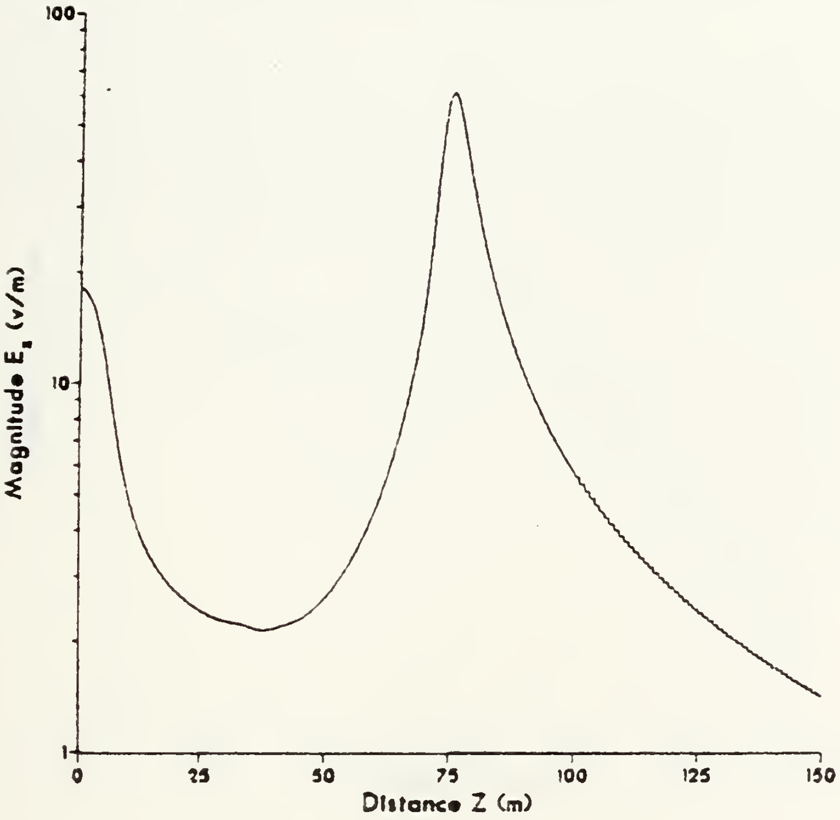

Figure A-4

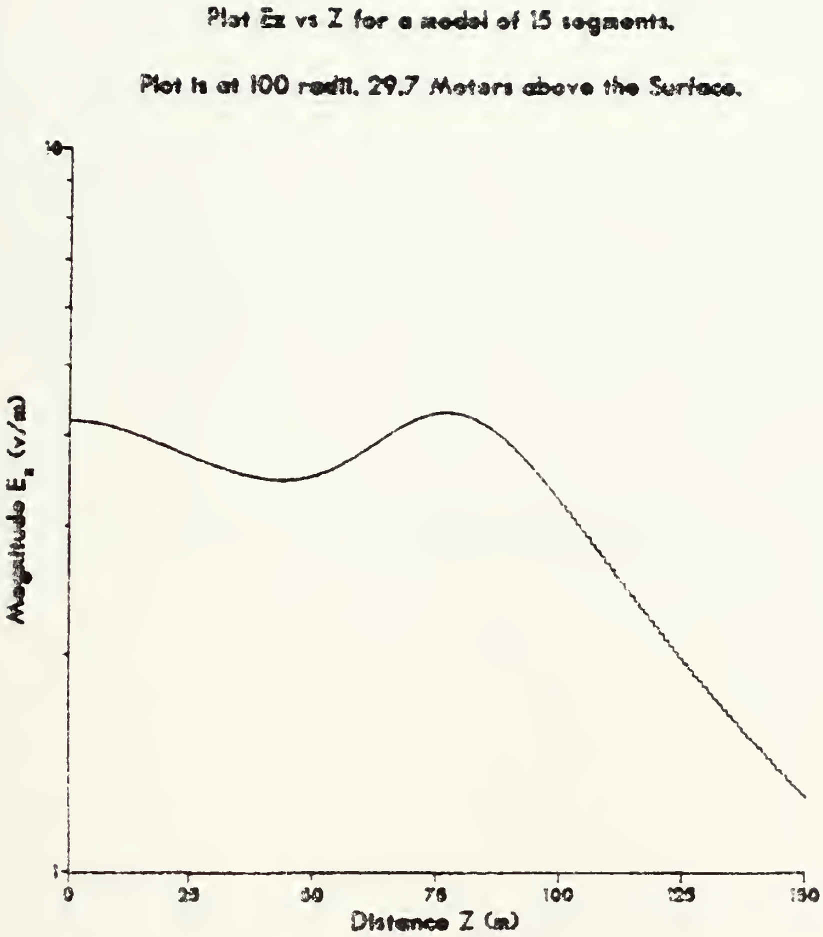

Plot Ez vs Z for a model of 15 segments.

Plot is at 100 radii, 29.7 Meters above the Surface.

Figure A-5

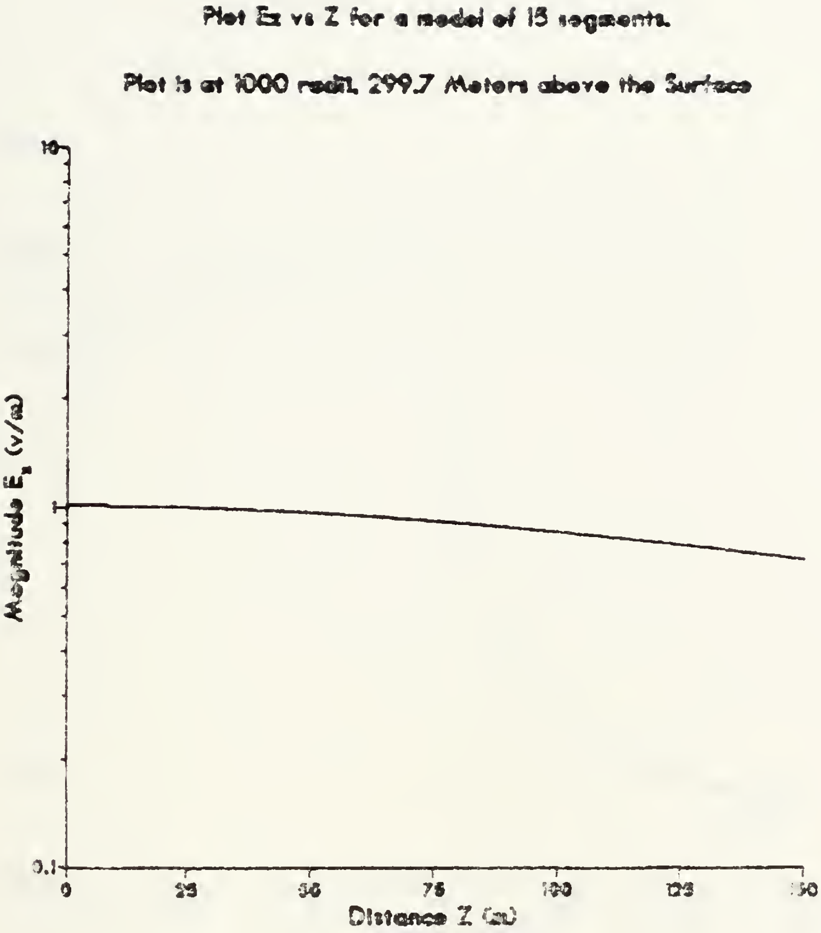

Plot Ez vs Z for a model of 15 segments.

Plot is at 1000 radii, 299.7 Meters above the Surface

Figure A-6

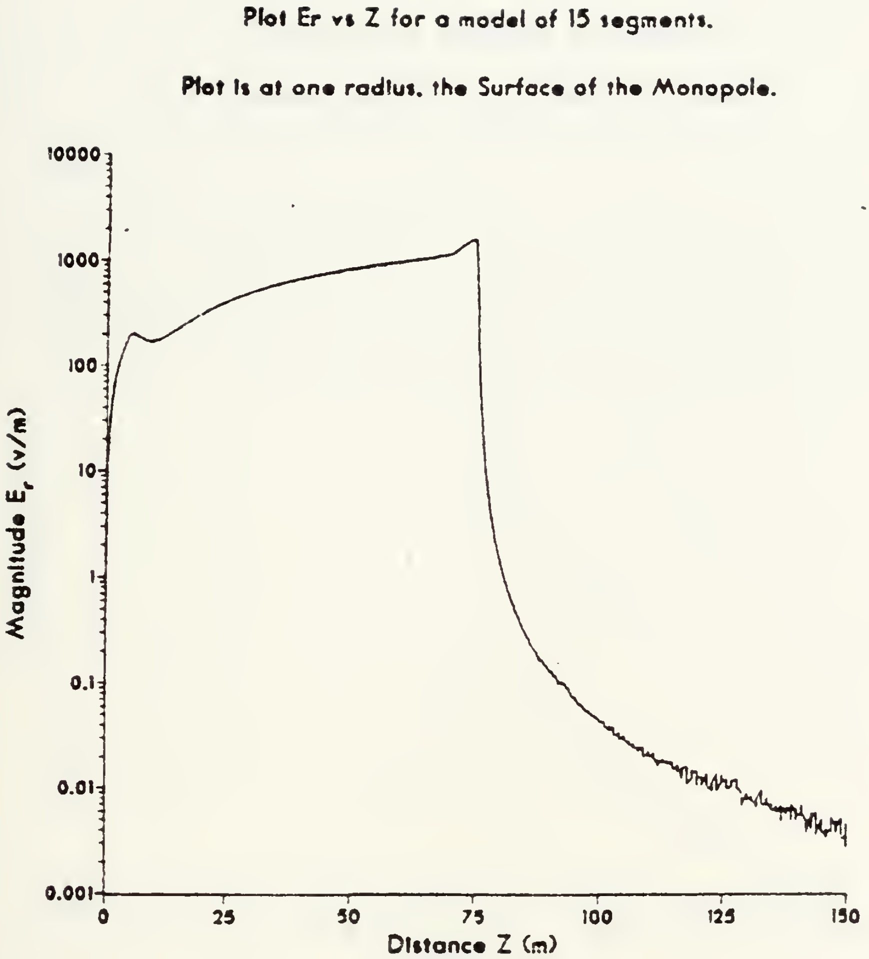

Plot Er vs Z for a model of 15 segments.

Plot is at one radius, the Surface of the Monopole.

Figure A-7

Figures A-7 through A-12 are plots of E_R as a function of z for various distances from the Z-axis.

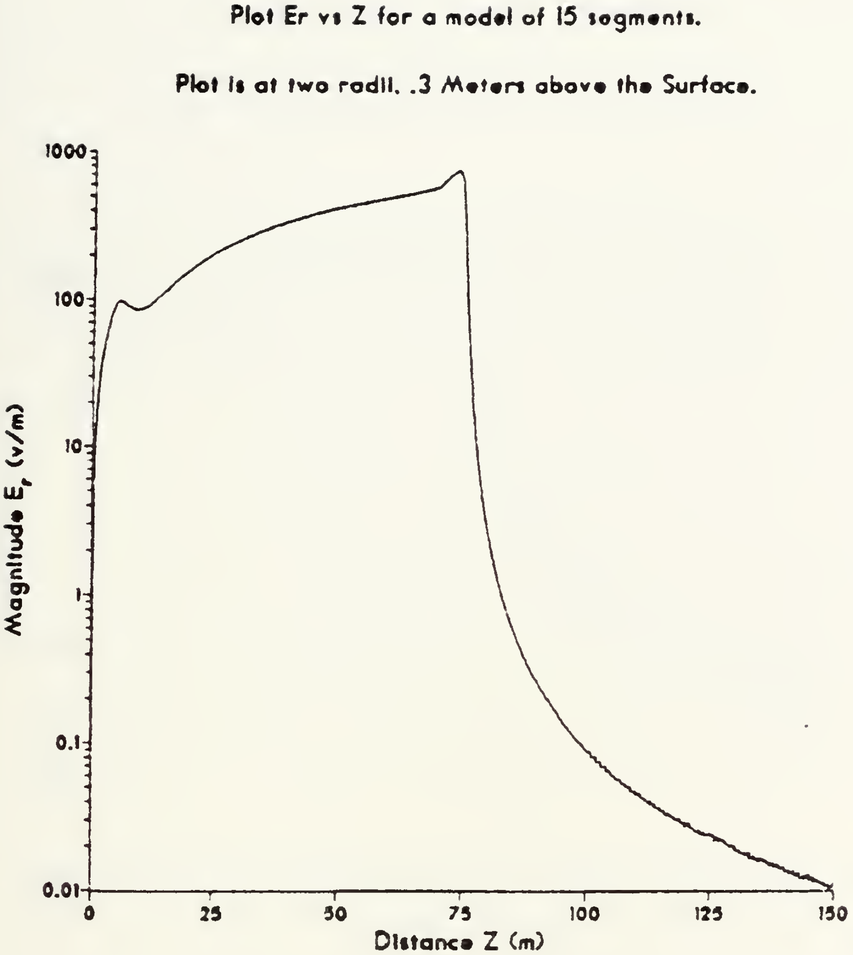
Plot Er vs Z for a model of 15 segments.
Plot is at two radii. .3 Meters above the Surface.
1000
100
10
1
0.1
0.01
Magnitude E_r (v/m)
0
25
50
75
100
125
150
Distance Z (m)

Figure A-8

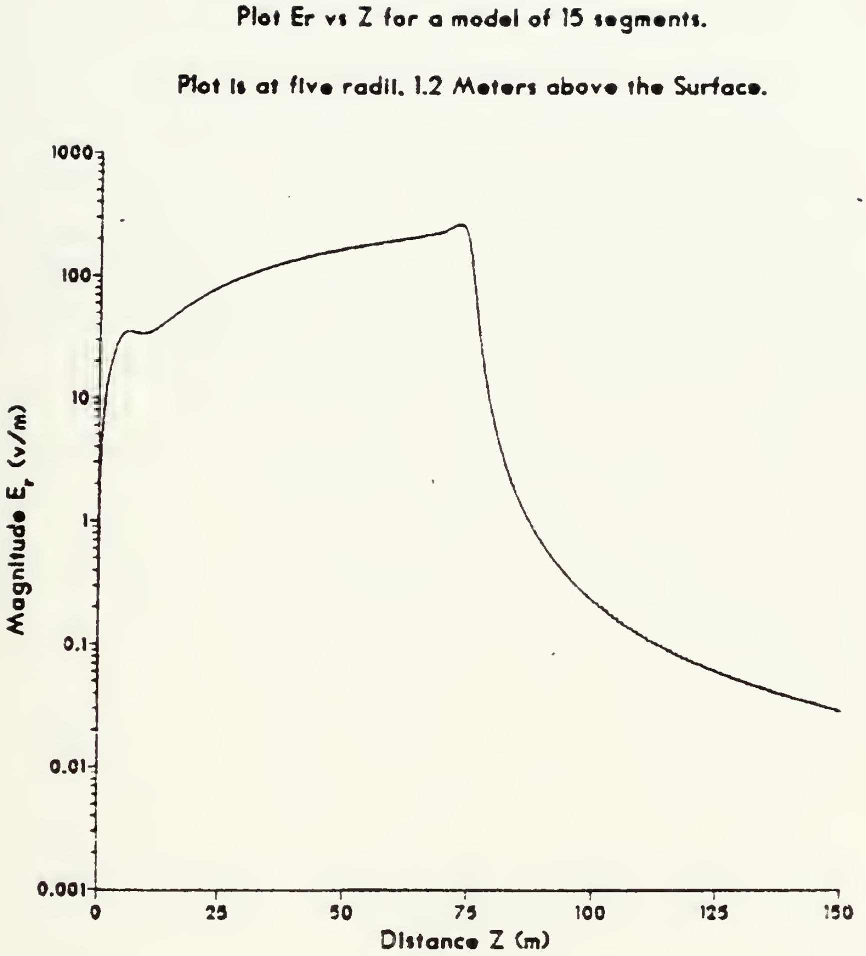

Plot Er vs Z for a model of 15 segments.

Plot is at five radii. 1.2 Meters above the Surface.

Figure A-9

Plot Er vs Z for a model of 15 segments.

Plot is at ten radii. 2.7 Meters above the Surface.

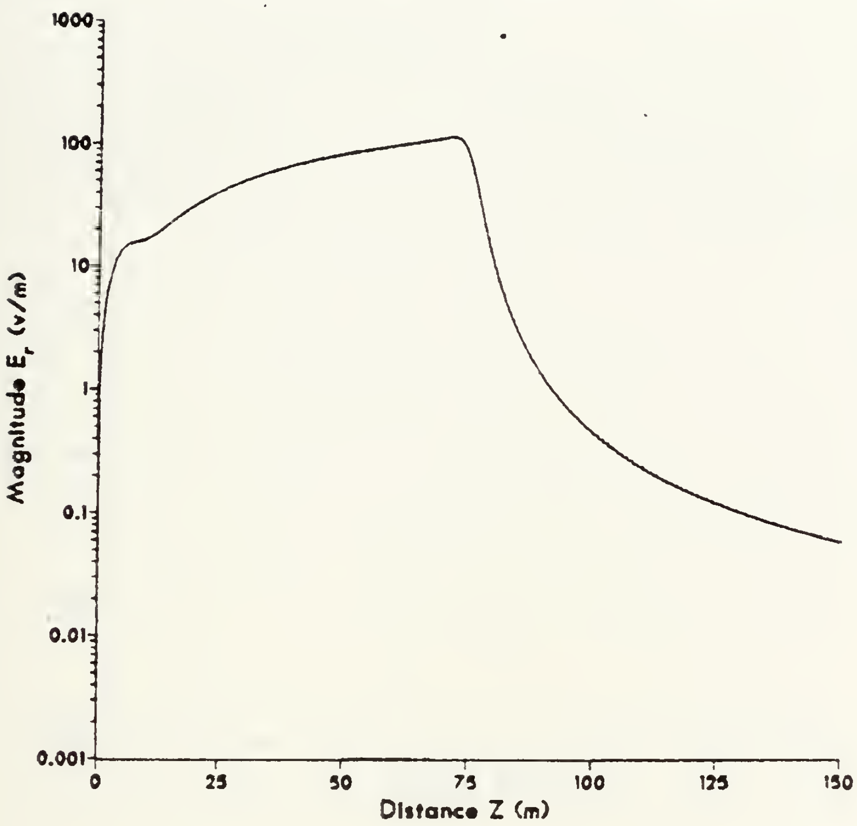

Figure A-10

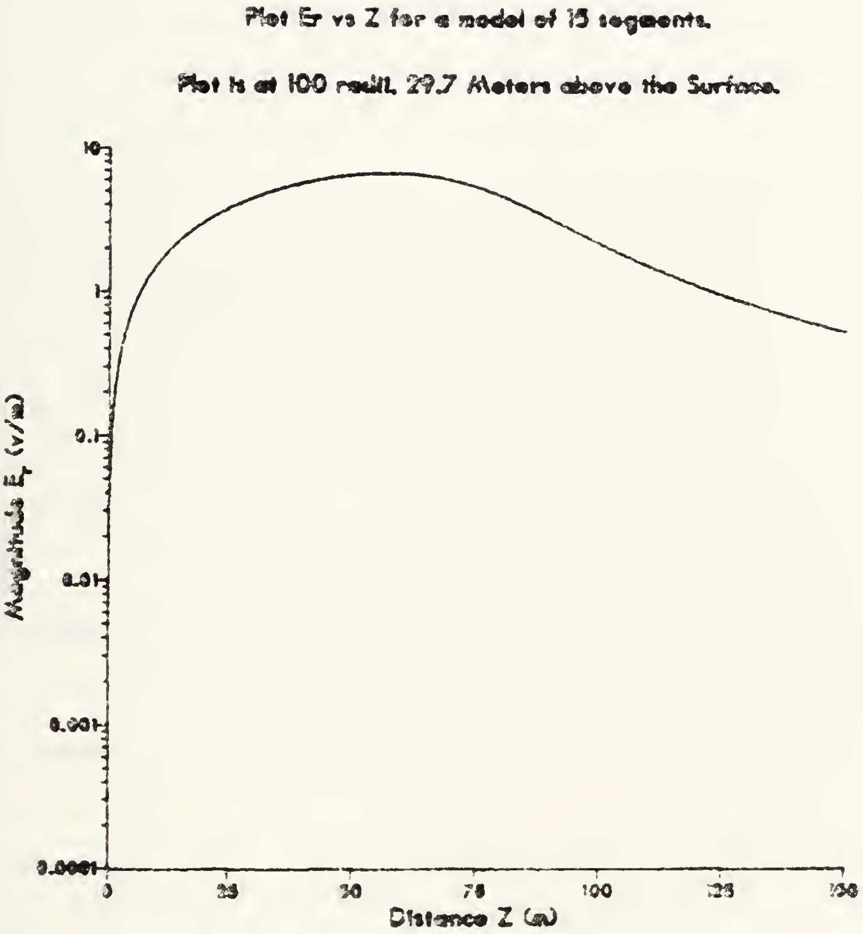Plot Er vs Z for a model of 15 segments.
Plot is at 100 radii, 29.7 Meters above the Surface.
Magnitude E_r (v/m)
10
1
0.1
0.01
0.001
0.0001
0
25
50
75
100
125
150
Distance Z (m)

Figure A-11

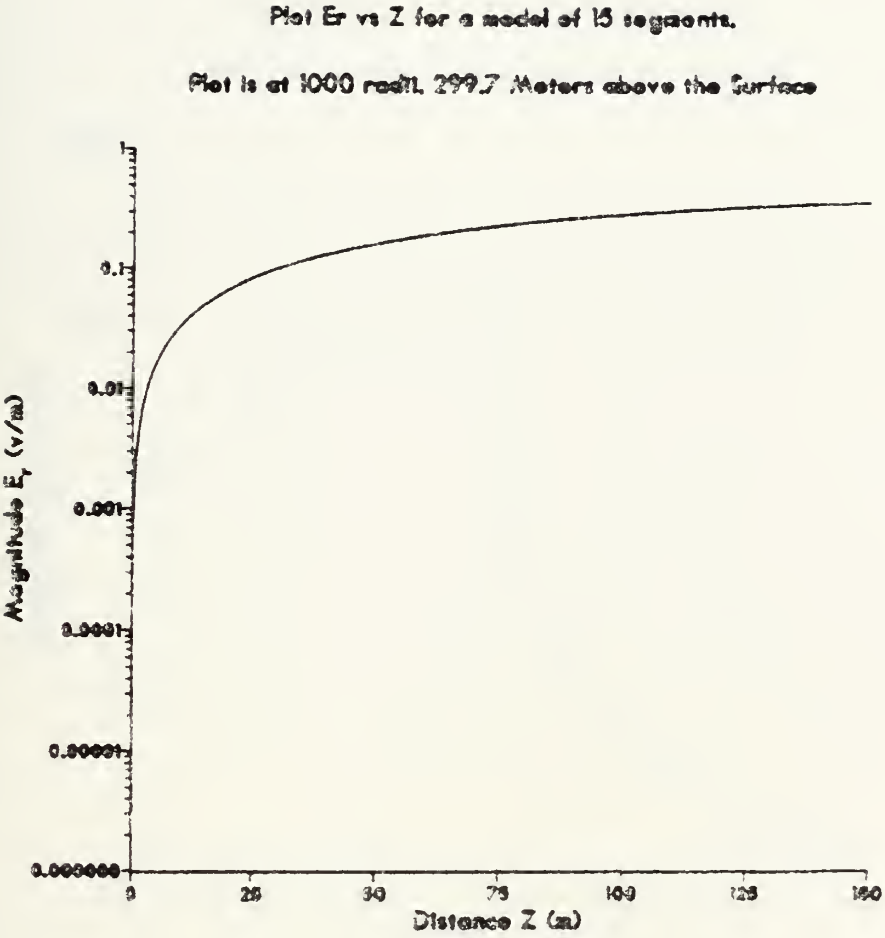
Plot Er vs Z for a model of 15 segments.
Plot is at 1000 radii, 299.7 Meters above the Surface
1
0.1
0.01
0.001
0.0001
0.00001
0.000000
Magnitude E_r (v/m)
0
25
50
75
100
125
150
Distance Z (m)

Figure A-12

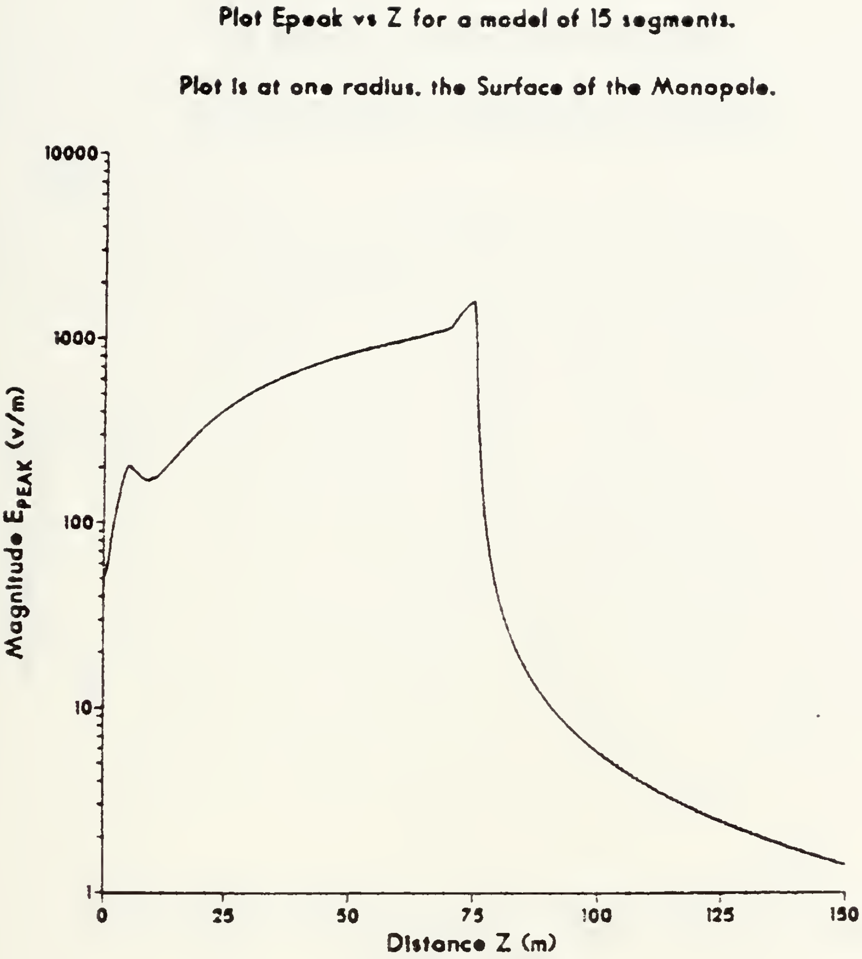
Plot Epeak vs Z for a model of 15 segments.

Plot Is at one radius. the Surface of the Monopole.

Figure A-13

Figures A-13 through A-18 are plots of E_{peak} as a function of z for various distances from the Z-axis.

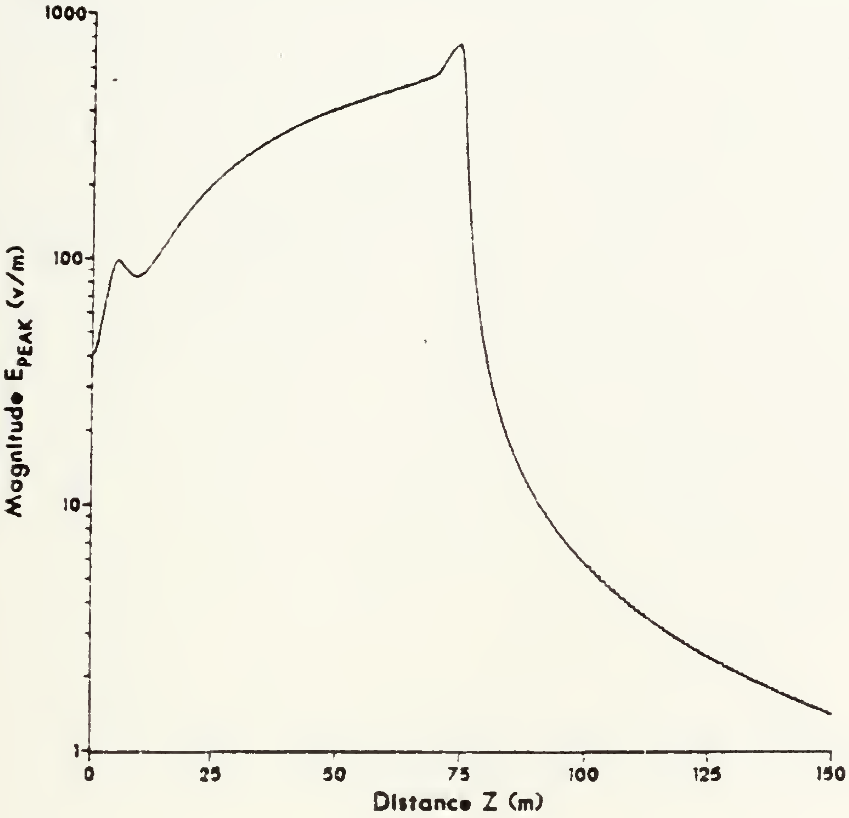

Plot Epeak vs Z for a model of 15 segments.

Plot is at two radii. .3 Meters above the Surface.

Figure A-14

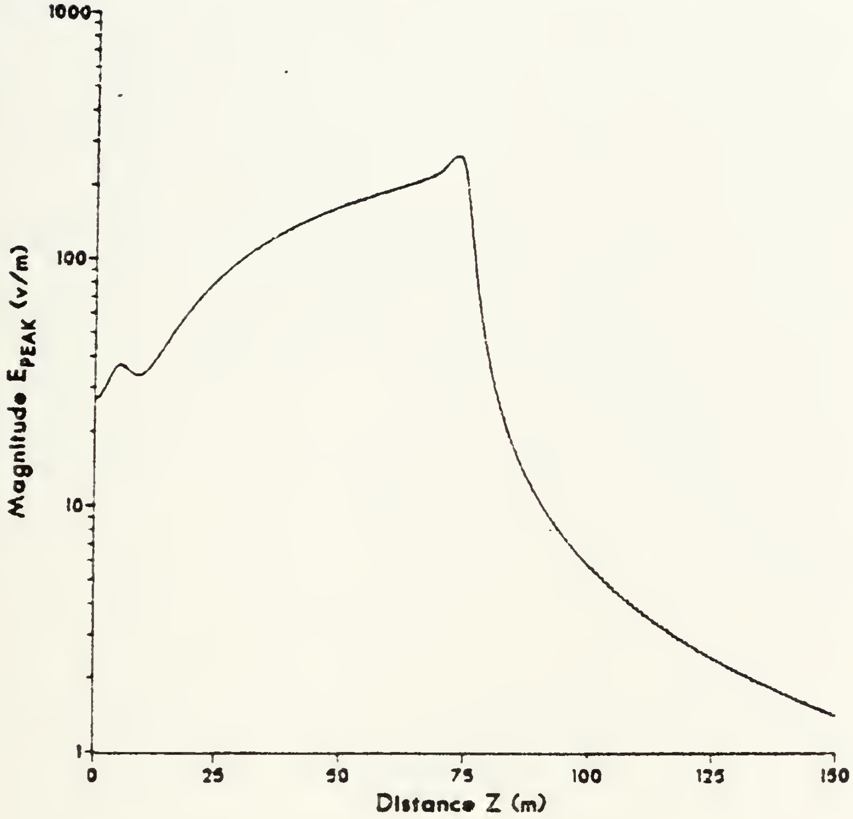

Plot Epeak vs Z for a model of 15 segments.

Plot is at five radii, 1.2 Meters above the Surface.

Figure A-15

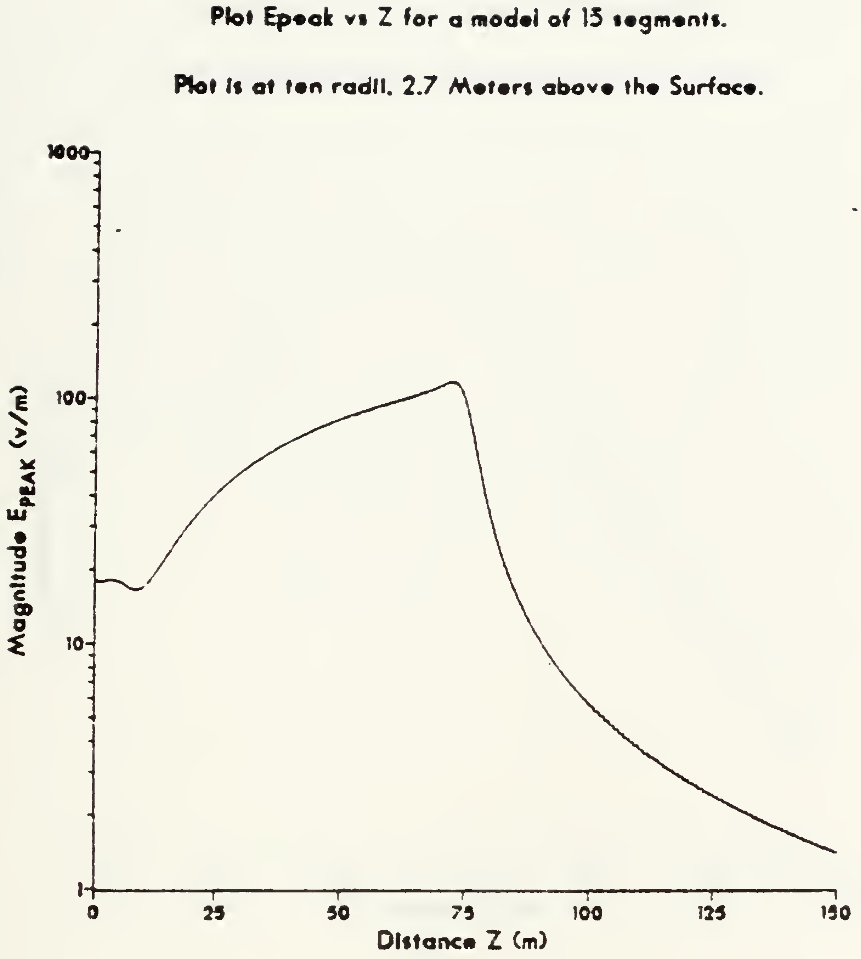

Plot Epeak vs Z for a model of 15 segments.

Plot is at ten radii, 2.7 Meters above the Surface.

Figure A-16

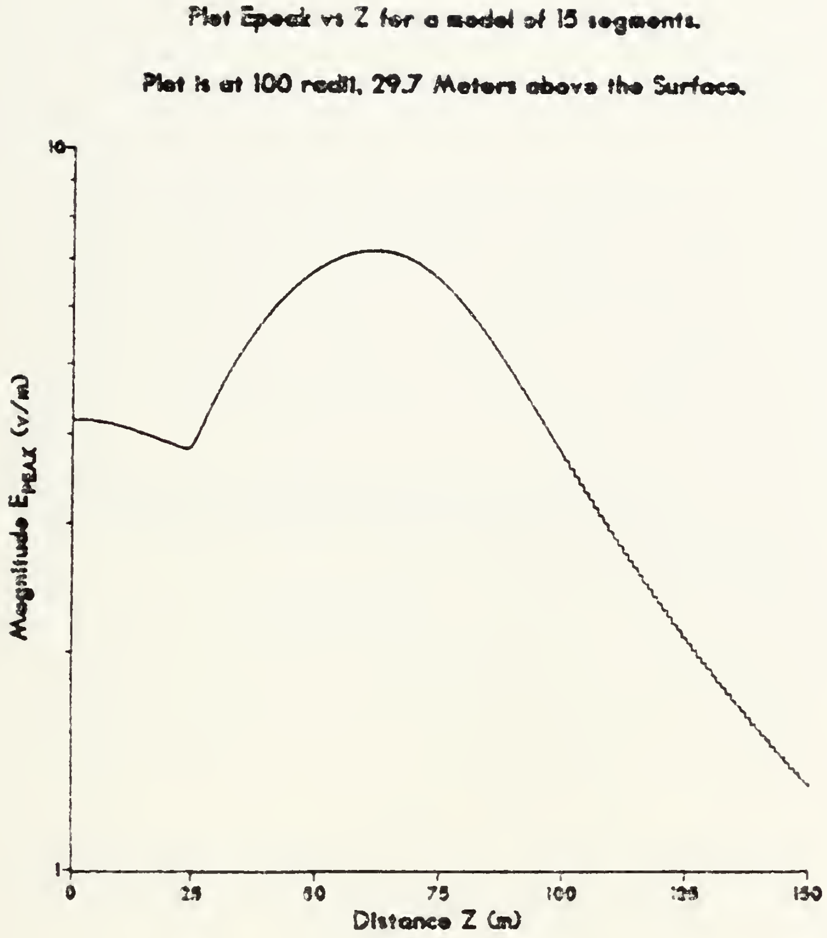

Plot Epeak vs Z for a model of 15 segments.

Plot is at 100 radii, 29.7 Meters above the Surface.

Figure A-17

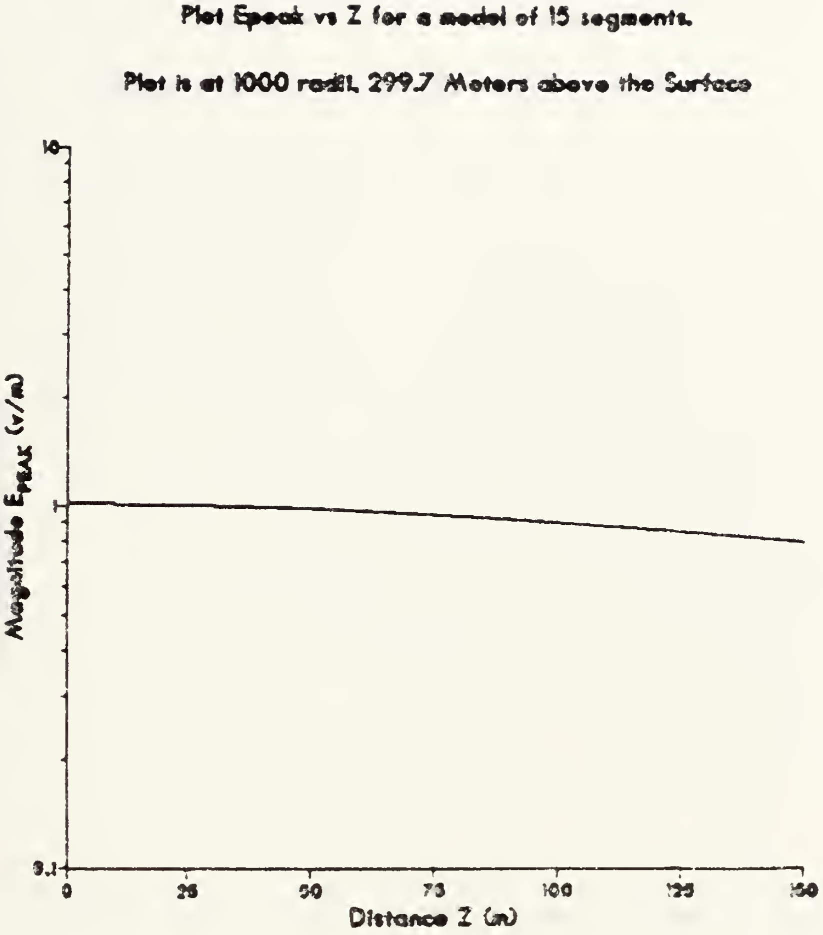
Plot Epeak vs Z for a model of 15 segments.
Plot is at 1000 radii, 299.7 Meters above the Surface
10
1
0.1
Magnitude E_{PEAK} (v/m)
0
25
50
75
100
125
150
Distance Z (m)

Figure A-18

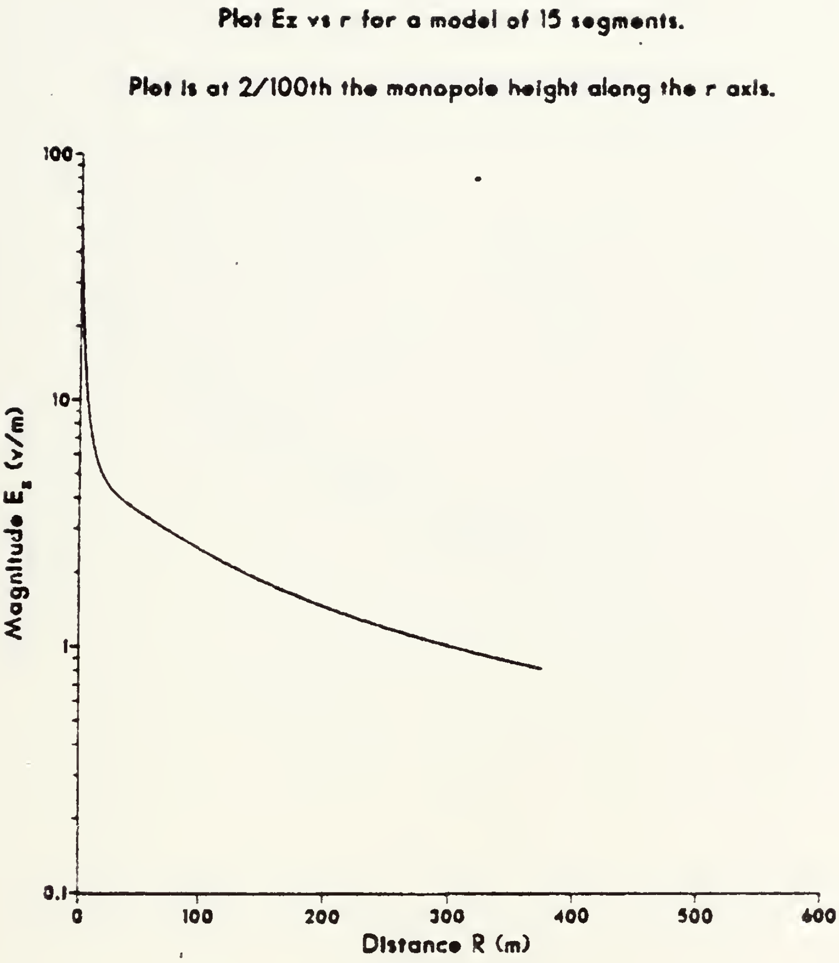

Plot Ez vs r for a model of 15 segments.

Plot is at 2/100th the monopole height along the r axis.

Figure A-19

Figures A-19 through A-23 are plots of E_z as a function of R for various heights above the ground plane.

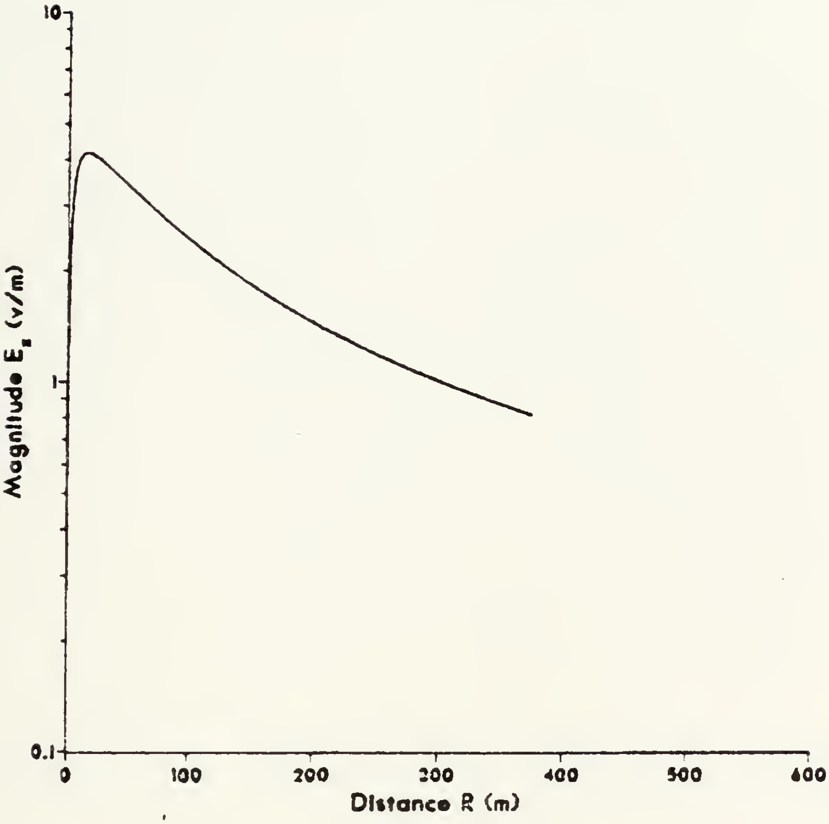

Plot Ez vs r for a model of 15 segments.

Plot is at 1/4 the monopole height along the r axis.

Figure A-20

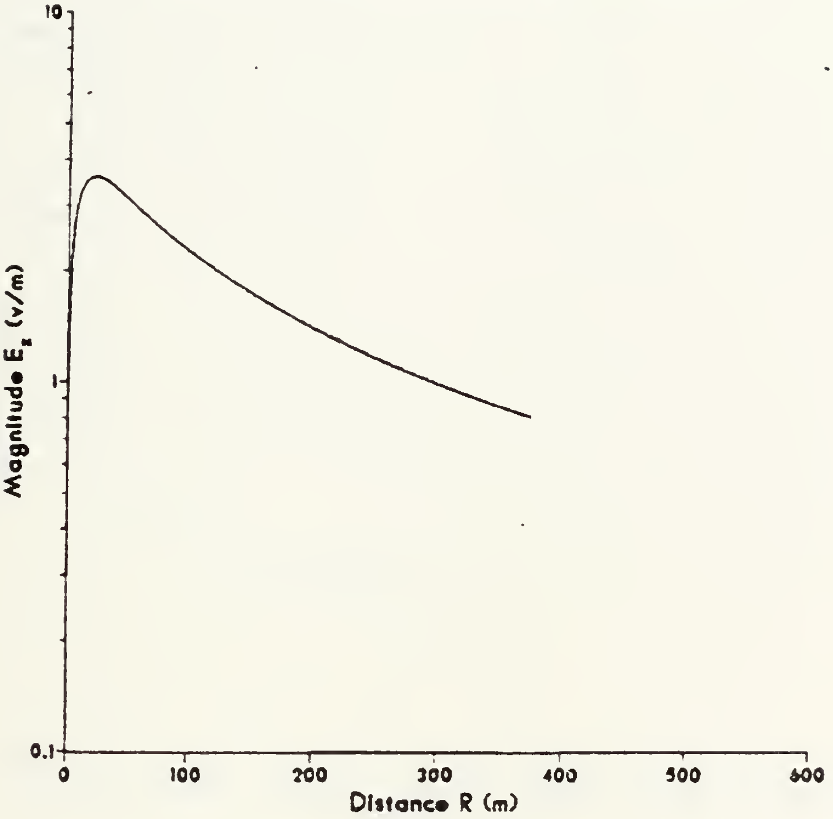

Plot Ez vs r for a model of 15 segments.

Plot is at 1/2 the monopole height along the r axis.

Figure A-21

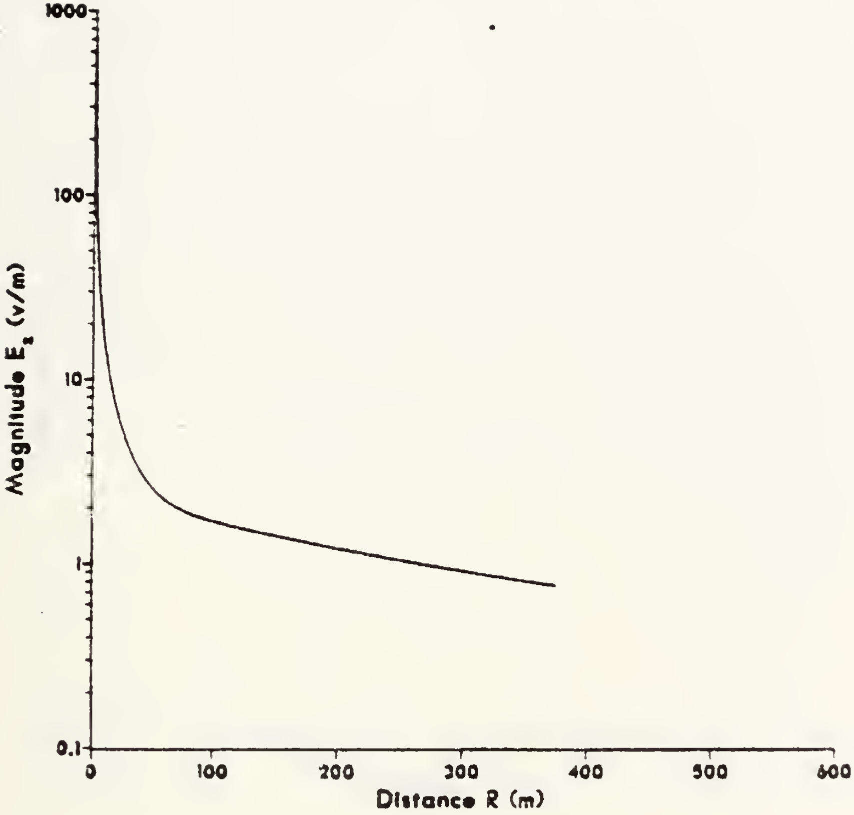

Plot Ez vs r for a model of 15 segments.

Plot is at the height of the monopole along the r axis.

Figure A-22

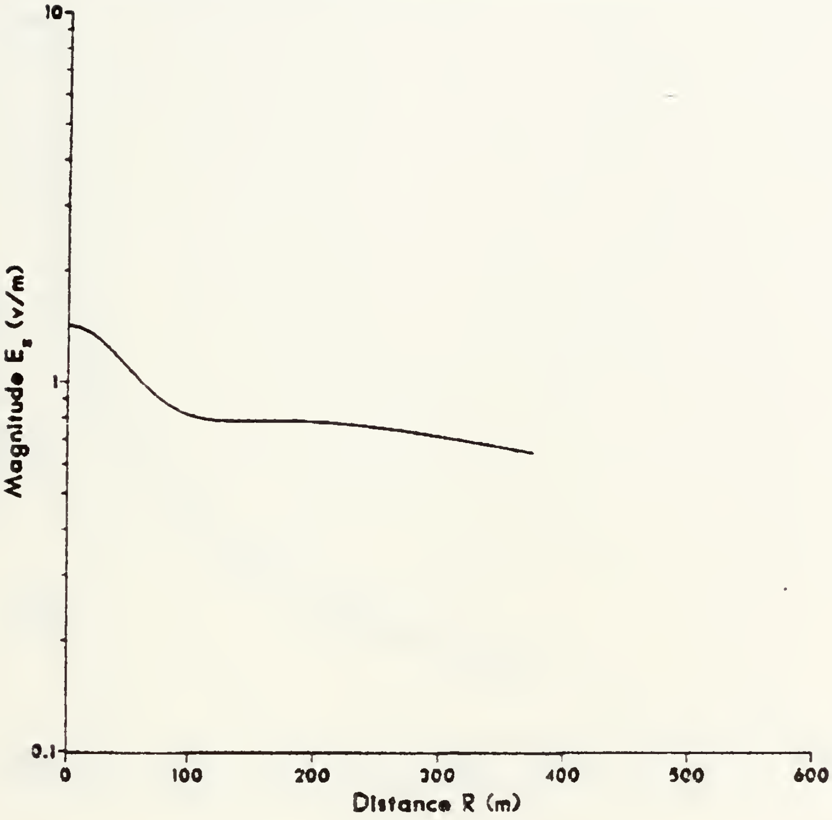

Plot Ez vs r for a model of 15 segments.

Plot is at twice the monopole height along the r axis.

Figure A-23

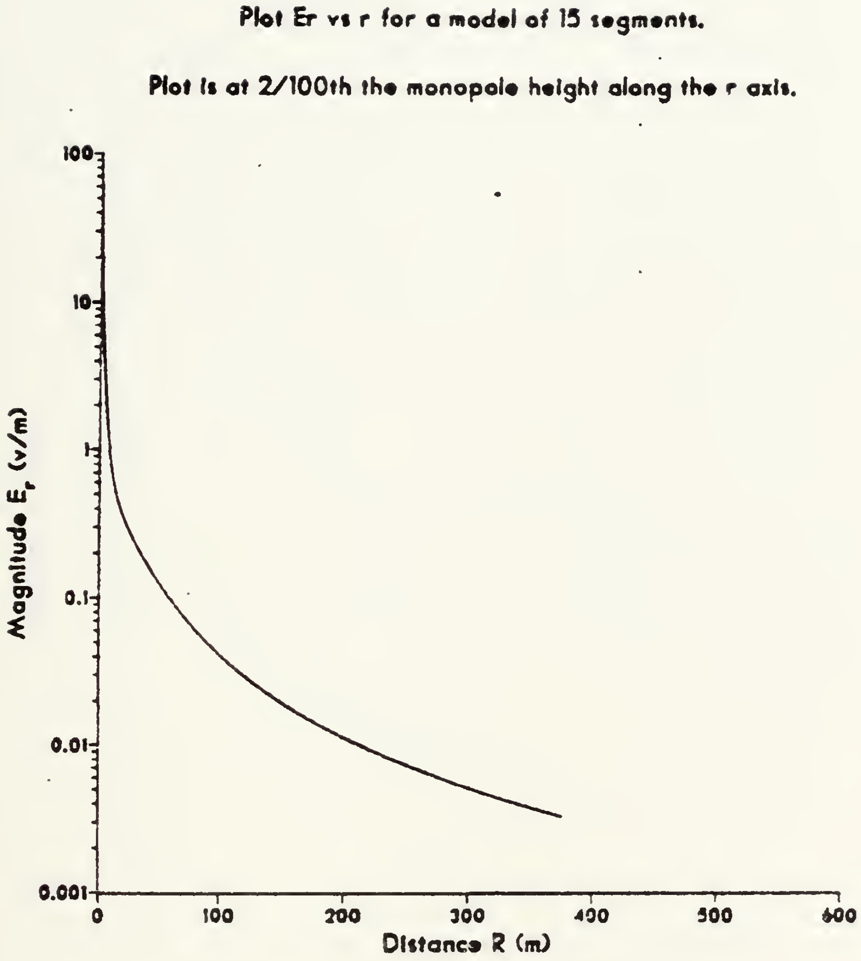

Plot Er vs r for a model of 15 segments.

Plot is at 2/100th the monopole height along the r axis.

Figure A-24

Figures A-24 through A-28 are plots of E_R as a function of R for various heights above the ground plane.

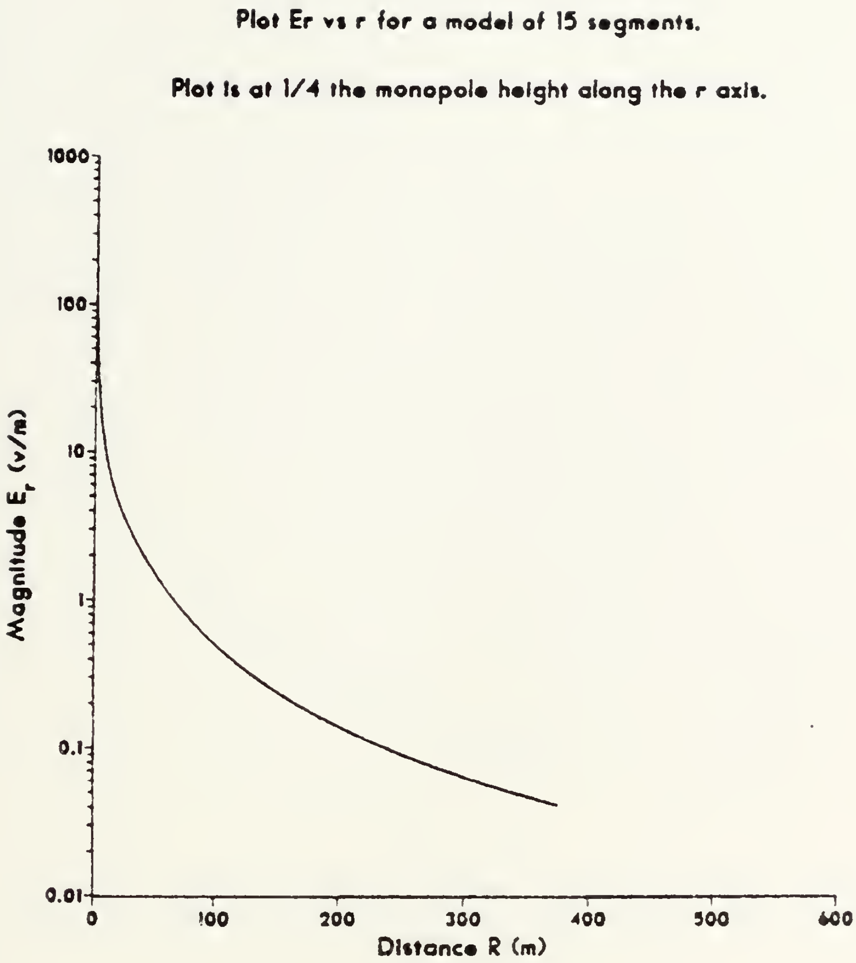

Plot Er vs r for a model of 15 segments.

Plot is at 1/4 the monopole height along the r axis.

Figure A-25

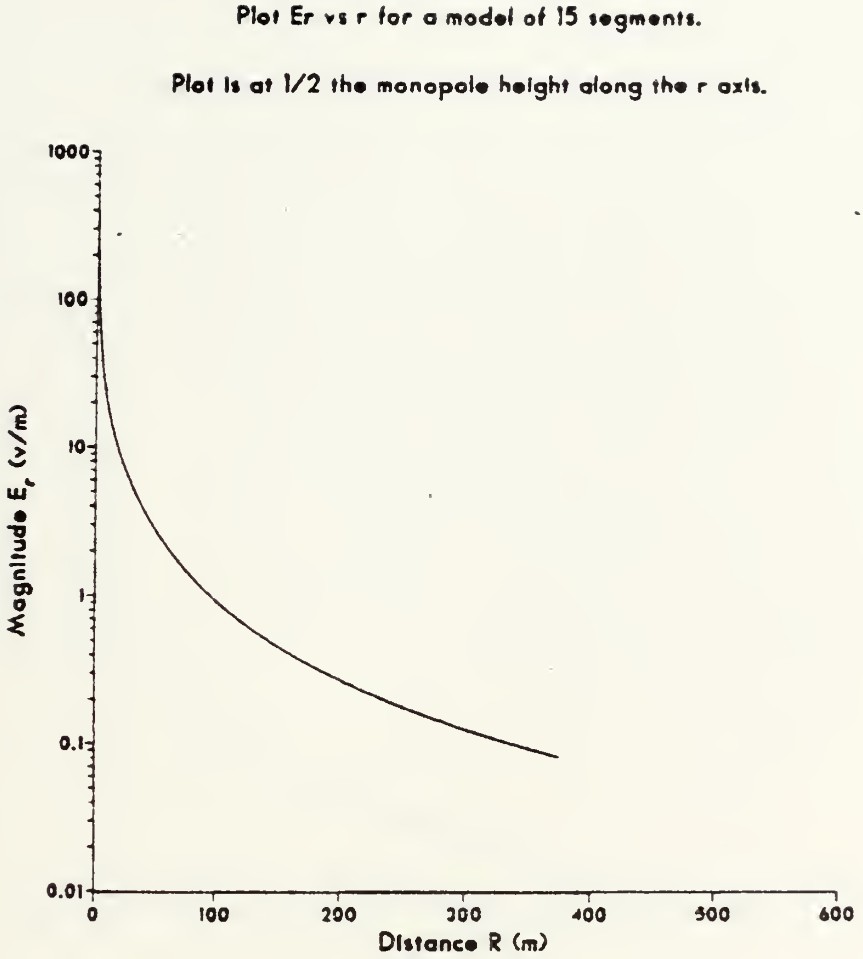

Plot Er vs r for a model of 15 segments.

Plot is at 1/2 the monopole height along the r axis.

Figure A-26

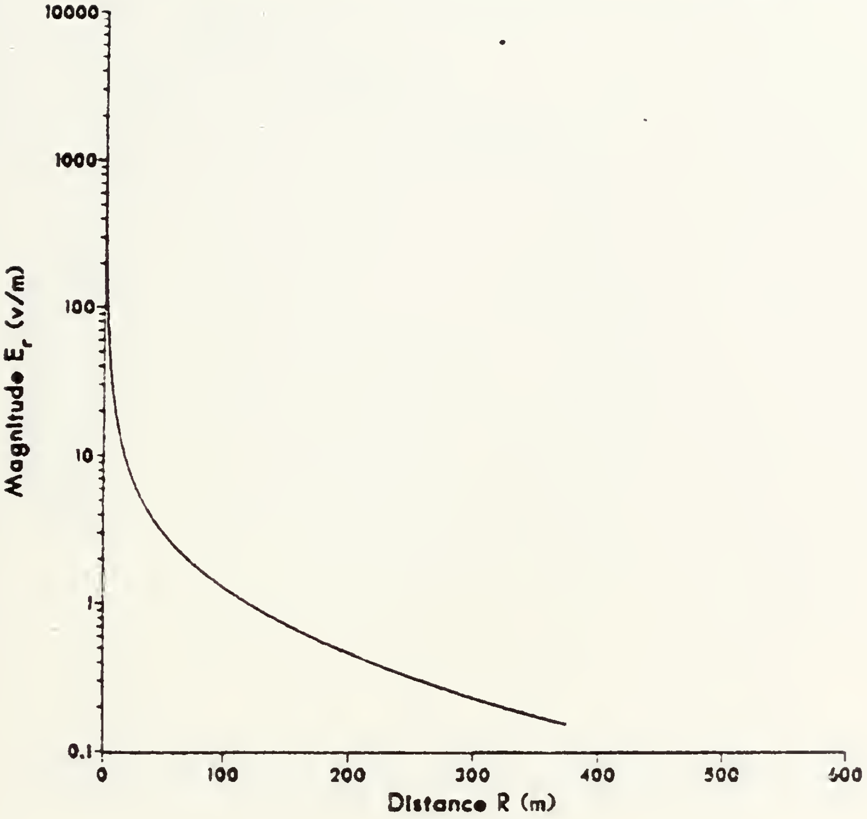

Plot Er vs r for a model of 15 segments.

Plot is at the height of the monopole along the r axis.

Figure A-27

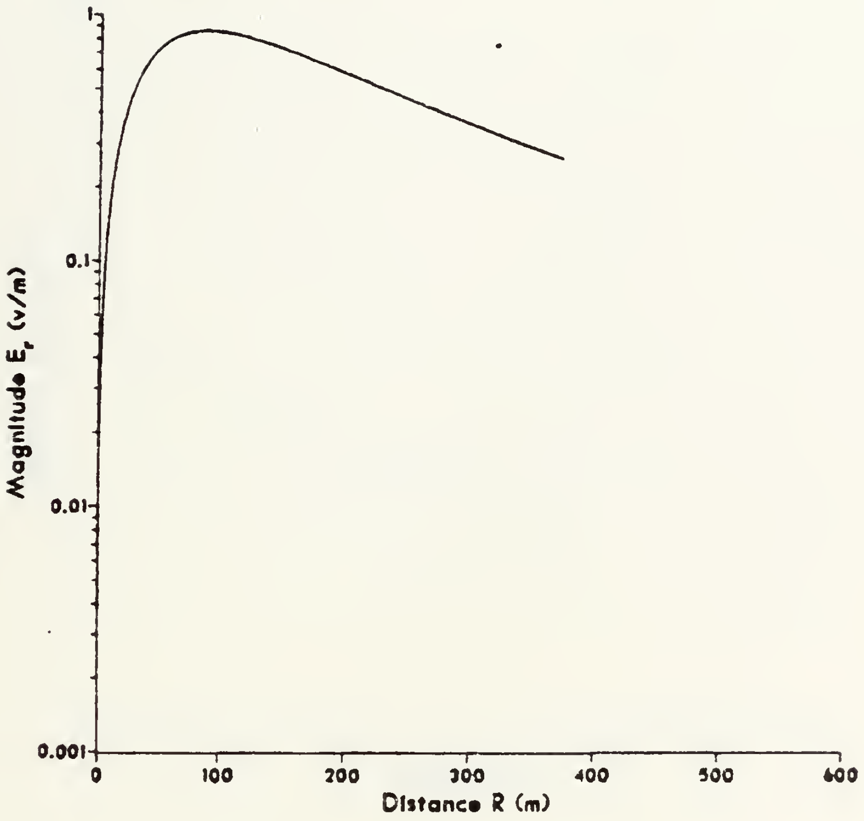

Plot Er vs r for a model of 15 segments.

Plot is at twice the monopole height along the r axis.

Figure A-28

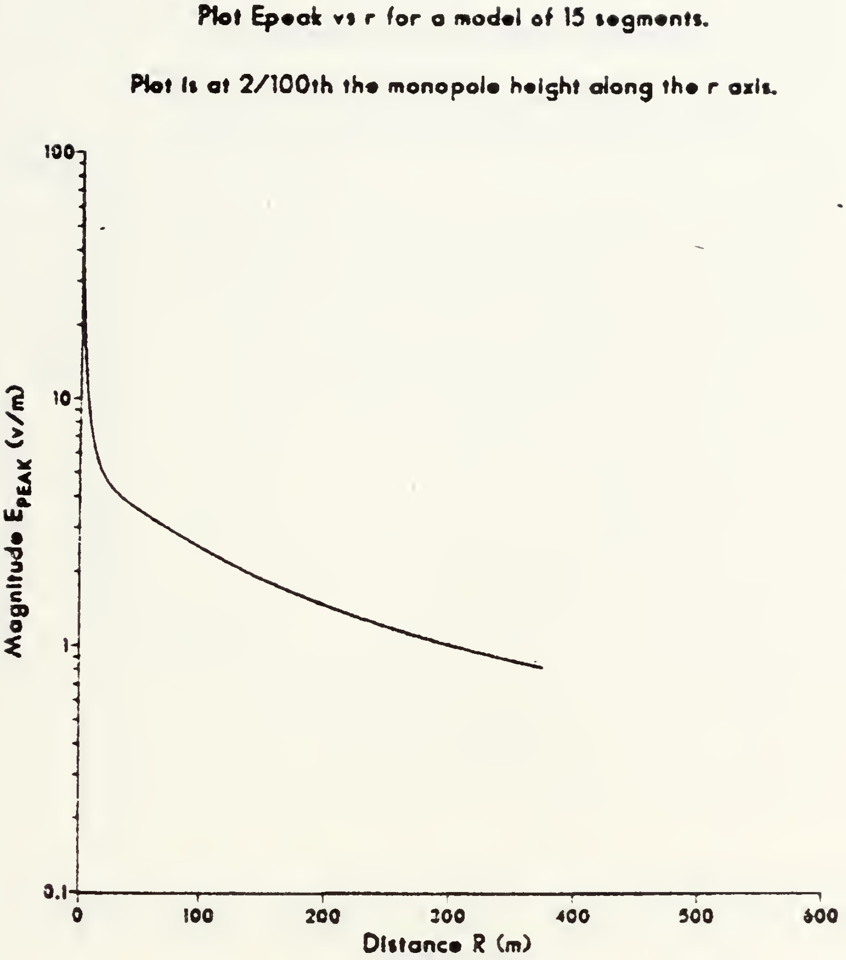

Plot Epeak vs r for a model of 15 segments.

Plot is at 2/100th the monopole height along the r axis.

Figure A-29

Figure A-29 through A-33 are plots of E_{peak} as a function of R for various heights above the ground plane.

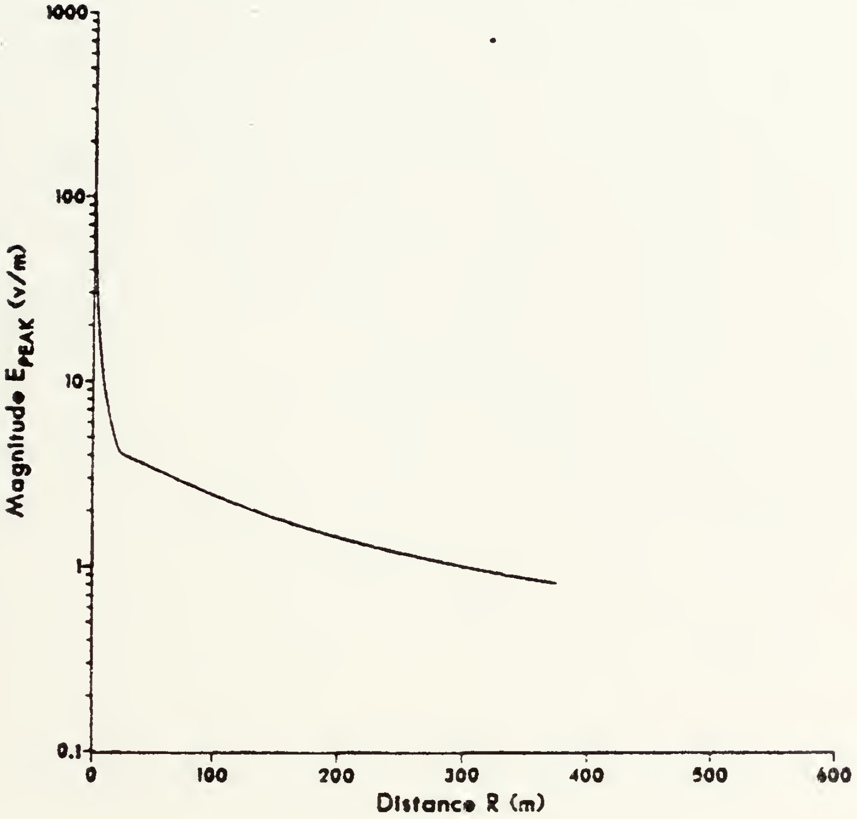

Plot Epeak vs r for a model of 15 segments.

Plot is at 1/4 the monopole height along the r axis.

Figure A-30

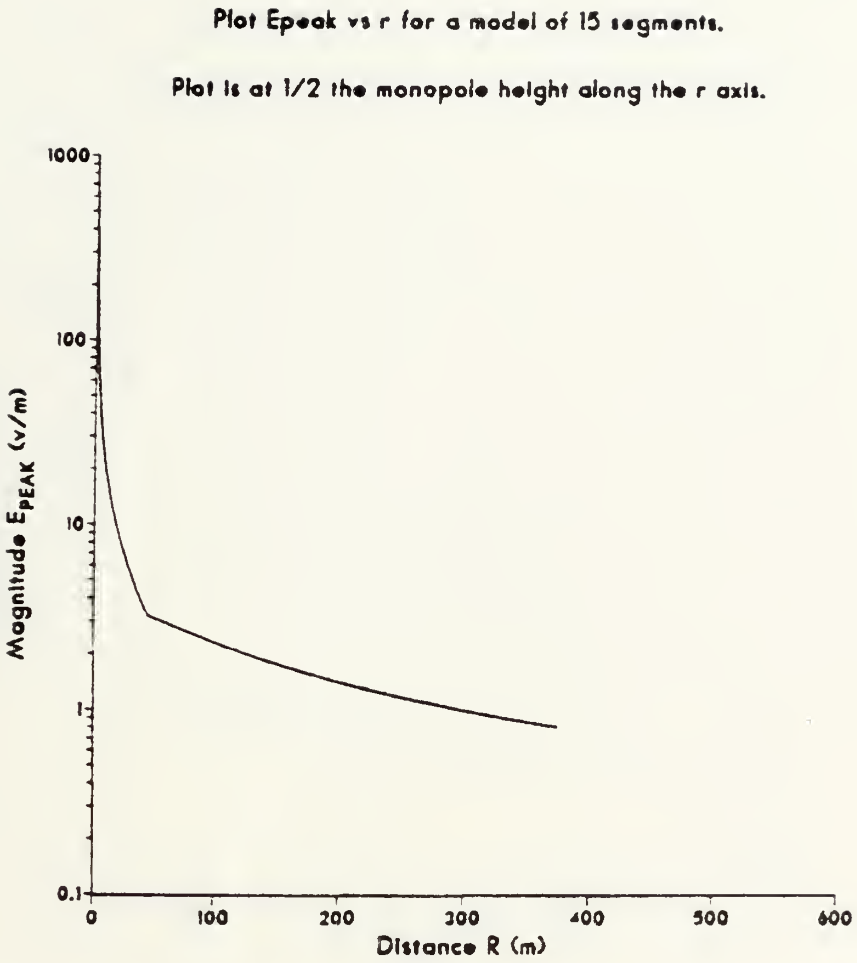
Plot Epeak vs r for a model of 15 segments.
Plot is at 1/2 the monopole height along the r axis.
1000
100
10
1
0.1
Magnitude E_{PEAK} (v/m)
0
100
200
300
400
500
600
Distance R (m)

Figure A-31

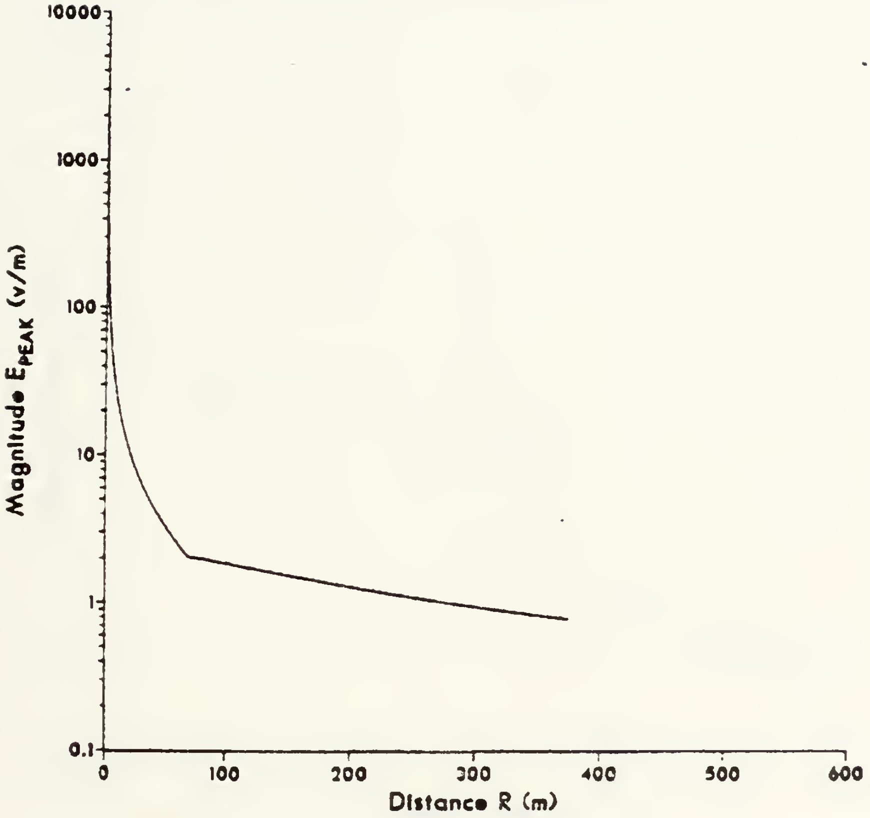

Plot Epeak vs r for a model of 15 segments.

Plot is at the height of the monopole along the r axis.

Figure A-32

Plot Epeak vs r for a model of 15 segments.

Plot is at twice the monopole height along the r axis.

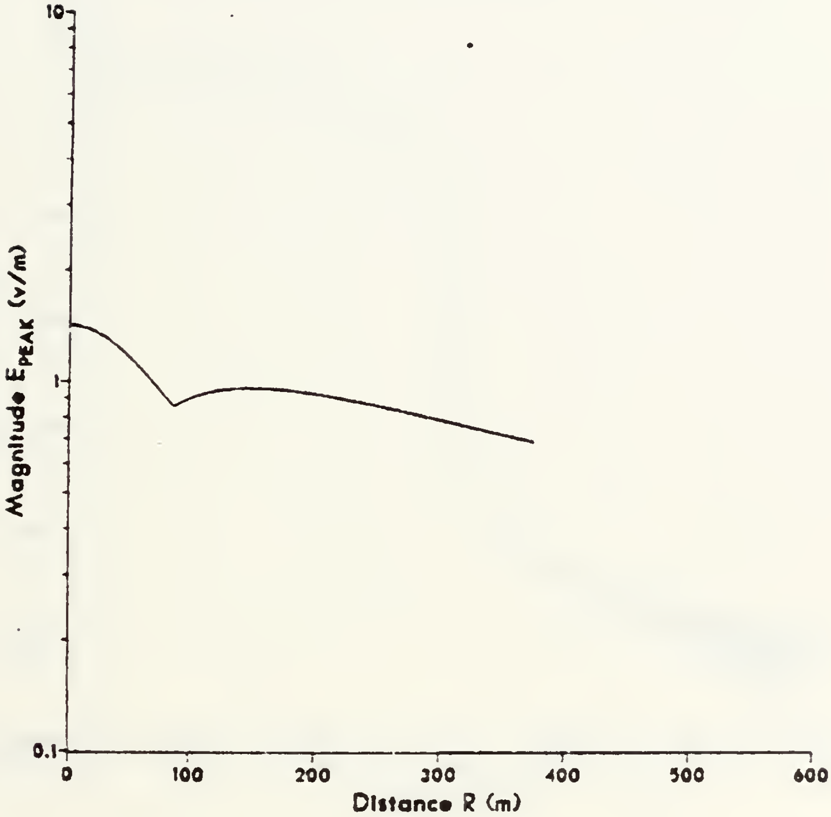

Figure A-33

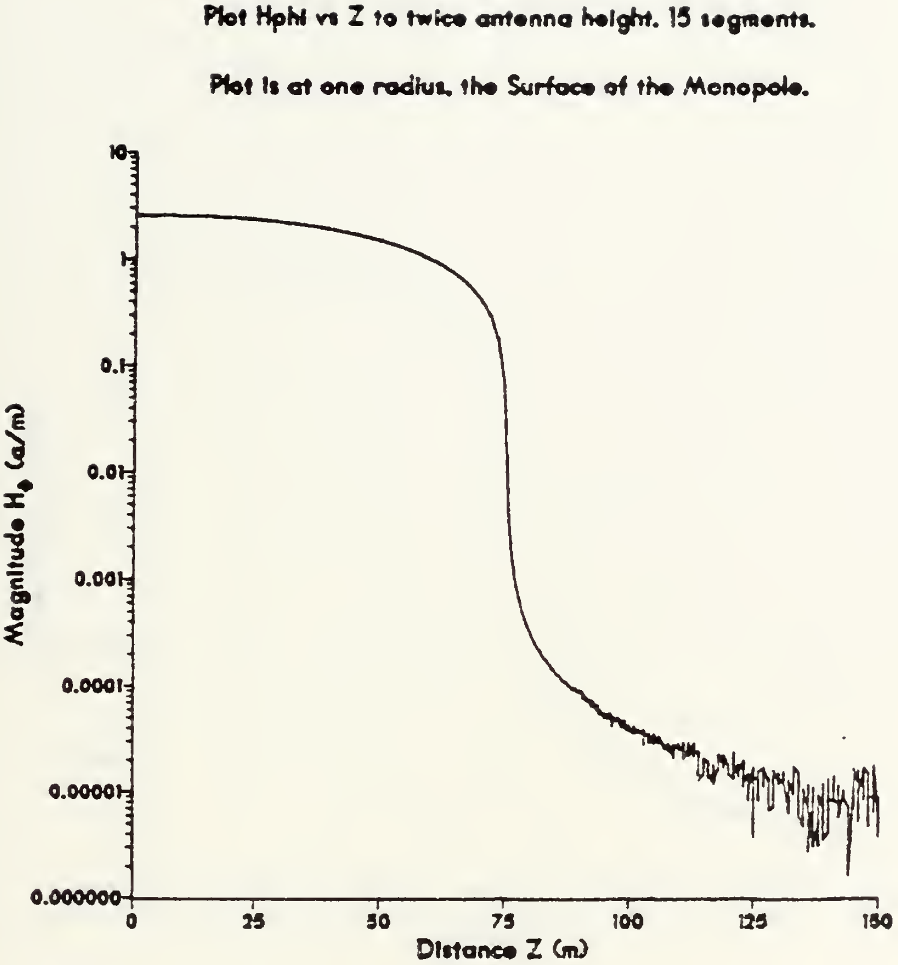

Figure A-34

Figures A-34 through A-39 are plots of H_ϕ as a function of Z for various distances from the Z-axis.

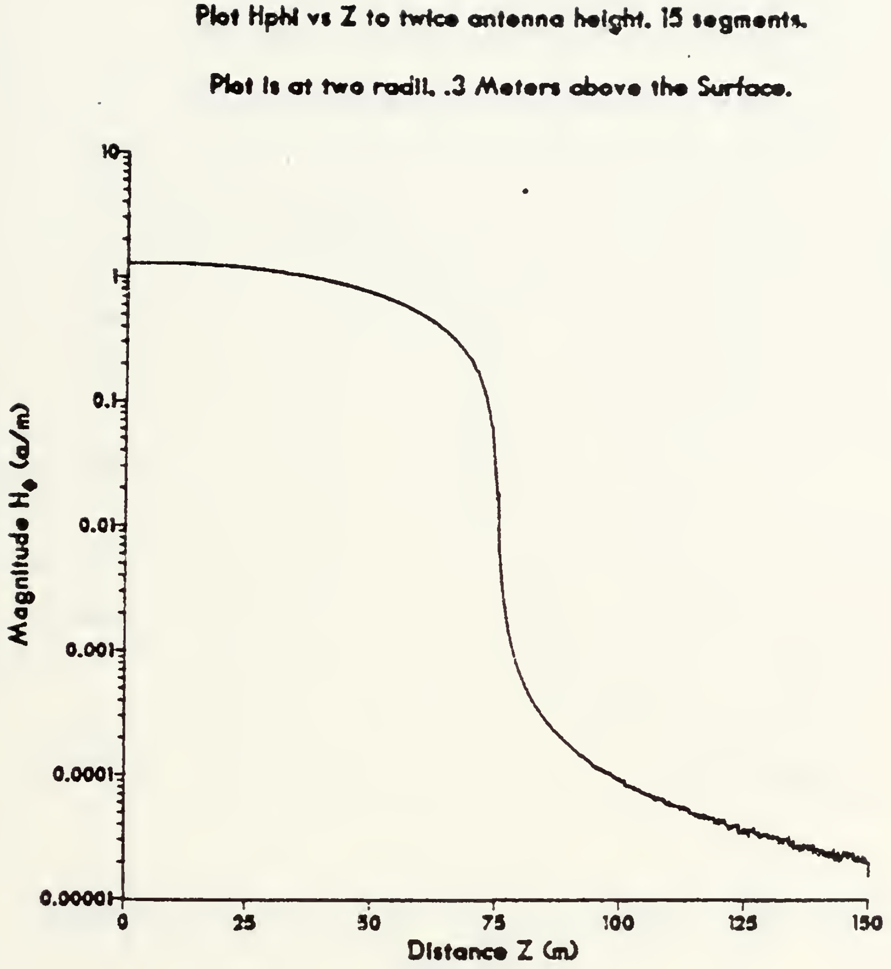
Plot Hphi vs Z to twice antenna height. 15 segments.

Plot is at two radii. .3 Meters above the Surface.

Figure A-35

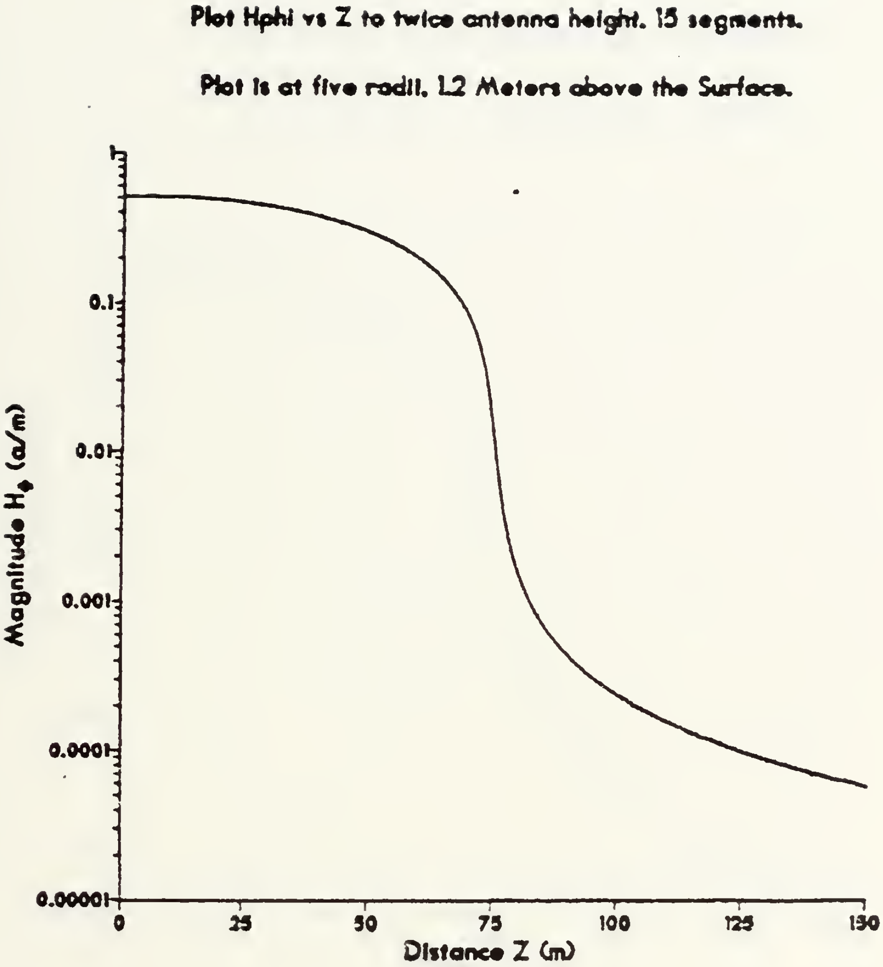
Plot Hphi vs Z to twice antenna height. 15 segments.
Plot is at five radii. 1.2 Meters above the Surface.
Magnitude H_ϕ (a/m)
1
0.1
0.01
0.001
0.0001
0.00001
0
25
50
75
100
125
150
Distance Z (m)

Figure A-36

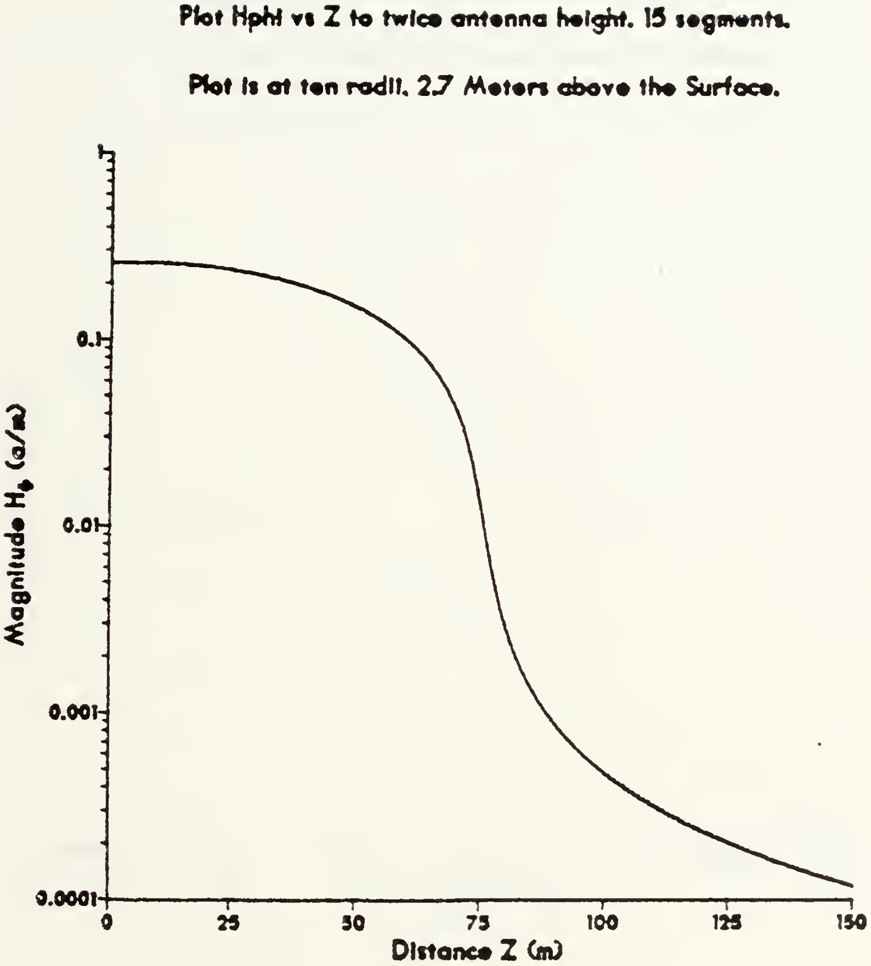

Plot Hphi vs Z to twice antenna height. 15 segments.

Plot is at ten radii. 2.7 Meters above the Surface.

Figure A-37

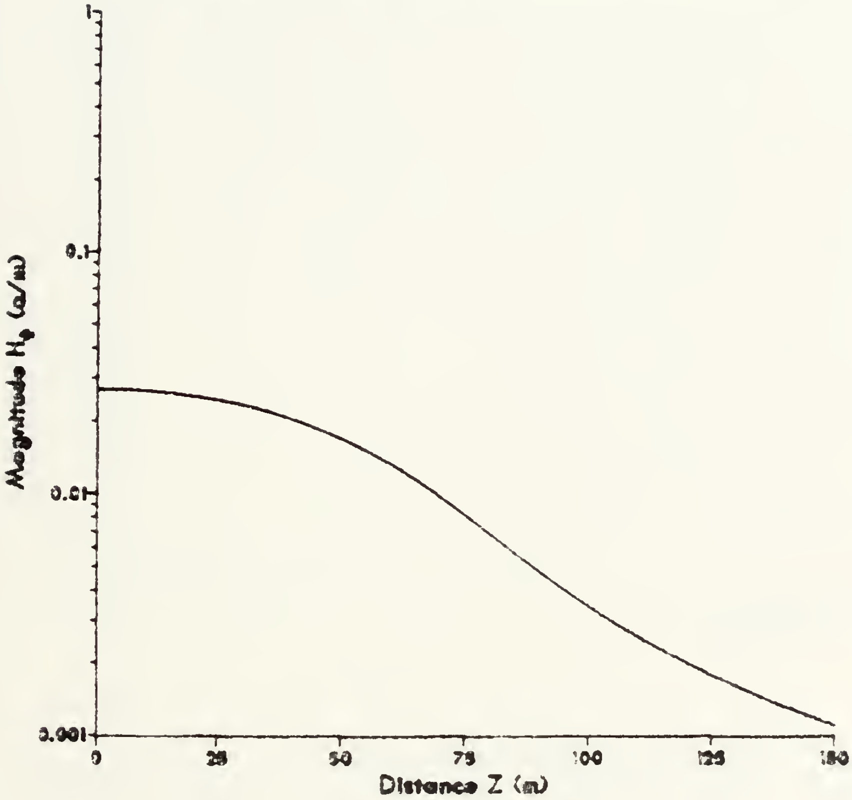

Plot Hphi vs Z to twice antenna height. 15 segments.

Plot is at 100 radii, 29.7 Meters above the Surface.

Figure A-38

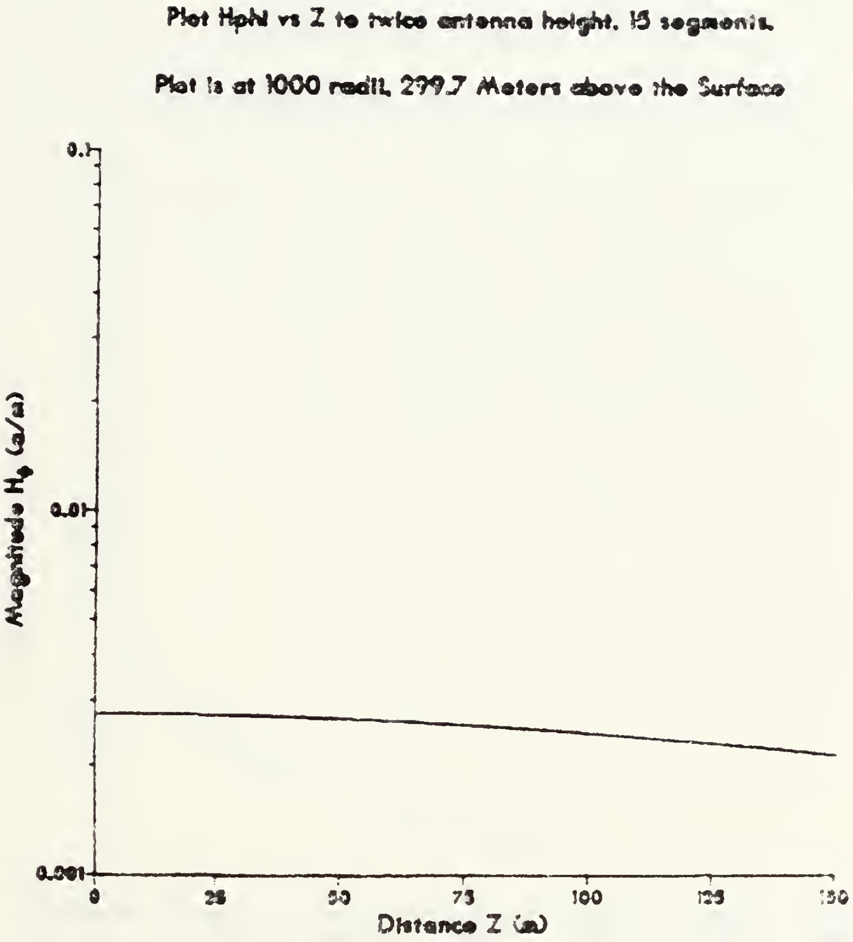
Plot Hphi vs Z to twice antenna height. 15 segments.
Plot is at 1000 radii, 299.7 Meters above the Surface
Magnitude H_ϕ (a/m)
0.1
0.01
0.001
0
25
50
75
100
125
150
Distance Z (m)

Figure A-39

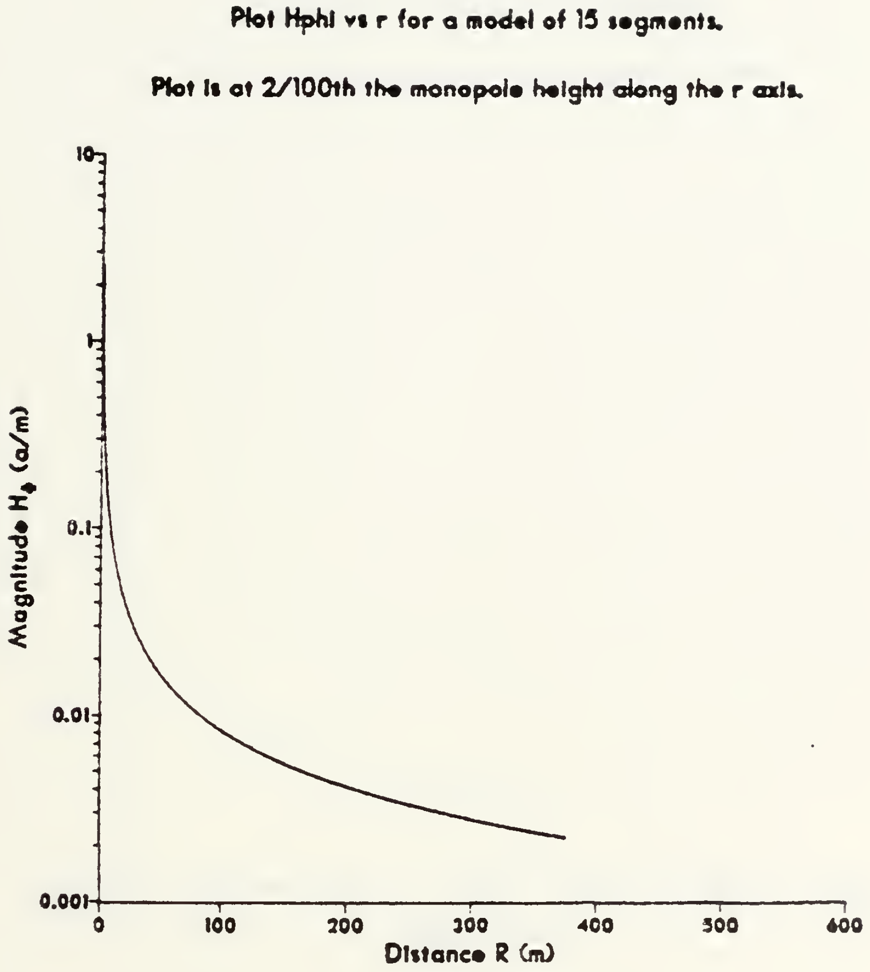
Plot Hphi vs r for a model of 15 segments.

Plot is at 2/100th the monopole height along the r axis.

Figure A-40

Figures A-40 through A-44 are plots of H_ϕ as a function of R for various heights above the ground plane.

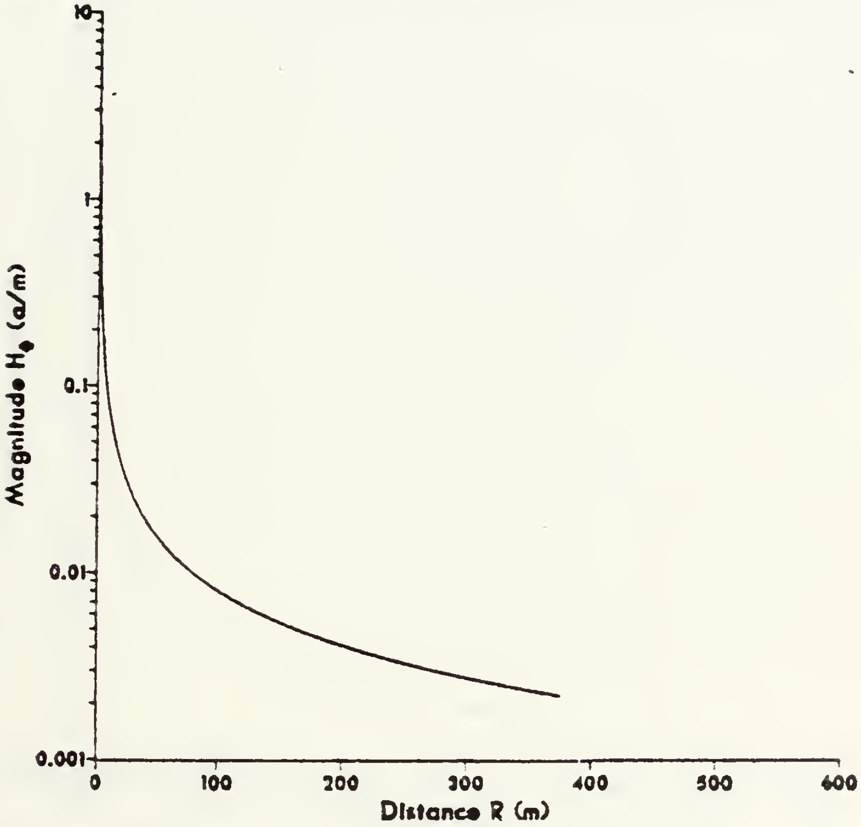

Plot Hphi vs r for a model of 15 segments.

Plot is at 1/4 the monopole height along the r axis.

Figure A-41

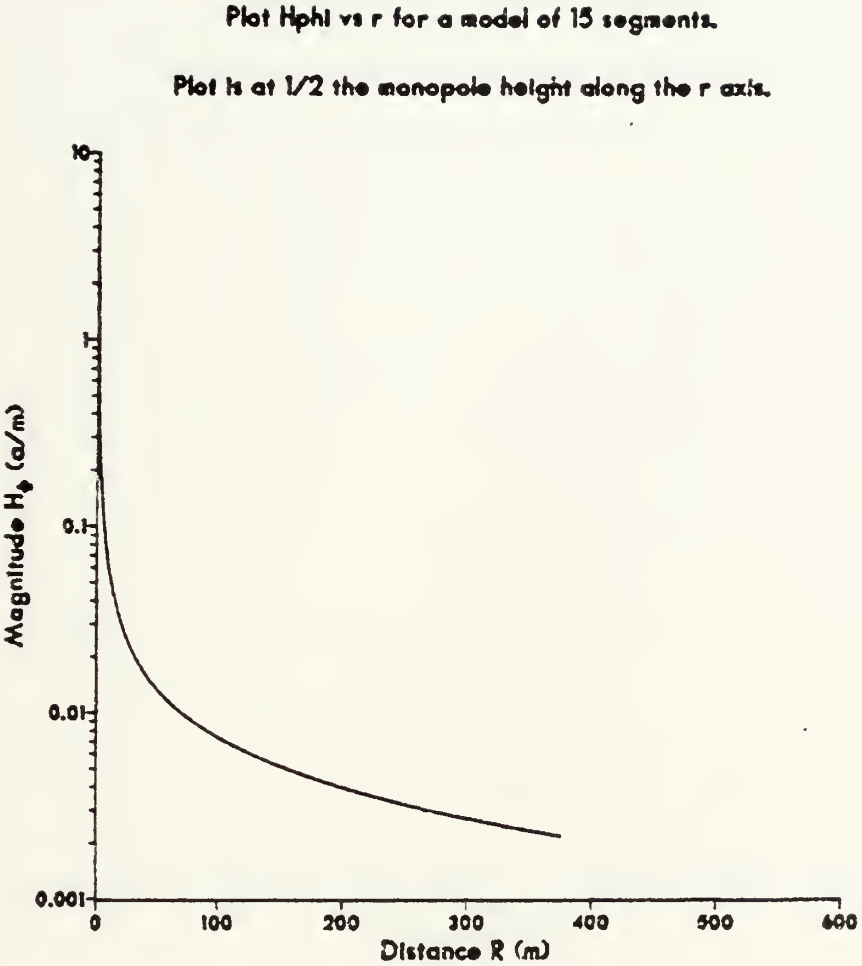

Plot Hphi vs r for a model of 15 segments.

Plot is at 1/2 the monopole height along the r axis.

Figure A-42

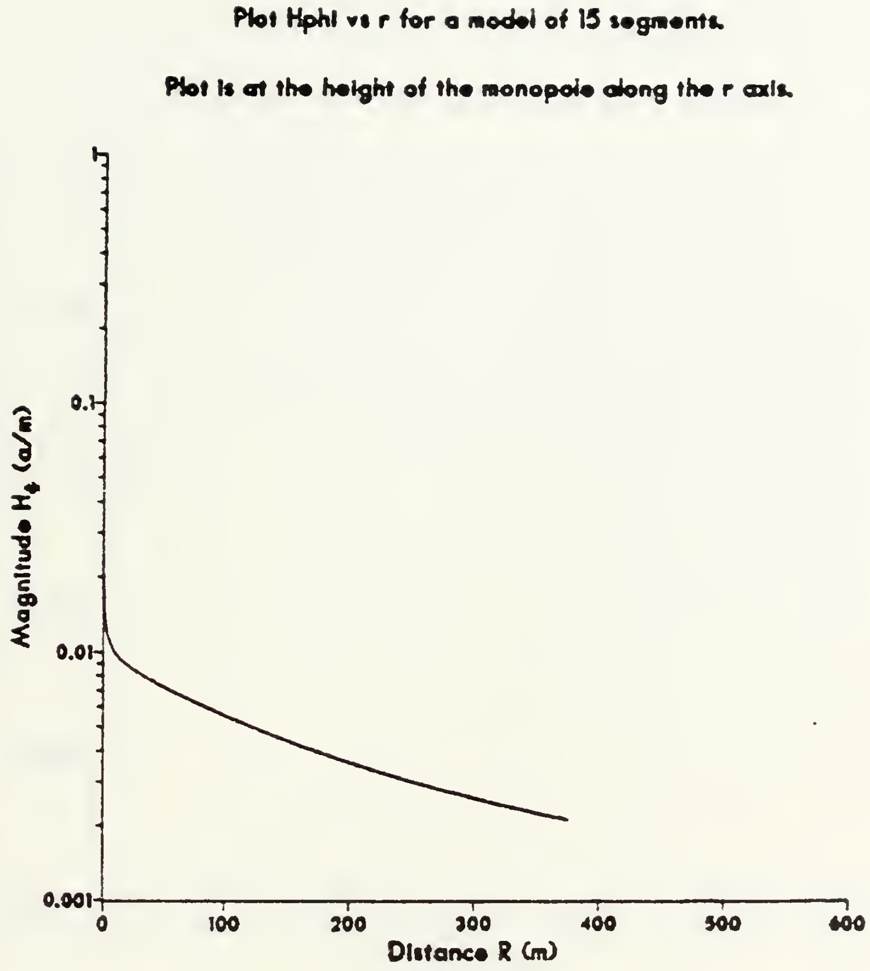

Plot Hphi vs r for a model of 15 segments.

Plot is at the height of the monopole along the r axis.

Figure A-43

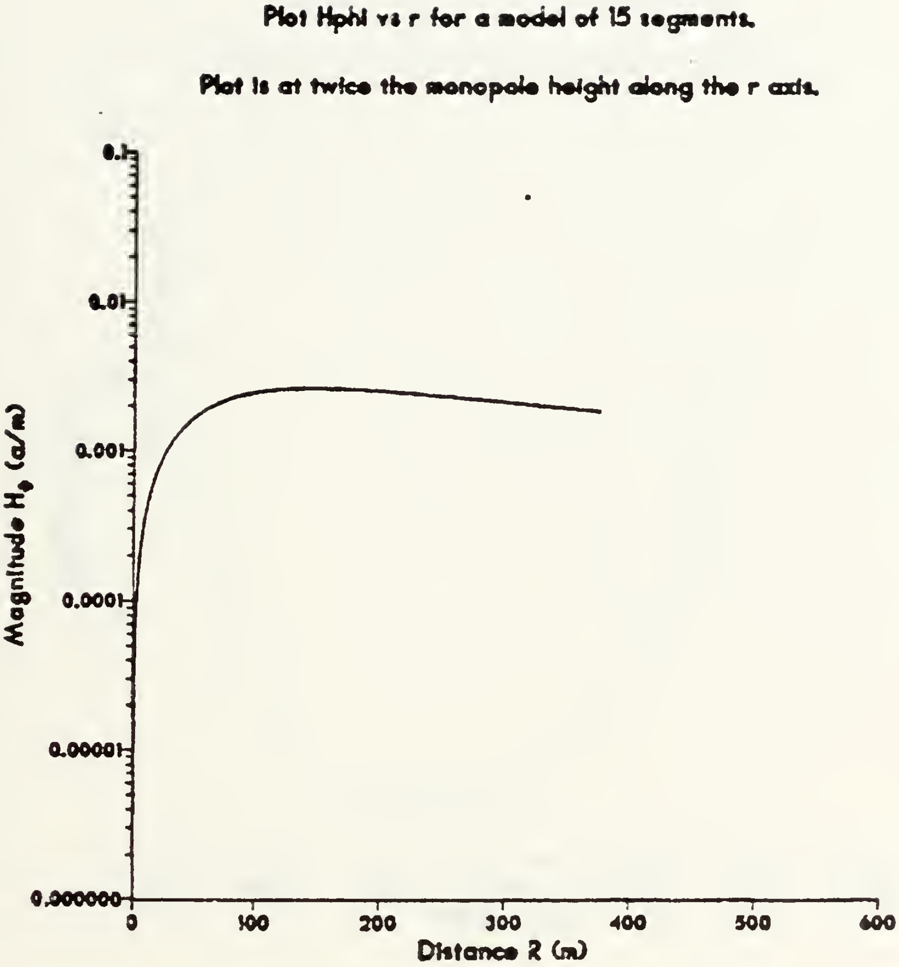
Plot Hphi vs r for a model of 15 segments.

Plot is at twice the monopole height along the r axis.

Figure A-44

APPENDIX B

Plot Ez vs z for a model of 19 segments.

Plot is .3 cm from monopole axis along the z axis.

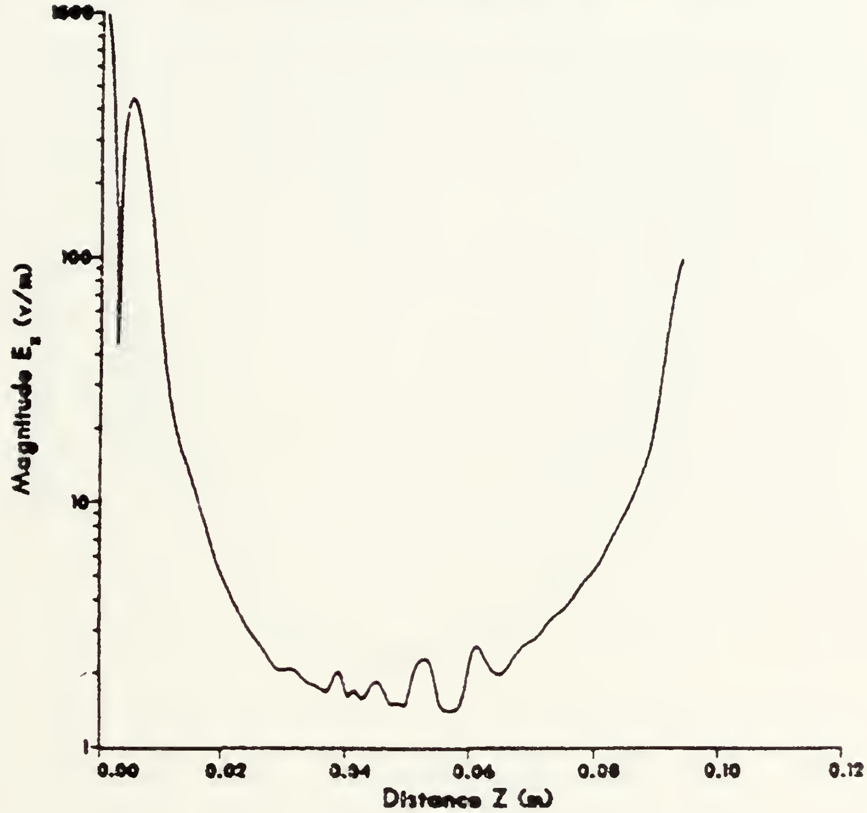

Figure B-1

Figures B-1 through B-8 are plots of E_z as a function of Z for various distances from the Z-axis.

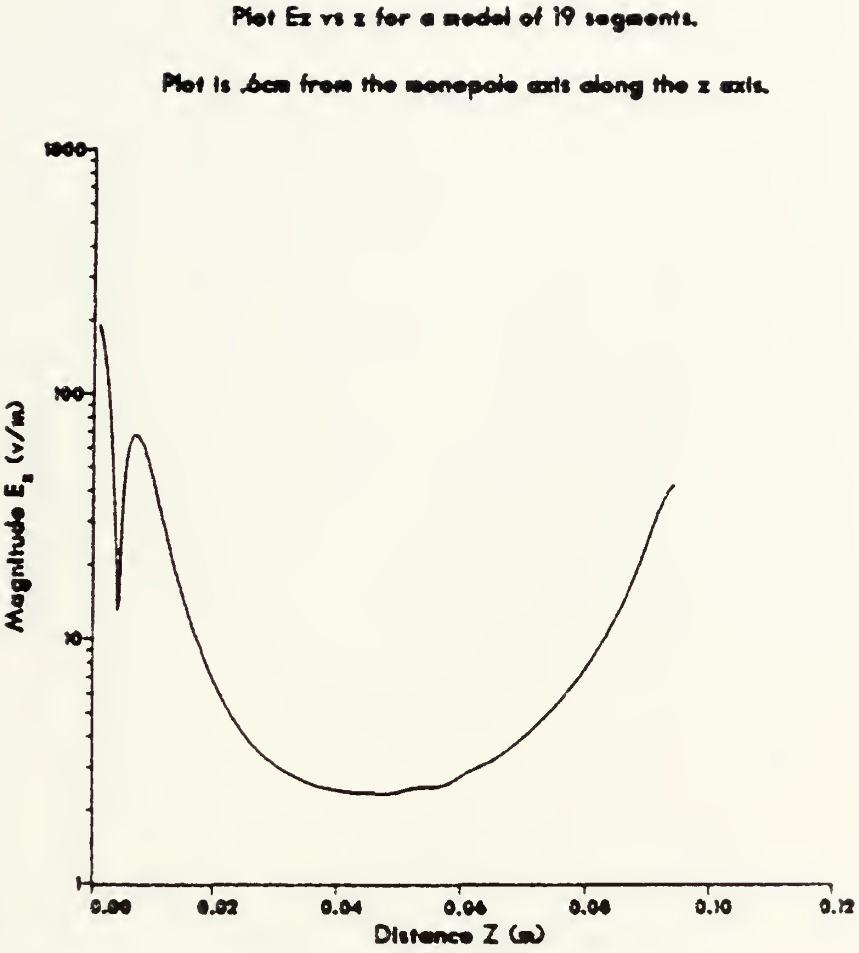

Plot Ez vs z for a model of 19 segments.

Plot is .6cm from the monopole axis along the z axis.

Figure B-2

Plot Ez vs z for a model of 19 segments.

Plot is 1 cm from the monopole axis along the z axis.

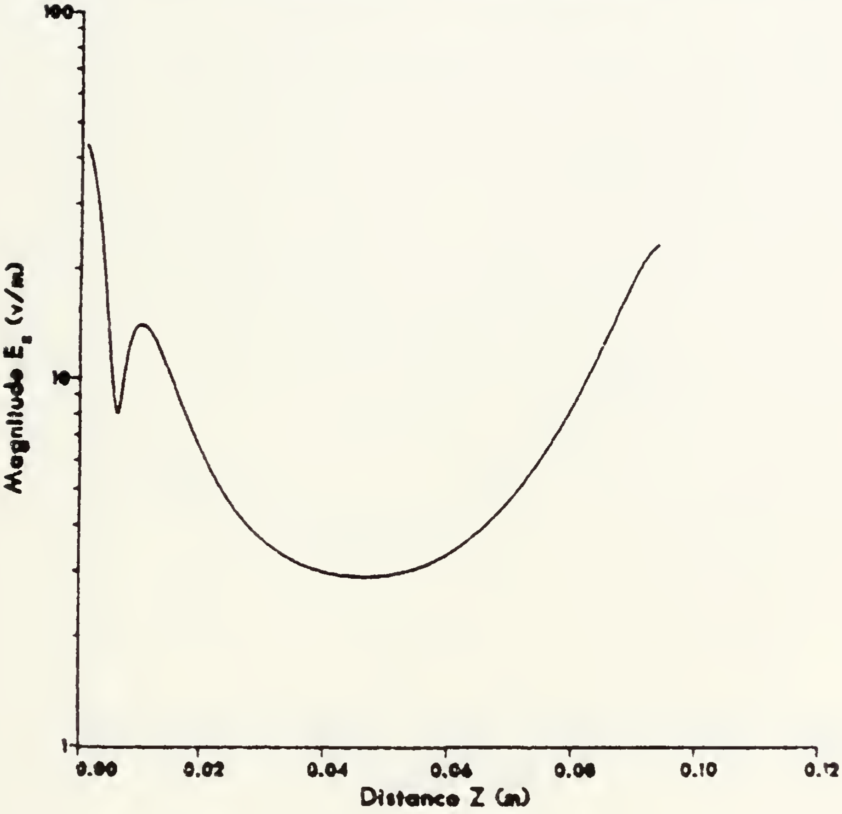

Figure B-3

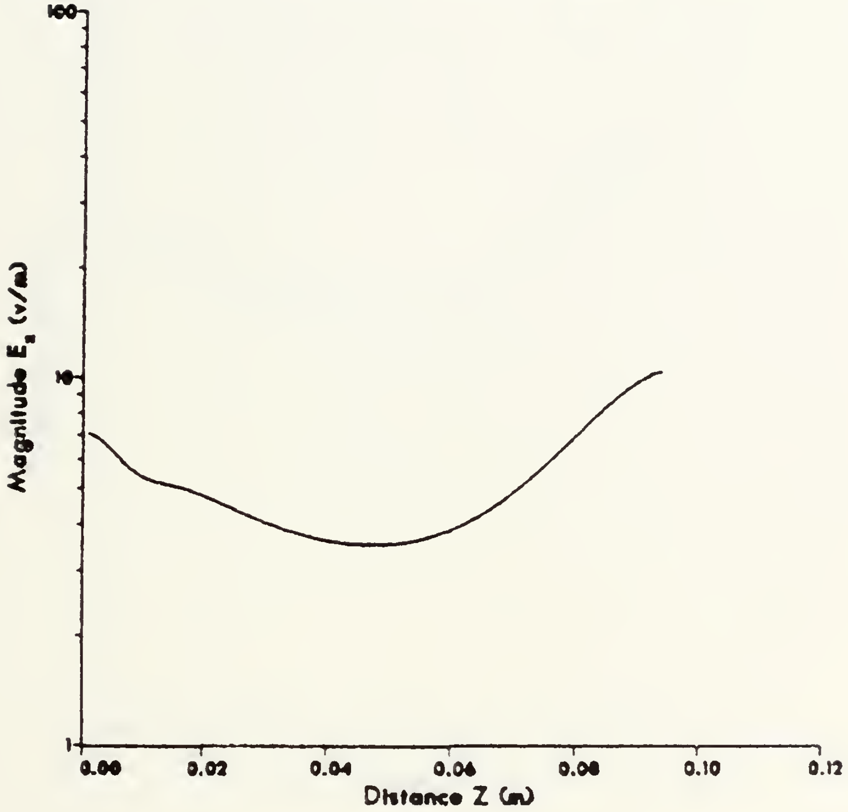

Plot Ez vs z for a model of 19 segments.

Plot is 2 cm from the monopole axis along the z axis.

Figure B-4

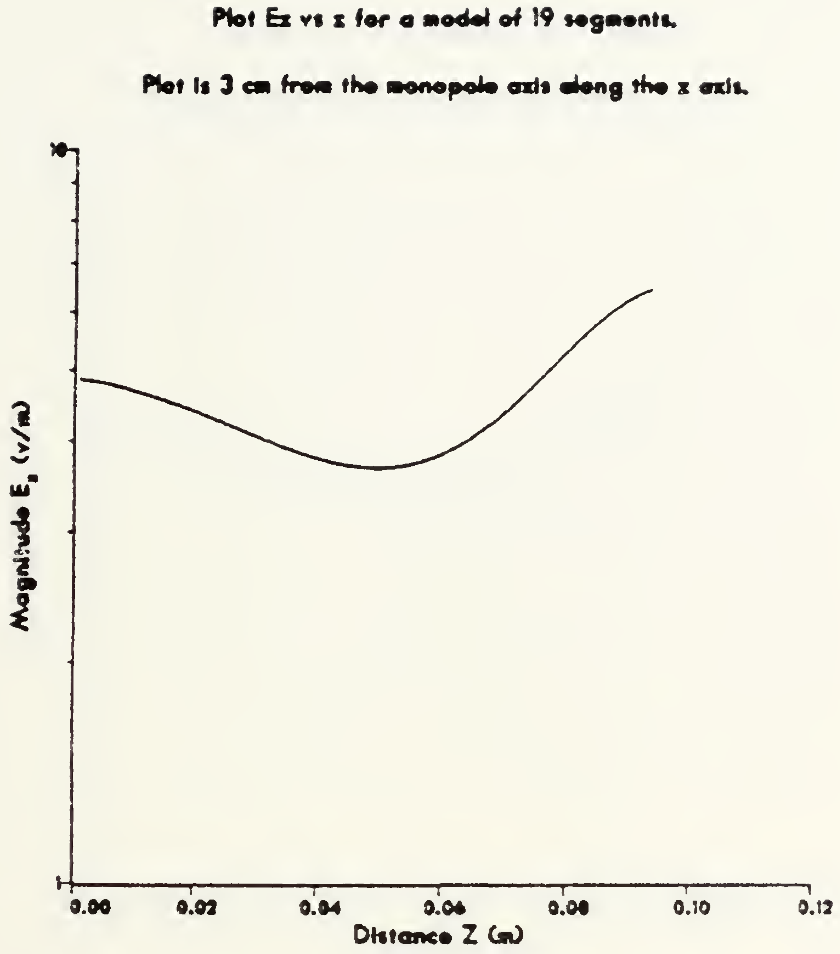

Plot Ez vs z for a model of 19 segments.

Plot is 3 cm from the monopole axis along the x axis.

Figure B-5

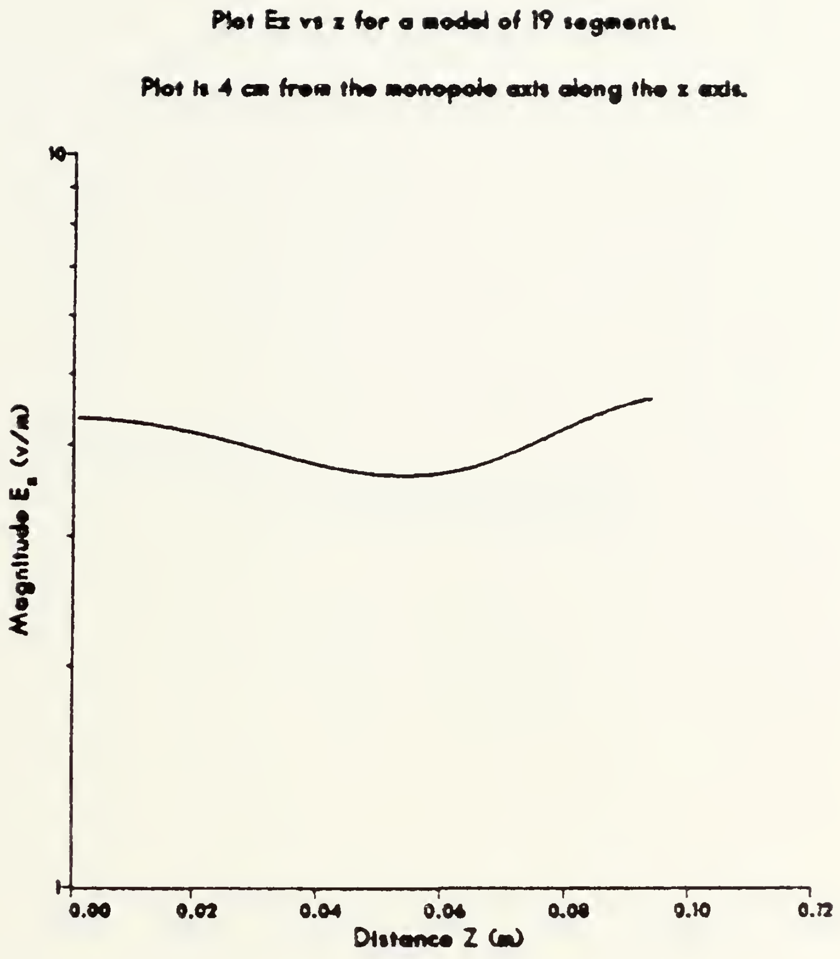
Plot Ez vs z for a model of 19 segments.
Plot is 4 cm from the monopole axis along the x axis.
10
1
Magnitude E_z (v/m)
0.00
0.02
0.04
0.06
0.08
0.10
0.12
Distance Z (m)

Figure B-6

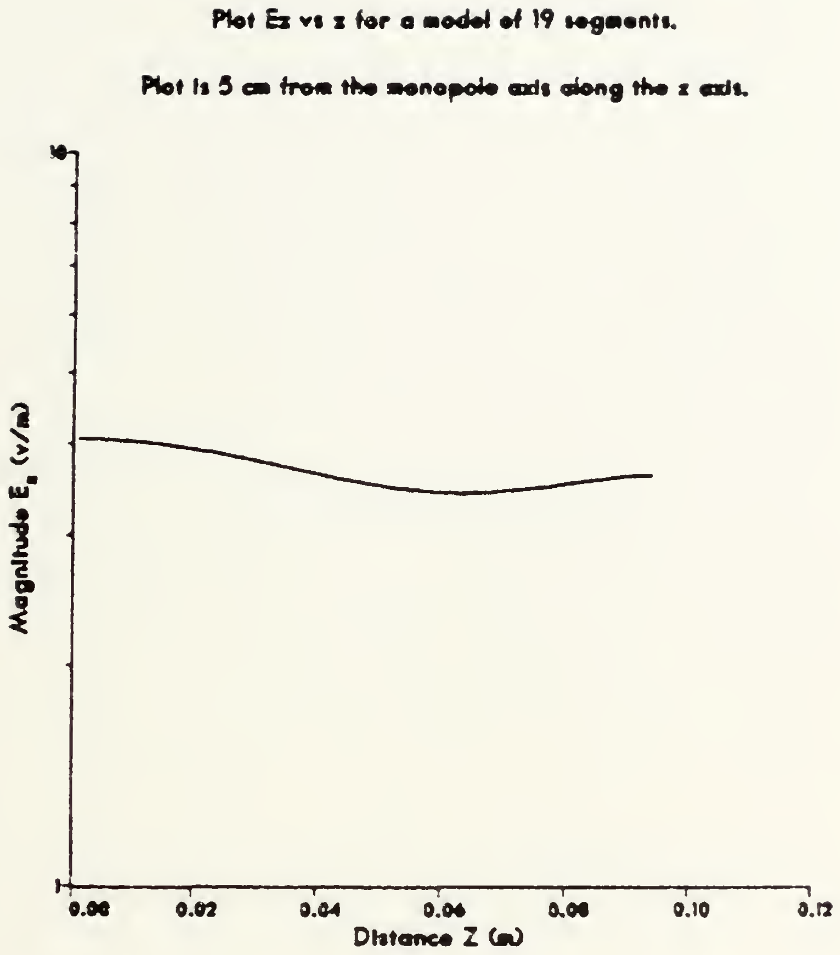

Plot Ez vs z for a model of 19 segments.

Plot is 5 cm from the monopole axis along the z axis.

Figure B-7

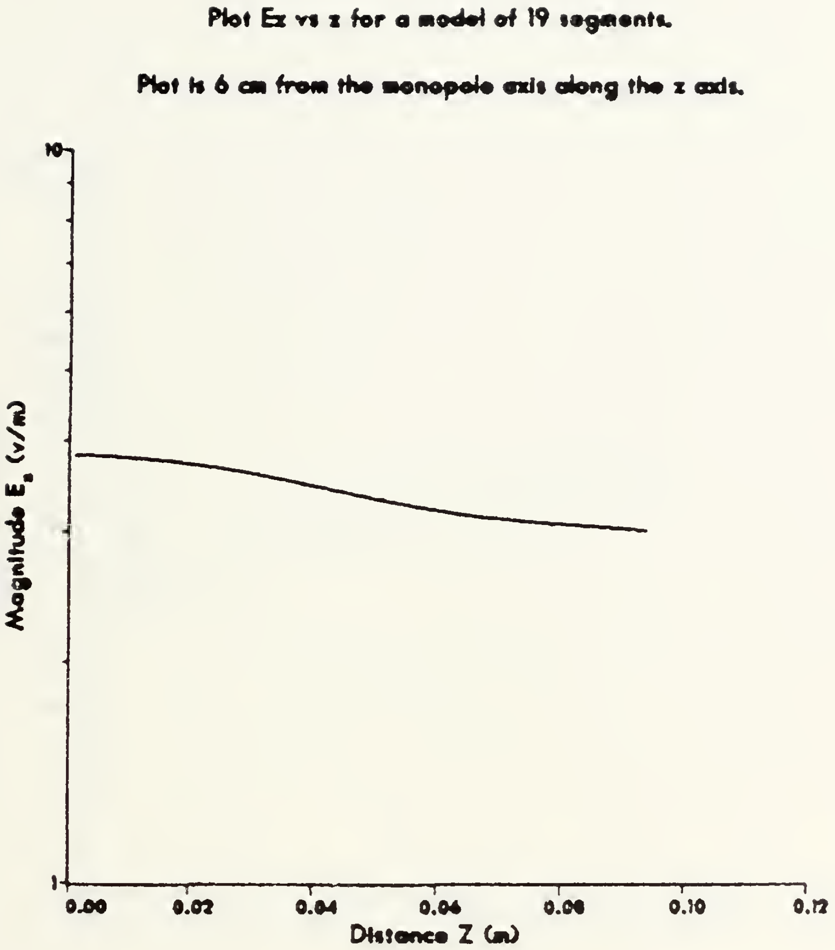
Plot Ez vs z for a model of 19 segments.

Plot is 6 cm from the monopole axis along the z axis.

Figure B-8

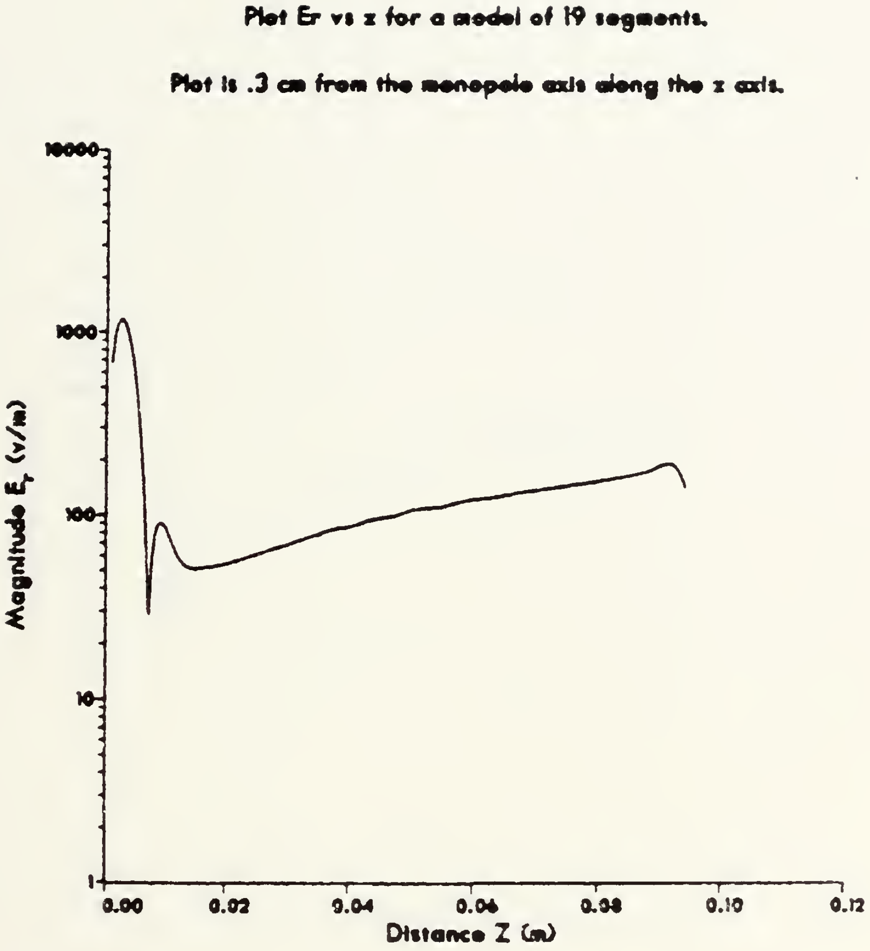

Figure B-9

Figures B-9 through B-16 are plots of E_R as a function of Z for various distances from the Z-axis.

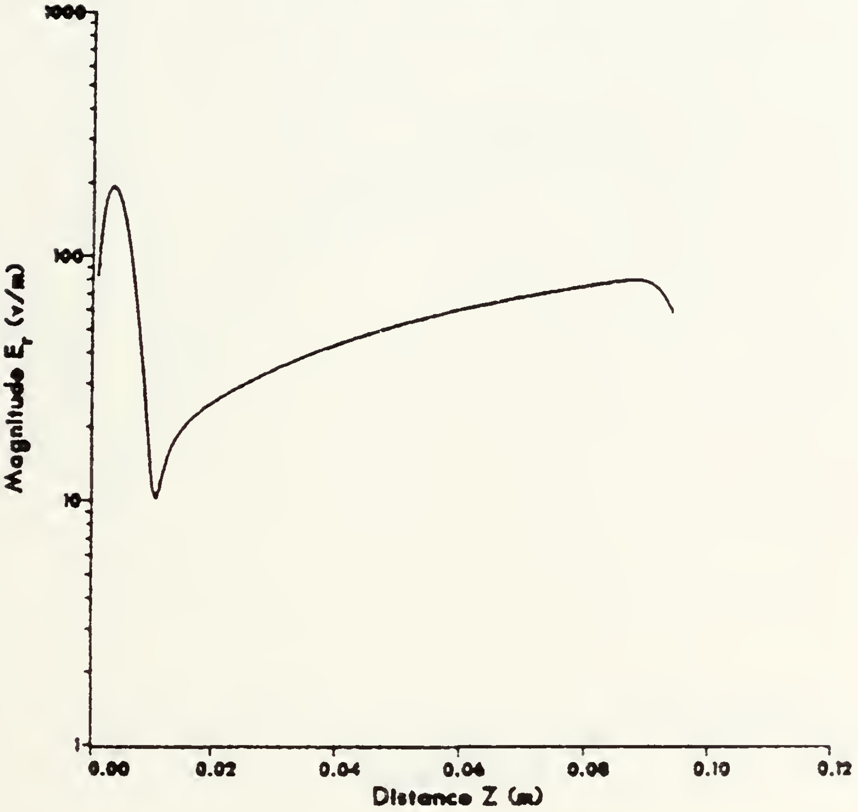

Plot Er vs z for a model of 19 segments.

Plot is .6cm from the monopole axis along the z axis.

Figure B-10

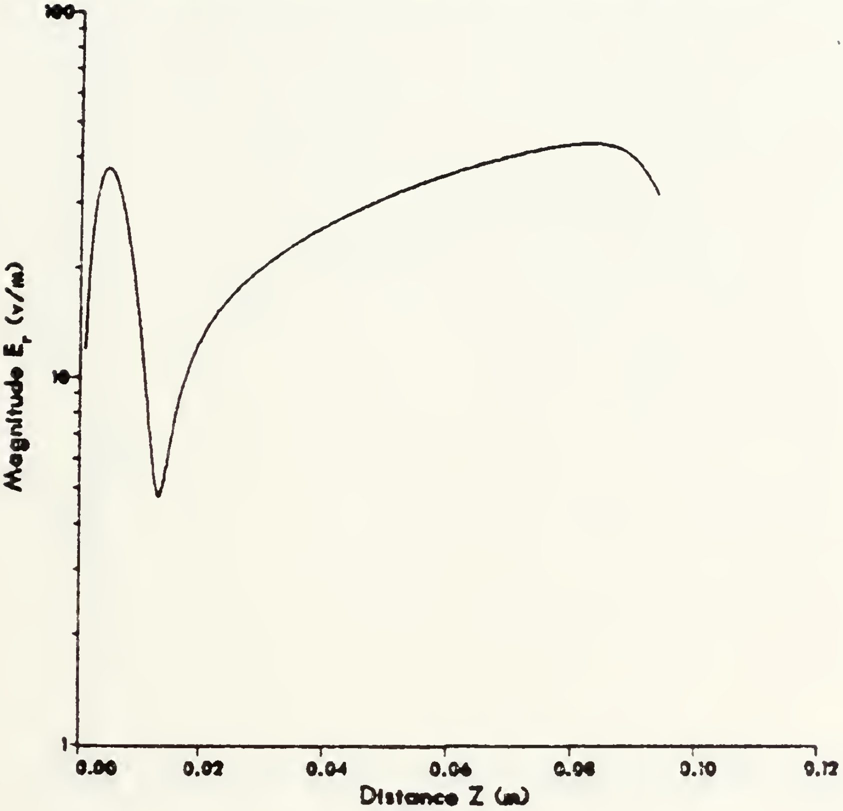

Plot Er vs z for a model of 19 segments.

Plot is 1 cm from the monopole axis along the z axis.

Figure B-11

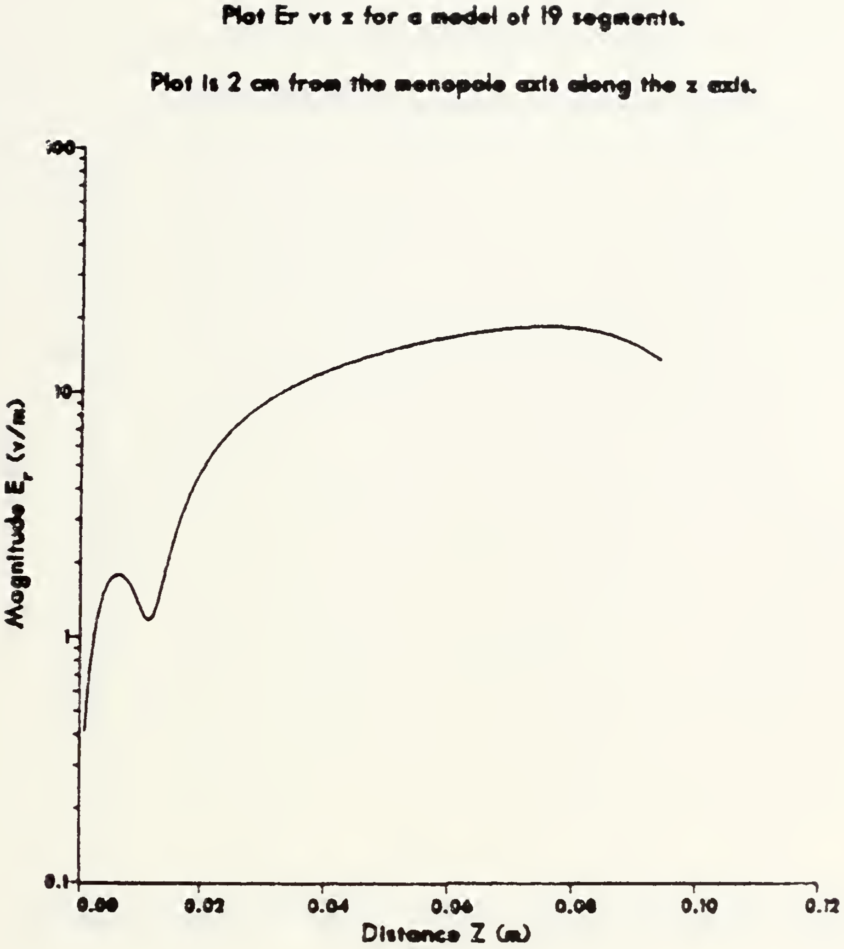

Plot Er vs z for a model of 19 segments.

Plot is 2 cm from the monopole axis along the z axis.

Figure B-12

Plot Er vs z for a model of 19 segments.

Plot is 3 cm from the monopole axis along the z axis.

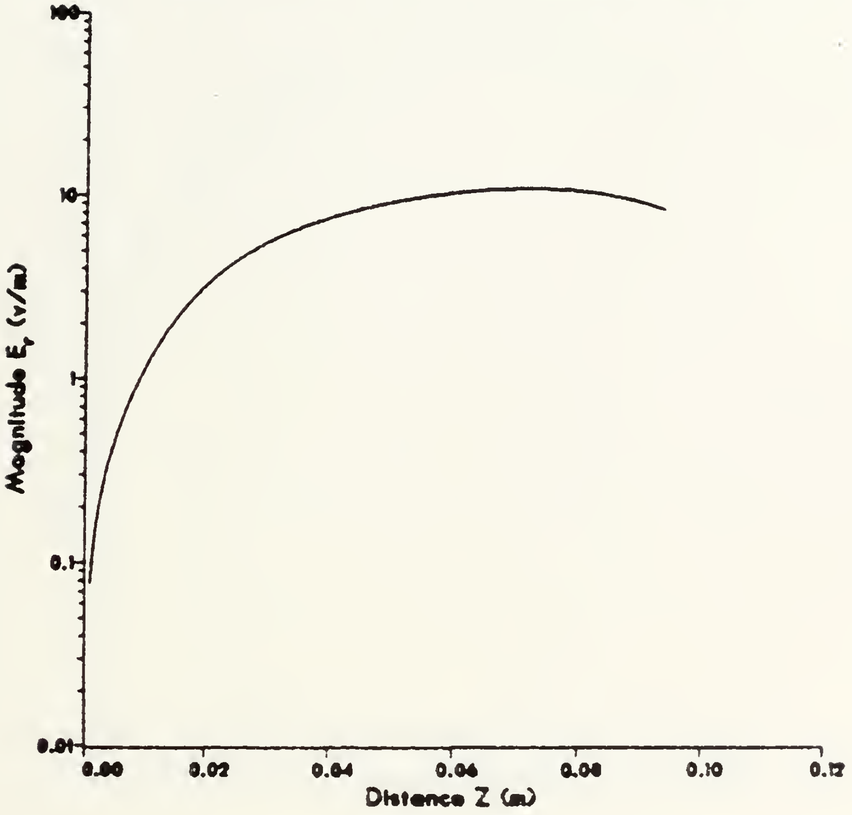

Figure B-13

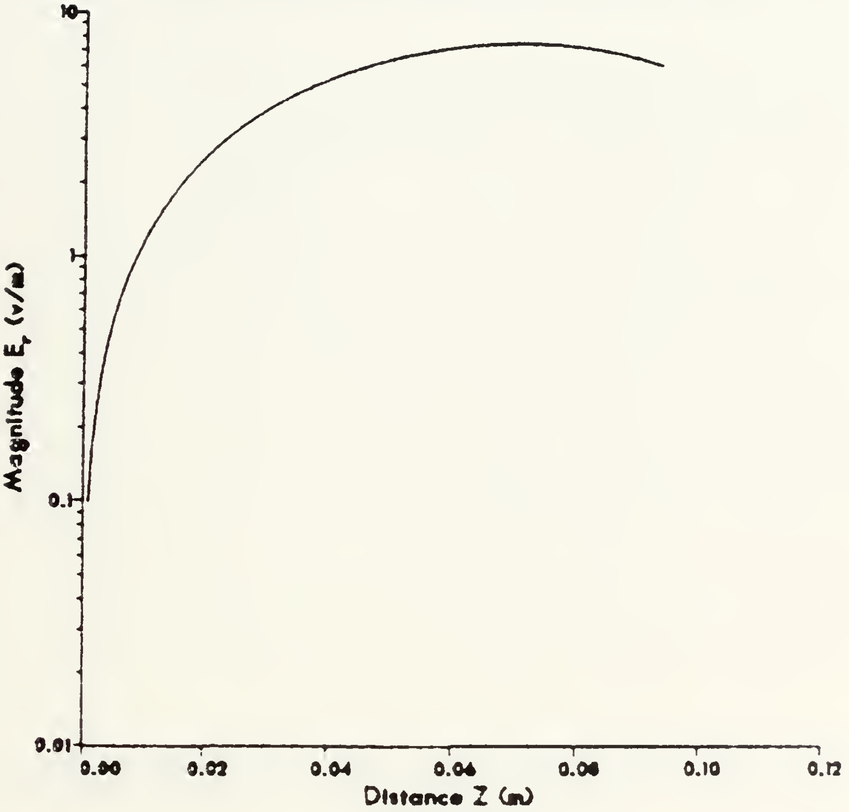

Plot Er vs z for a model of 19 segments.

Plot is 4 cm from the monopole axis along the z axis.

Figure B-14

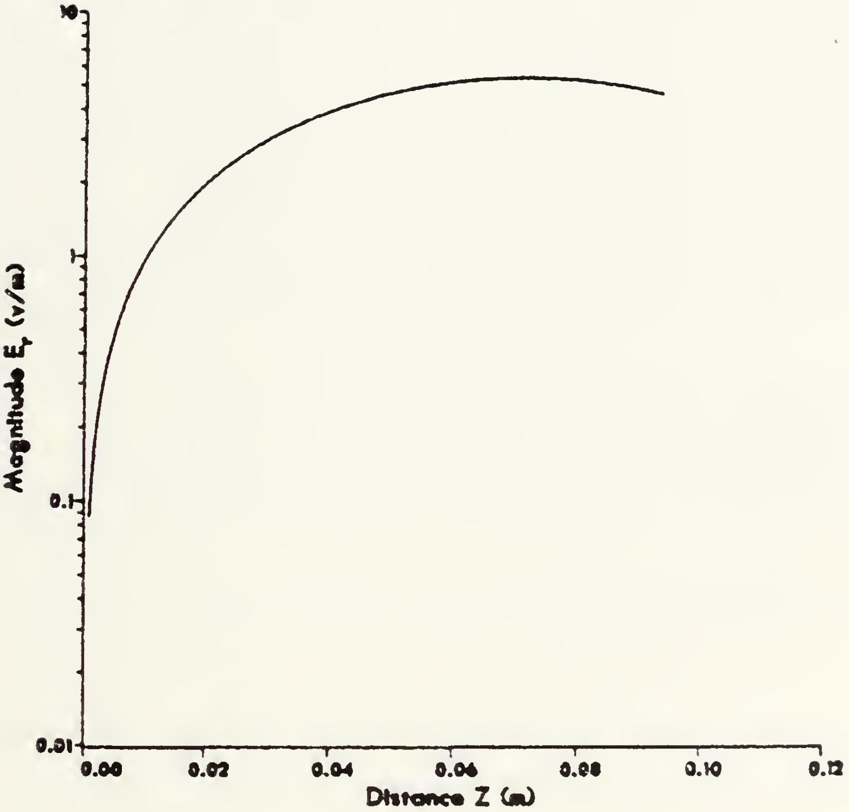
Plot Er vs z for a model of 19 segments.

Plot is 5 cm from the monopole axis along the z axis.

Figure B-15

Plot Er vs z for a model of 19 segments.

Plot is 6 cm from the monopole axis along the x axis.

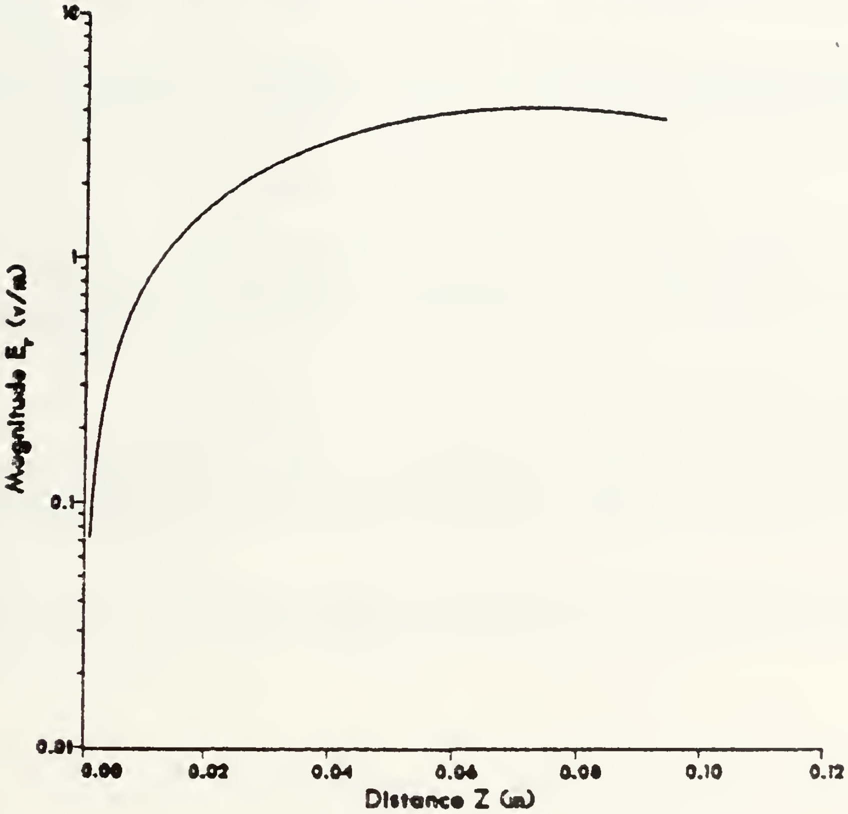

Figure B-16

LIST OF REFERENCES

1. MIL-HDBK-238(NAVY), 10 August 1973.

2. Naval Ocean Systems Center Technical Document 116, NUMERICAL ELECTROMAGNETICS CODE (NEC) - Method of Moments, by G.J. Burke and A.J. Poggio of Lawrence Livermore Laboratory, January 1981.

3. Schelkunoff, S.A. and Friis, H.T., Antennas Theory and Practice, Wiley, 1952.

4. Jordan, E.C. and Balmain, K.G., Electromagnetic Waves and Radiating Systems, 2nd Ed., Prentice-Hall, 1968.

5. Kraus, J.D., Antennas, McGraw-Hill, 1950.

6. Chang, D.C., Halbgewachs, R.D., and Harrison, C.W., "The Electromagnetic Field Very Near to a Monopole", Transactions on Electromagnetic Compatability, Vol. EMC-17, No. 2, May 1975.

7. Balzano, Q., Garay, O., Siwiak, K., "The Near Field of Dipole Antennas, Part I: Theory" and "The Near Field of Dipole Antennas, Part II: Experimental Results", Transactions on Vehicular Technology, Vol. VT-30, No. 4, November 1981.

8. Mills, A.H., Fields Near Radiating Antennas, Unpublished, Undated.

INITIAL DISTRIBUTION LIST

		No. Copies
1.	Defense Technical Information Center Cameron Station Alexandria, Virginia 22314	2
2.	Library, Code 0142 Naval Postgraduate School Monterey, California 93943	2
3.	LCDR David D. Thomson (Code 3909) Naval Weapons Center China Lake, California 93555	2
4.	Dr. Richard W. Adler, Code 62 Naval Postgraduate School Monterey, California 93943	5
5.	Dr. Stephen Jauregui, Code 62Ja Naval Postgraduate School Monterey, California 93943	1
6.	Mr. W. R. Vincent, Code 62Ja Naval Postgraduate School Monterey, California 93943	1
7.	Chairman, Code 62 Department of Electrical Engineering Naval Postgraduate School Monterey, California 93943	1
8.	Commander Naval Electronic Systems Command Naval Electronic Systems Command Headquarters PME-107-9 Washington, D.C. 20360	1
9.	Commander Naval Electronic Systems Command Naval Electronic Systems Command Headquarters PME-107-6 Washington, D.C. 20360	1
10.	Commander Naval Security Group Command, G-80 Naval Security Group Headquarters 3801 Nebraska Avenue, N.W. Washington, D.C. 20390	1

207756

Thesis
T444 Thomson
c.1 Electromagnetic near-
field computations for
a broadcast monopole
using Numerical Elec-
tromagnetics Code (NEC).

27 JAN [illegible] 30202
24 JUL 87 33404

207756

Thesis
T444 Thomson
c.1 Electromagnetic near-
field computations for
a broadcast monopole
using Numerical Elec-
tromagnetics Code (NEC).

AMERICAN BINDERY
TOPEKA KANSAS
4

Electromagnetic near-field computations
3 2768 001 01109 1
DUDLEY KNOX LIBRARY